2013

Thermal analysis of undercooled metallic liquids by electromagnetic levitation drop calorimetry

Carl Tackes
Iowa State University

Thermal analysis of undercooled metallic liquids by electromagnetic levitation drop calorimetry

by

Carl Matthew Tackes

A thesis submitted to the graduate faculty
in partial fulfillment of the requirements for the degree of
MASTER OF SCIENCE

Major: Materials Science and Engineering

Program of Study Committee:
Ralph E. Napolitano, Major Professor
Monica Lamm
Matt Kramer

Iowa State University
Ames, Iowa
2013

TABLE OF CONTENTS

LIST OF TABLES

LIST OF FIGURES

ACKNOWLEDGEMENTS

There are many I would like to acknowledge for otherwise this thesis could not have been written. First I'd like to thank Ralph Napolitano and Shihuai Zhou for their support and discussions. I would also like to thank my committee members for their time and thoughts regarding my work. I'd also like to thank Matt Besser for his expertise (as well as patience) with regards to X-ray diffraction. I'd also like to acknowledge the contributions of my fellow group members: Tim Cullinan, Paul Matlage, Megan Meyer, Yang Huo, Irmak Sargin, James Acton, and Zach Royer.

This work was supported by the US Department of Energy, **Office of Basic Energy Science, Division of Material Sciences and Engineering**. The research was performed at Ames Laboratory, Ames Laboratory is operated for the US Department of Energy by Iowa State University under Contract No. DE-AC02-07CH11358. The document number assigned to this thesis is IS-T 3088.

ABSTRACT

Here the role of thermodynamic measurements in computational materials science (with a focus on metallic glasses) is described, of which the heat capacity of the undercooled liquid is identified as a key measurement. Traditional experimental techniques for generating thermodynamic measurements are then reviewed, as well as techniques that focus on the undercooled liquid. Then the development of a levitation calorimeter is presented, and the results of applying the technique to several binary Al-based glass forming compositions is described. The enthalpy of a reactive Al-rare earth liquid was measured as well as the enthalpy of the undercooled liquid of Al-rare earth glass forming compositions. The results indicated a constant heat capacity of the liquid throughout the temperature range studied, which is discussed with respect to liquid behavior. Additionally, the containerless levitation technique enabled the *in-situ* formation of metastable Al-Sm phases.

CHAPTER 1. Introduction

The increasing societal and technological demand for improved performance of engineered components calls for the development of materials that are stronger, safer, lighter, while being less expensive. As a result, there are great motivations to understand and quantify the relationship between a materials structure, processing techniques, and performance in order to effectively design and implement new materials systems. Thus, the design and application of new materials, such as amorphous, glassy, or nanocrystalline metals requires quantification of the thermodynamic and physical properties that underpin a material's behavior as a result of processing conditions.

The characterization of the structures and dynamics of metallic glasses requires analysis over a vast expanse of length scales, beginning with liquid ordering and continuing to extend in length to include consideration of formation stable and metastable crystalline structures which may exist in combination with partial glass formation or extend over the entire material. There is great motivation to not only understand the phenomenological aspects of glass formation (which properties changed?), but also how the structure influences the properties and performance of the system. The more difficult question is, "why does this property change?"

That is not meant to downplay the usefulness of a phenomenological understanding of a system, when it is often sufficient to have a consistent description of how properties change. For instance, there has been considerable success in the search for better glass formers based on empirical rules, presented by Inoue [49], where it has been shown that glass formability is improved with an increased number of elements with large atomic size ratio differences ($\sim$12 %), and highly negative enthalpies of mixing. These rules are thought to be related to chemical and topological ordering, however the ideal case of *predictive* multi-scale control of glassy and nanocrystalline materials is improved with the atomic level quantification of the

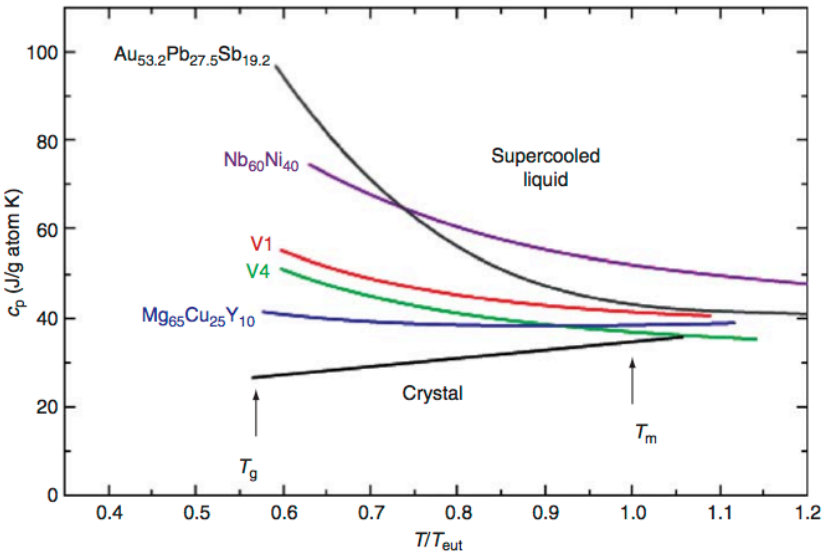

Figure 1.1 Specific heat capacities of the undercooled liquid for several alloys from [2]. V1 and V4 are Vitreloy-1 and Vitreloy-4 alloys. Plotted data from [3, 4, 5].

role of ordering in metallic liquids [50, 51]. Indeed, the goal of understanding structural-motifs and their selection as a function of time and temperature shows promise for a more universal understanding of the glass transition [52].

The quantification of bulk thermodynamic properties, such as the specific heat capacity, C_p, of the undercooled liquid brings insight into the configuration of the liquid. The heat capacity of material is inherently related to its structure, where changes in bonding nature, or short-range ordering are reflected in the heat capacity. Furthermore, the undercooled heat capacity enables calculation of the Gibbs free energy difference between the undercooled liquid and crystalline states, ΔG_{l-s}, the magnitude of which is indicative of the degree of instability of the liquid [53]. Small Gibbs free energy differences between the liquid and solid, coupled with classical nucleation theory, are indicative of slow nucleation rates, which reduces the critical cooling rate required to form a glass. It has been demonstrated that glass forming systems can exhibit a variety of temperature dependence of the heat capacity [21, 2] which is indicative of the liquid behavior and 'strength' against crystallization. Some reported specific heat capacities and Gibbs free energy differences between the liquid and crystalline solid can be seen in Figure 1.1 and Figure 1.2 respectively.

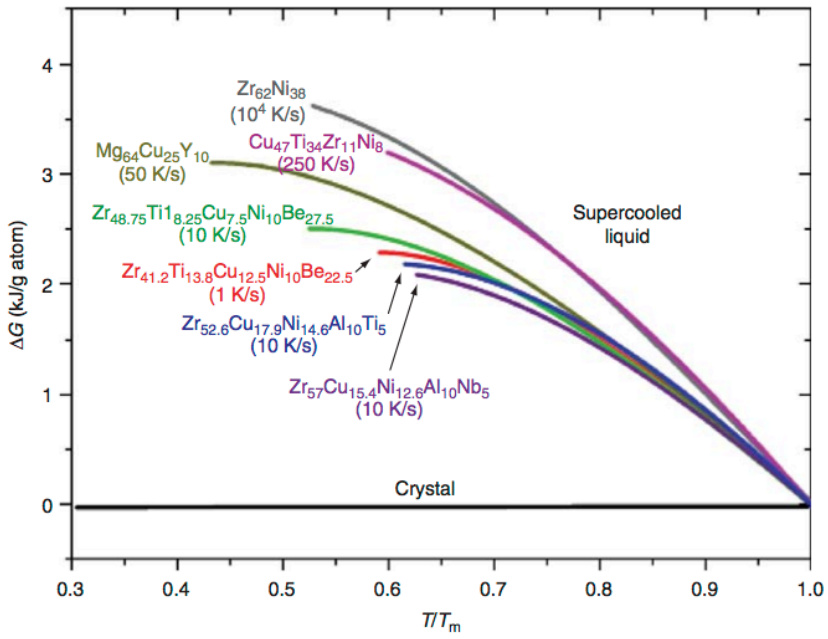

Figure 1.2 Difference in Gibbs free energy between the liquid and crystalline states from [2]. Critical cooling rates are listed below the composition. Plotted data from [3, 5, 6].

The undercooled heat capacity also enables the calculation of ΔS_{l-s}, the entropy difference between the undercooled liquid and crystalline state, which can be used to calculate the Kauzmann temperature, T_k, discussed in detail later, which is presented to be the lowest entropy limit of the undercooled liquid. T_k is defined as the point in which the entropy of the undercooled liquid is equal to that of the crystalline state, which is paradoxical. An example of the calculation of ΔS_{l-s} can be seen in Figure 1.3. Determination of T_k, and the kinetic limit of glass formation, the glass transition temperature, T_g, as well as the temperature limit of liquid stability with respect to crystalline phases, T_0 (also discussed later), is of interest to further understand the glass transition phenomenon.

Experimental measurements of the undercooled liquid are generally scarce, having been described as the most neglected thermodynamic measurement [54] due to the experimental challenges required to reduce the energetic advantage for nucleation provided by surfaces such as container walls or impurities. Additionally, empirical estimations of the heat capacity of undercooled liquids such as the model of Thompson [18] diverge from experimental data as undercooling is increased [15, 55]. In this work, the development of a levitation calorimeter is

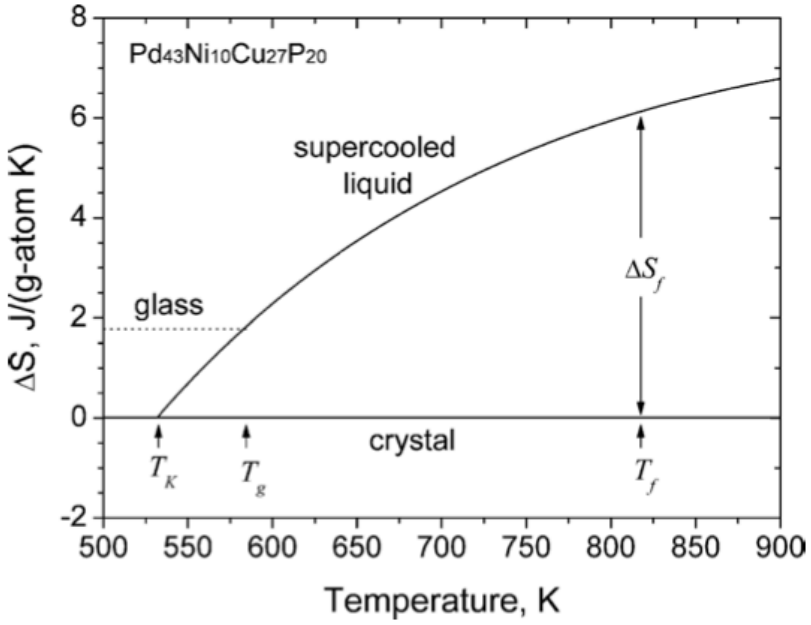

Figure 1.3 Difference in Entropy between the liquid and crystalline states, ΔS_{l-s}, for a $Pd_{43}Ni_{10}Cu_{27}P_{20}$ alloy [7]. T_k is the Kauzmann temperature, T_g is the kinetically observed glass transition, and T_f the peak fusion temperature (melting temperature).

presented that enables access to far-from-equilibrium conditions at the laboratory time scale. The technique is used to probe the undercooled liquid for two binary Al-Re (Rare earth) glass forming alloys, which to date has only been analyzed in far-from-equilibrium conditions as a result of high cooling rates.

In addition to the undercooled liquid, thermodynamic measurements in the liquid state are also valuable on their own for use in industry in simulations or heat balances to improve production efficiency. Almost all industrial metal productions require heating the product to the liquid state at some point. Additionally, liquid thermodynamic measurements are used for the development of phase diagrams (both equilibrium and non-equilibrium) which are valuable when developing new materials systems.

In this work, the role of thermodynamic measurements (including the undercooled liquid) in models will be summarized with an emphasis on those related to glass formation. Traditional experimental techniques for obtaining thermodynamic measurements will also be outlined. The development of a thermal analysis technique which can be used to measure thermodynamic properties in the liquid state as well as probe far-from-equilibrium experimental conditions such as the undercooled liquid state will be described, and finally the results of applying the technique to Al-based rare earth glass forming alloys will be presented.

CHAPTER 2. The Role of Thermodynamic Measurements in Computational Materials Science

2.1 Introduction

Thermodynamics provides a framework for which a great deal information about the behavior of matter can be arranged. A widely used aspect of thermodynamics is its use in describing stability of a state in terms of energy (usually Gibbs free energy). If the free energy of a system as a function of atomic arrangement is presented, there generally exists maxima and minima. Maxima are therefore inherently unstable, in which the energy can be easily lowered by atomic re-arrangement. As a result, decreases in free energy drive the maxima towards a minima and the absolute minimum is defined as the stable state, with any relative minima above that state defined as metastable. The rates of transformation, described by kinetics, can be sufficiently slow enough to render a metastable state practically stable, which can lead to many uses like martensitic transformations in steels or glassy metals [56].

Real materials are generally multicomponent and multiphase, where phases may be chemical solutions or specific stoichiometric compounds. The phases are most frequently crystalline with a host of defects associated with occupancy on the lattice and anomalies in the periodicity. The structure in general, due to its composite nature, includes interfaces of various types and perhaps other inhomogeneities. The field of materials science is largely focused on the creation and control of these multi-scale multiphase defected structures and their correlation with observable material properties. Knowledge of the Gibbs free energy as a function of chemical composition and temperature, i.e. $G(x, T)$, provides a map of stability known as a phase diagram. Phase diagrams can be used to answer a variety of questions along the lines of "what happens if?" [57]. Phase diagrams can be determined experimentally using thermal

analysis techniques such as DSC and DTA, and also from calculations when a comprehensive thermodynamic description of the components is available. The three main techniques used for generating thermodynamic data are calorimetry, vapor pressure measurements, and electromotive force measurements. Each of these techniques have advantages and limitations, and will be discussed in more detail later. From these measurements, thermodynamic functions of phases can be determined and when collected can be used to determine a phase diagram. A complete thermodynamic description of a system often requires several measurements, usually a combination of calorimetry and either electromotive force or vapor pressure measurements [1].

As described earlier, amorphous and glassy metals are formed in extreme conditions, far-from-equilibrium. How can thermodynamics, of which equilibrium is a pre-requisite, be used to further understanding of these conditions? The energetic landscape of glass formation is complex, and the liquid can select many different solidification pathways. Depending on the undercooling, there exists a multitude of viable crystalline structures (stable or metastable), each having different diffusional requirements. Additionally, the liquid may form clusters, icosahedral or otherwise [51], which influences the interfacial energy and provides an energy barrier to crystallization [58]. The simplest description of glass formation is 'failed crystallization', in which the undercooled liquid is stable for the kinetically required time period to reach the glass transition. Within this simple framework, thermodynamic limits of glass formation can be calculated and provide insight into glass formation. Determining glass forming compositions and temperatures requires kinetic analysis, however it is useful to have some measure of thermodynamic viability for the limits of crystallization which are likely to be kinetically suppressed.

The critical data for such thermodynamic models is that of the undercooled liquid. Additionally, thermodynamic measurements in far-from-equilbrium conditions are used in relation to first-principles (*ab-initio*) and molecular dynamics simulations to provide a measure of accuracy and link the methods to a real system. These techniques can investigate conditions of glass formation otherwise inaccessible, and it is difficult to comprehend the quantification of the complex structures and dynamics of metallic glasses without them.

This chapter is therefore dedicated to describing the roles of the most relevant thermodynamic measurements in computational materials science, with a focus on computational techniques used to further understand glass formation.

2.2 Thermodynamic Models

The Gibbs free energy of the undercooled liquid allows for the calculation of the Kauzmann temperature, T_k, as well as T_0 curves, which define the stability limit for the liquid based on the Gibbs free energy of the liquid and available competing phases that can form at the same composition (without partitioning). The Kauzmann [59] temperature is the temperature at which the entropy of the undercooled liquid is equal to that of the crystal, and approaching T_k likely causes an 'entropy crisis' [60] in the liquid, forcing either glass formation or crystallization as it is paradoxical for a liquid to exist with a lower entropy than the crystal state. The Kauzmann temperature is often presented as the absolute limit for the glass transition, where often kinetic arrest occurs at higher temperatures.

In general, nucleation of a crystalline phase requires compositional rearrangements in the undercooled liquid. At high undercoolings, such compositional fluctuations are kinetically suppressed, however there exists the possibility of the nucleation of a phase of the same composition as the liquid, known as partitionless solidification [21]. This can only occur with the fulfillment of two conditions, the composition of the liquid and crystal must be the same, and the solidification rate (dependent on the undercooling) be of high enough magnitude such that complete solute trapping would be energetically favorable [8]. T_0 is defined as the temperature-composition curve in which the the undercooled liquid is stable compared to crystalline phases that may form without partitioning. Thus, for any given temperature and composition under the T_0 curve allows for partitionless crystallization. The Gibbs free energy for the T_0 condition is illustrated in Figure 2.1.

Solidification rates for partitionless crystallization are several orders of magnitude higher than cases where partitioning is observed, and thus not likely to be kinetically suppressed even with high cooling rates. For this reason, T_0 curves are often used to bound the compositional region where partitionless crystallization is not possible, therefore indicating a thermodynamically

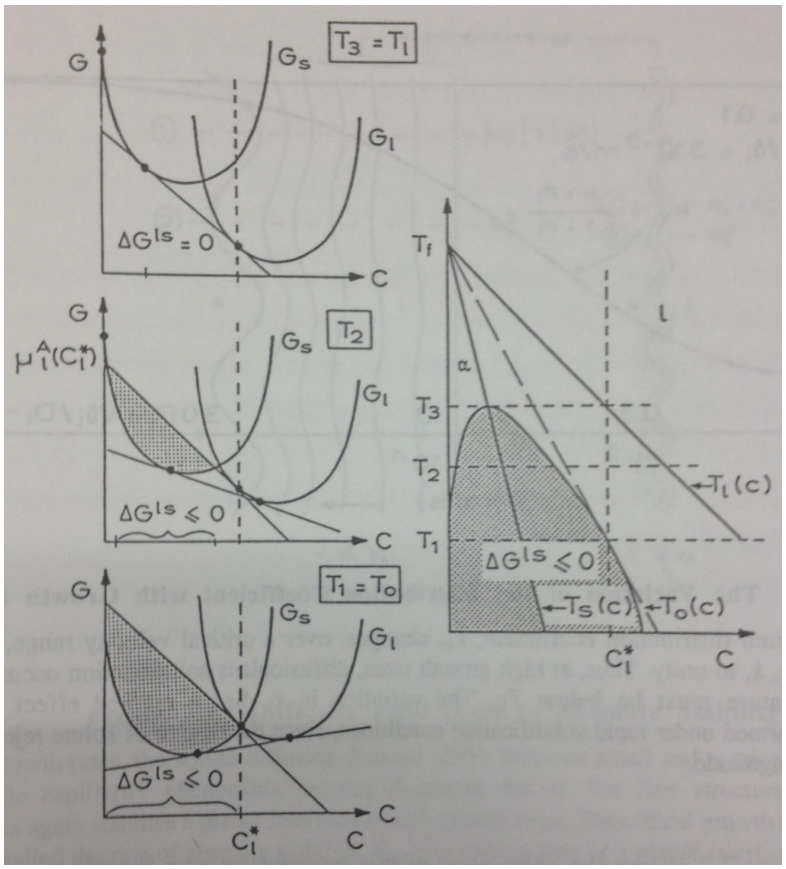

Figure 2.1 Schematic Gibbs free energies for the illustration of partitionless crystallization [8]. It can be seen that for a given composition C_l^*, the the required temperature for the condition $\Delta G^{ls} = 0$, where T_1 illustrates the T_0 condition, and any temperature below which allows for partitionless solidification.

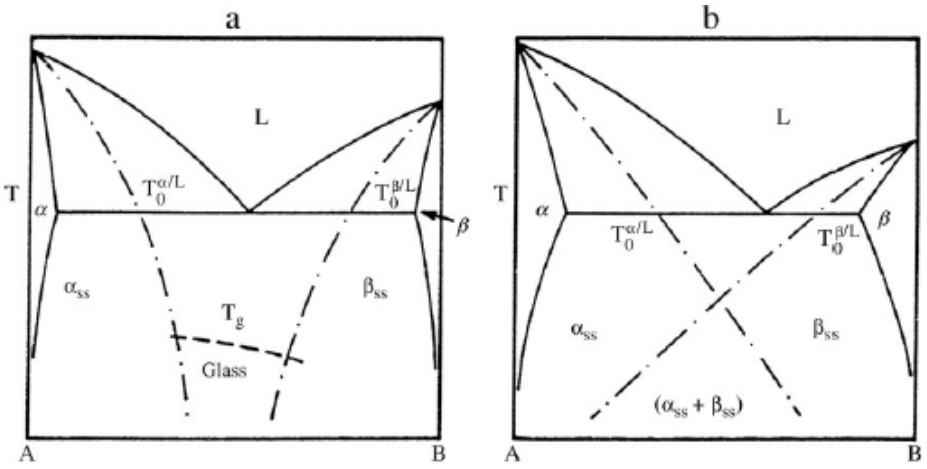

Figure 2.2 For a binary system A-B, if the T_0 curves 'plunge' (a), glass formation is possible. Should the T_0 curves intersect, the liquid would instead form $\alpha + \beta$ without partitioning (b). Figure from [9].

viable composition range for glass formation. The determination of this thermodynamically viable range is useful prior to the application of rigorous kinetic treatments. An illustration of T_0 curves can be seen in Figure 2.2.

For a real system, when a comprehensive thermodynamic description of a system has been obtained (including the undercooled liquid) the previously mentioned T_0 criterion can be calculated,

$$\Delta G^{C_x} = G^{C_x}_{liq} - G^{C_x}_{crystal} \leq 0, \tag{2.1}$$

where C_x denotes the composition for which the crystalline phase can solidify without partitioning. For example, the Al-La system was investigated by Zhou and Napolitano [10], in which T_0 and T_k curves were calculated and can be seen in Figure 2.3 with comparison to experimentally measured glass formation.

The definition of a metallic glass is often under debate, as it is possible to form some small fraction of crystals that are virtually undetectable. From this definition, the T_0 criterion would predict a smaller region of glass formation. The formation of glasses with some allowable volume fraction of crystals can be calculated with a modified T_0 criterion in which classical nucleation theory [16, 61] is applied, along with consideration of cooling rates, such as the work of Nash and Schwarz [12]. An example of this modified T_0 calculation can be seen in Figure 2.4.

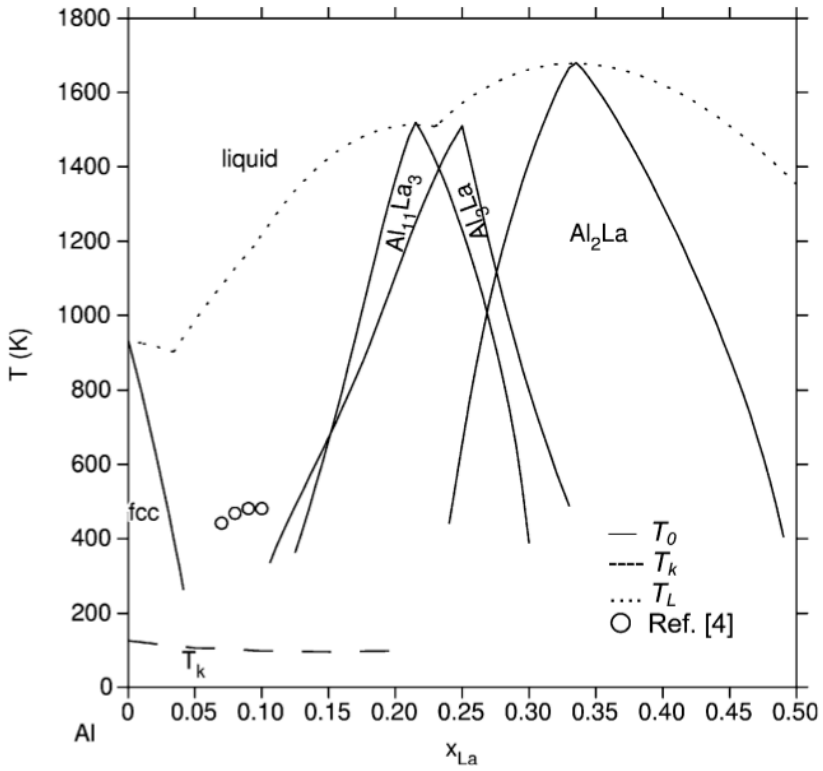

Figure 2.3 T_0 and T_k curves calculated by Zhou and Napolitano, with experimental comparison [10]. Ref. 4 is the experimental observations of glass formation from Inoue [11].

As thermodynamic approaches to glass formation require knowledge of all competing phases, often thermodynamic limitations are calculated within the CALPHAD (CALculation of PHAse Diagrams) framework. The CALPHAD method allows for the calculation of stable phase diagrams, as well as incorporation of metastable phases, and can include treatment of the undercooled liquid [9].

The CALPHAD method is a robust technique in which researchers can combine a variety of experimental (XRD, EPMA, DTA) data, and thermodynamic data to optimize and develop a self-consistent description of a system. A flow chart for the CALPHAD procedure can be seen in Figure 2.5.

Researchers must choose between a variety of models to describe how the atoms interact with each other. For instance, take the description of the Al-Sm system by Zhou and Napolitano [46], in which the liquid is described using a two-state association model, terminal

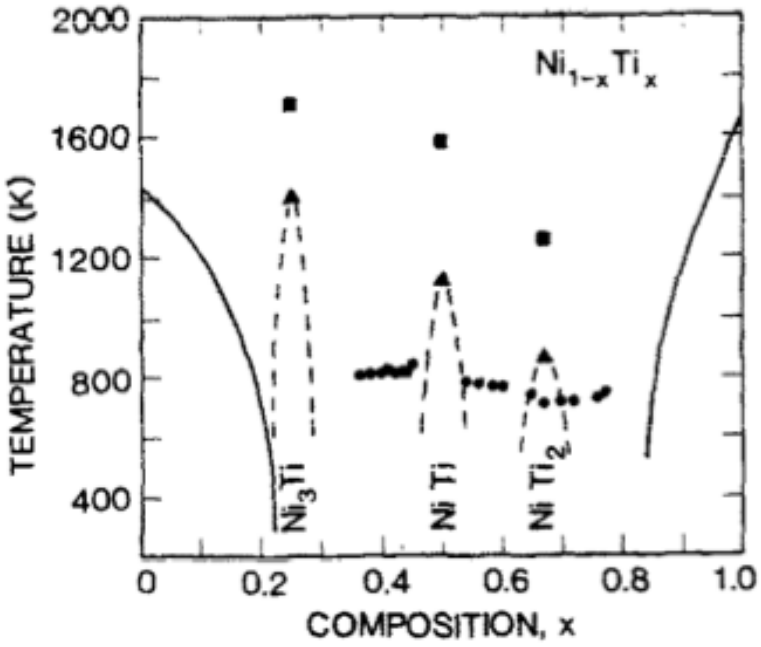

Figure 2.4 Modified T_0 curves, evaluated for a crystal volume fraction of 10^{-6}, and a cooling rate of 10^6 K/s from [12]. The solid circles are experimentally determined glass compositions, with their temperature being the crystallization temperature on heating [13]. Triangles are the melting point of the compound.

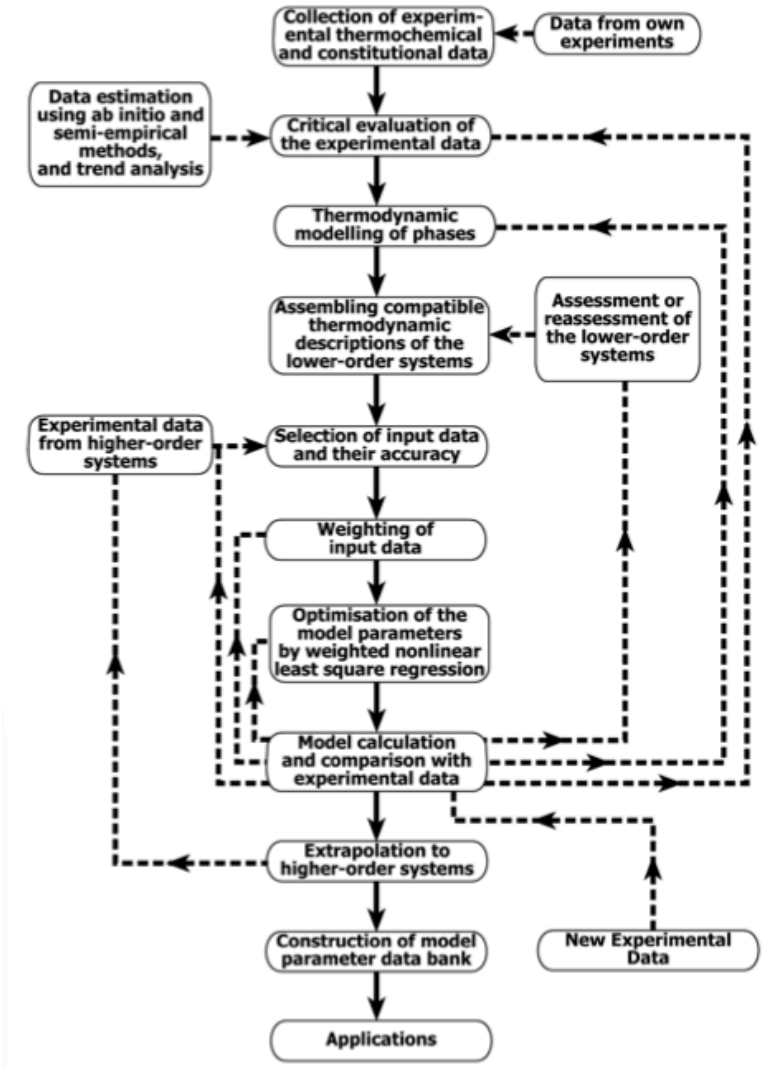

Figure 2.5 Flowchart describing CALPHAD method [14]

phases are described using a one-sublattice model, metastable phases are approximated using a two-sublattice model, and intermediate phases treated as stochiometric compounds. Indeed, accurately modeling the interactions of atoms usually requires a range of models of varying complexity [62].

It is desirable to describe the mixing of components with respect to the pure components [62],

$$G = G^o + G^{ideal}_{mix} + G^{xs}_{mix} \tag{2.2}$$

in which G^o is the contribution of the pure components, G^{ideal}_{mix} is the contribution from ideal

mixing, and G_{mix}^{xs} represents the contribution from non ideal interactions. This definition is useful because many researchers have compiled accurate thermodynamic data for pure substances to use in calculations [42]. There are a variety of solution types used in CALPHAD modeling to handle some of the complicated phases in some material systems, such as [62]: line compounds, interstitial phases in steels, order-disorder transformations, ionic liquids (slags, molten salts), or even aqueous solutions. These can be treated with a variety of restrictions related to individual components, and a definition of the Gibbs free energy can be obtained.

It is then desirable to compare the definition of the Gibbs free energy of mixing to that of a real system to show accuracy. Having generated a model for the Gibbs free energy using the CALPHAD approach, it is possible to calculate the enthalpy of mixing. It is therefore desirable to measure the enthalpy of mixing to compare to the calculations. Later in this work, enthalpy of mixing is determined for comparison with modeling, and can be seen in Chapter 5.

The CALPHAD framework is the most convenient for application of thermodynamic limitations of glass formation. The properties of metastable phases must be calculated, and the undercooled liquid must be described. The calculation of phase diagrams for amorphous alloys has been examined extensively [63, 64, 65, 66, 9, 46, 10]. The critical thermodynamic data for this approach is that of the undercooled liquid. The Gibbs free energy for the undercooled liquid phase is usually estimated by the difference between the energy of the undercooled liquid and the equilibrium solid, as described in Eqs. 2.3 to 2.6.

2.2.1 Thermodynamic Properties of the Undercooled Liquid

The Gibbs free energy of the undercooled liquid is often considered with reference to the equilibrium crystalline state. The undercooled liquid is inherently unstable, and the driving force is defined as

$$\Delta G_{l-s} = \Delta H_{l-s} - T\Delta S_{l-s}, \tag{2.3}$$

where the enthalpy and entropy are also considered with respect to the equilibrium crystalline state.

The enthalpy difference between liquid and solid is described as [67]

$$\Delta H_{l-s} = \Delta H_f - \int_T^{T_m} \Delta C_p^{l-s} \, \mathrm{d}T, \tag{2.4}$$

and the entropy difference between liquid and solid is described as [67]

$$\Delta S_{l-s} = \Delta S_f - \int_T^{T_m} \frac{\Delta C_p^{l-s}}{T} \, \mathrm{d}T, \tag{2.5}$$

where ΔH_f and ΔS_f are the enthalpy and entropy of formation, and ΔC_p is the difference of heat capacity between the liquid and solid, and T_m the melting temperature. And by the combination of Eqs. 2.3 to 2.5, the Gibbs free energy difference, ΔG_{l-s}, can be described:

$$\Delta G_{l-s}(T) = \left[\Delta H_f - \int_T^{T_m} \Delta C_p^{l-s} \, \mathrm{d}T\right] - T\left[\Delta S_f + \int_T^{T_m} \frac{\Delta C_p^{l-s}}{T} \, \mathrm{d}T\right]. \tag{2.6}$$

This allows for direct calculation of the Gibbs free energy difference as well as the Kauzmann temperature, T_k ($\Delta S_{l-s} = 0$), from measurements of specific heat of the undercooled liquid. The heat capacity of the undercooled liquid is rarely available, having been considered the most neglected thermodynamic quantity [54], thus various approximations have been developed such as that of Turnbull and Fisher [16], Dubey and Ramachandrarao [17], Thompson and Spaepen [18], and Hoffman [19]. It has been shown that for even moderate undercoolings accurate experimental data is required for successfully predicting solidification phenomena [15] which is shown in Figure 2.6.

The variation in the predicted value for ΔG_{l-s} in Figure 2.6 can be used in combination with classical nucleation theory to predict critical cooling rates, which in this case vary over several orders of magnitude [21].

2.2.2 Temperature Dependence of the Undercooled Heat Capacity and Associated Liquid Behavior

Recently there has been an effort to classify glass forming metallic alloys based on their 'strength' against crystallization, based on the dynamics of the undercooled heat capacity [2] and viscosity [68]. The temperature dependence of the undercooled heat capacity is related to the formation of short-range ordering, which plays an important role in glass formation. Chen

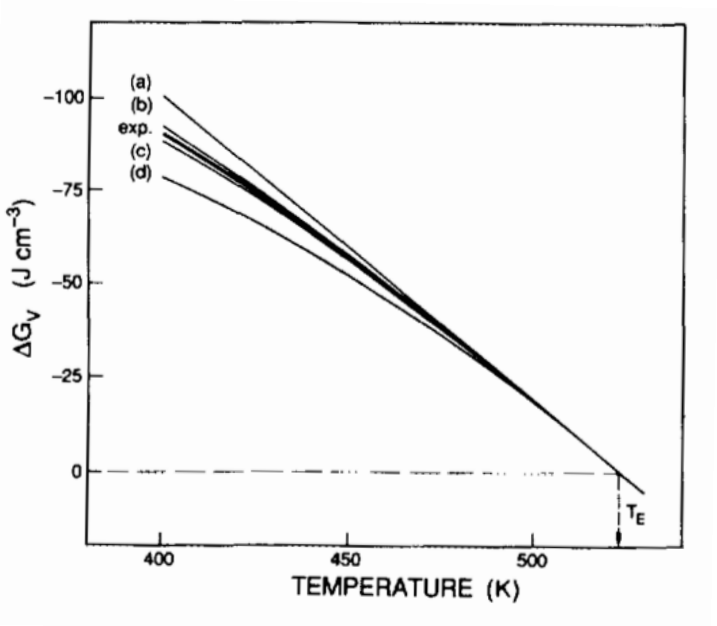

Figure 2.6 Comparison between various empirical models for the undercooled heat capacity, used in the calculation of the difference of Gibbs free energy per volume [15]. (a)-(d) refer to the models of Turnbull [16], Dubey [17], Thompson [18], and Hoffman [19], respectively.

and Turnbull proposed several mechanisms for the change in heat capacity of liquids that relate to their configuration such as [69],

- a change in the vibrational spectrum as a result of the change in the types of bonding,
- an increase in non-random associations between unlike atoms as temperatures decrease,
- and changes in the configurational entropy from the multiplicity of atomic positioning.

The first is related to the quantum-mechanical phonon theory of temperature, in which the motions of an atomic lattice are a result of the collective excitation of quasi-particles that oscillate at a given frequency. For low temperature crystals, the Debye law accurately predicts the temperature dependence of the heat capacity solely from the vibrational contribution of photons, should the electronic contribution to the heat capacity be negligible. In liquids, atoms gain additional degrees of freedom such as rotation and translation, however the vibrational mode is still important. Later work in analysis of metallic glasses has identified the Boson Peak [70], an excess contribution to the Debye predicted vibrational density of states, which has been

controversial in determining its meaning with respect to glass formation [71, 72]. Computational analyses predict that the Boson Peak is a result of localized anharmonic vibrational modes associated with the 'defects' in glasses [73], and that the magnitude of the Boson Peak is related to the liquid behavior that formed the glass.

In Chen and Turnbull's second proposal, an increase in non-random associations on cooling, they describe the phenomenon more commonly known as short-range ordering, and they predicted short-range ordering had a significant effect on the temperature dependent behavior of the heat capacity. The formation of short-range ordering often has a large effect on the specific heat capacity, as a result of the formation of bonds and clusters in the liquid state, the available degrees of freedom are reduced. A wide variety of temperature dependent behavior of the undercooled heat capacity has been reported, and will be shown here. The heat capacity of $Pd_{40}Ni_{40}P_{20}$ and $Pd_{77.5}Cu_6P_{16.5}$ is illustrated in Figure 2.7.

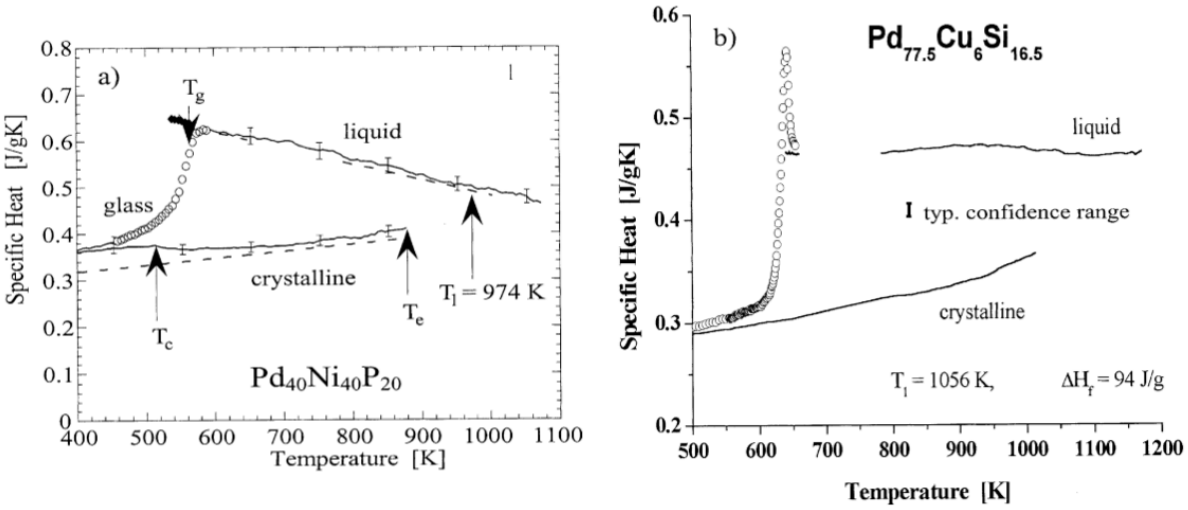

Figure 2.7 $C_p(T)$ for two BMG alloys, $Pd_{40}Ni_{40}P_{20}$ (left) and $Pd_{77.5}Cu_6Si_{16.5}$ (right) from [20]. $Pd_{40}Ni_{40}P_{20}$ has been characterized with strong liquid behavior [21], $Pd_{77.5}Cu_6Si_{16.5}$ is more fragile [22]. On left, linear temperature dependence can be observed, on right, no discernible temperature dependence until a large peak near the glass transition.

$Pd_{77.5}Cu_6Si_{16.5}$ can be cast into a rod of 11mm diameter, and its behavior is classified as fragile, and one of the best glass formers, $Mg_{65}Cu_{25}Y_{10}$, can form rods up to 22 mm in diameter, and its kinetic behavior is strong [22]. The temperature dependence of the heat capacity of

$Mg_{65}Cu_{25}Y_{10}$ is very low, which can be seen in Figure 2.8.

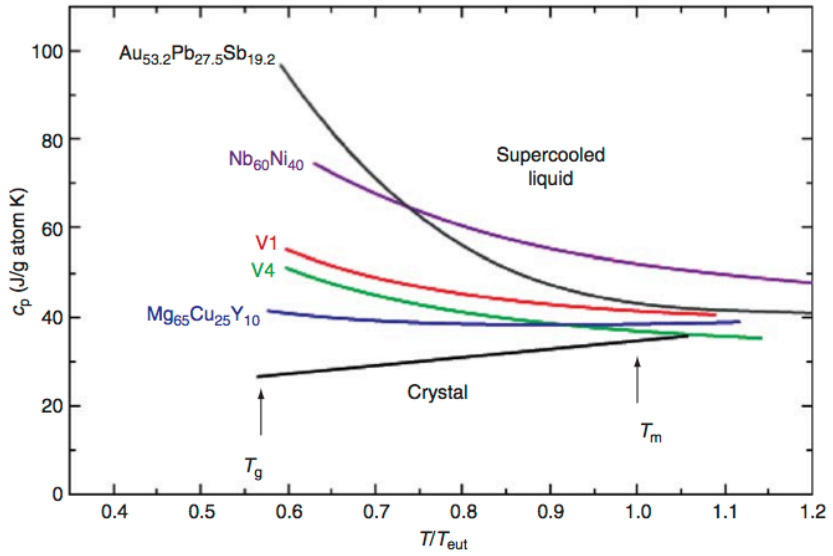

Figure 2.8 Specific heat capacities of the undercooled liquid for several alloys from [2]. V1 and V4 are Vitreloy-1 and Vitreloy-4 alloys. Plotted data from [3, 4, 5].

Fragile liquids are inherently more difficult to measure the heat capacity over the entire undercooled liquid range, due to their decreased resistance to crystallization. In Figure 2.7, a glassy sample was annealed at $T > T_g$ and then measured on cooling through the glass transition. Another example of a fragile liquid can be seen in Figure 2.9.

This review of experimentally measured heat capacities leads to the general conclusion that fragile liquids display a peak in the heat capacity near the glass transition, 'good' glass formers like $Pd_{40}Ni_{40}P_{20}$ display a weak linear temperature dependence, and one of the best glassformers, $Mg_{65}Cu_{25}Y_{10}$, displays a very shallow temperature dependence. The other very good BMG alloys (Vitreloy alloys in Figure 2.8) also display a very shallow temperature dependence of the heat capacity.

Future directions for analyzing the glass transition have been summarized by Debenedetti and Stillinger [60], Cheng and Ma [50], and Sheng et. al. [51]. Of the future directions, the energy landscape framework will be briefly discussed here, which is related to Chen and Turnbull's third proposal; ΔC_p is related to changes in the configurational entropy of the system.

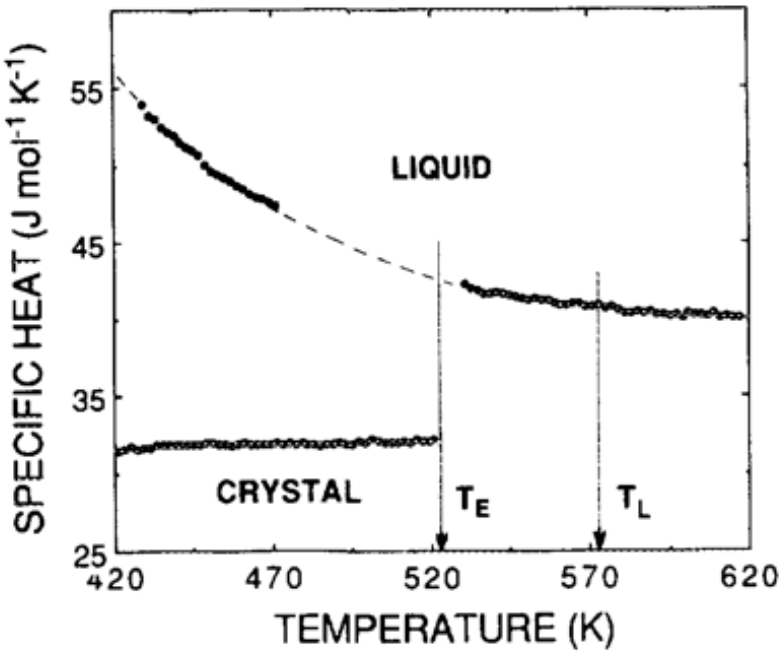

Figure 2.9 Specific heat capacities of liquid, undercooled liquid, and crystalline $Au_{53.2}Pb_{27.6}Sb_{19.2}$ by Fecht et. al. [15]. It can be seen that the heat capacity of the undercooled liquid is neither constant or linear as shown before, but of second order temperature dependence.

Configurational entropy is defined as a measure of the available structural states, which decreases as temperatures decrease. The concept of configurational entropy was presented by Adam and Gibbs for a connection between kinetics and thermodynamics in their theory for cooperatively rearranging regions [74],

$$t = t_0 \exp(B/S_c(T)) \tag{2.7}$$

where t is a relaxation time (essentially viscosity), $S_c(T)$ the configurational entropy, and t_0 and B are T independent constants. In Equation 2.7 it can be seen that the relaxation time, t, approaches infinity if the ideal glass transition temperature, T_k ($S_c(T_k) = 0$), is approached. Quantitatively defining the available states is one of the main challenges of applying Adam-Gibbs theory, along with the increasing notion that metallic liquids are heterogenous in nature, in which localized regions may relax differently than the bulk (dynamical heterogeneity [75]).

The configurational entropy, S_c, can be approximated experimentally [74],

$$S_c(T) = \Delta C_p \ln(T/T_k), \tag{2.8}$$

where T is the temperature, and T_k the ideal glass transition temperature ($S_c(T_k) = 0$). The Adam-Gibbs relation has been shown to be interesting in its relation to Volger-Tamman-Fulcher (VTF) viscosity theory, where if the configurational entropy is assumed to be constant, the Adam-Gibbs relation predicts Arrhenius viscosity behavior (strong liquid behavior) [76]. In this way, a non-zero temperature dependence of the heat capacity predicts deviation from Arrhenius viscosity behavior that is adequately described by VTF theory (fragile behavior).

The relation by Adams and Gibbs indicates that the origin of the glass transition is related to a decrease in the number of configurations that the liquid can sample. The final result, i.e. one last configuration available, would be the ideal glass state. This is qualitatively similar to the energy landscape theory that was later proposed by Goldstein [77], which defines potential energy basins which are separated by thermally activated energy barriers. An example of an energy landscape can be seen in Figure 2.10.

The recent work of Ding et. al. contrasts the fraction of ordering (decreasing number of available states) for both $Mg_{65}Cu_{25}Y_{10}$ (one of the best BMG) and Cu-Zr (marginal) as a function of temperature [24]. The dominant ordering in $Mg_{65}Cu_{25}Y_{10}$ are tetragonal tri-capped polyhedra (TTP) and bicapped square antiprisms (BSAP)[24], where in $Cu_{64}Zr_{36}$ the ordering is icosahedral in nature [24, 25]. As can be seen in Figure 2.11, the bonding nature is linked to the heat capacity in this instance.

Ding et. al. went further to determine the temperature dependence of the medium-range ordering for $Mg_{65}Cu_{25}Y_{10}$, which they determined to be very small, seen in Figure 2.12.

The main conclusions of their analyses were that a high degree of inherent structures in the high temperature $Mg_{65}Cu_{25}Y_{10}$ liquid is the source of the heat capacity behavior [24]. The liquid is saturated with SRO structures even at the melting point, which implies a low configurational entropy, thus the temperature dependence of the heat capacity does not reflect structural changes. In contrast, the degree of ordering in $Cu_{64}Zr_{36}$ increases on cooling with a small dependence and then peaks, consistent with the fragile behavior discussed earlier. It is

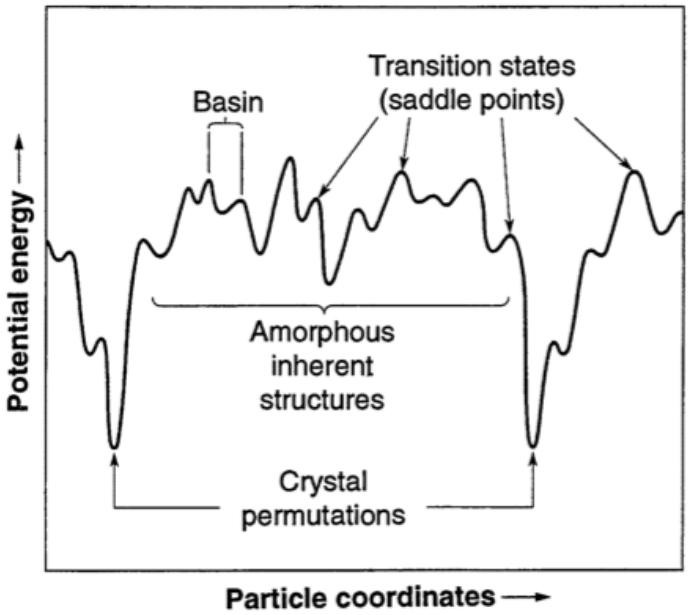

Figure 2.10 Potential energy landscape view of glass formation, where liquids can sample various inherent structures, amorphous or crystalline, in which transitions are thermally activated [23].

clear from this example that the measurement of the undercooled heat capacity is valuable to better understand the structural dynamics of metallic liquids.

In conclusion, the most valuable thermodynamic measurements for thermodynamic modeling to elucidate glass formation are as follows:

- The specific heat capacity of the undercooled liquid, in which experimental measurements are the most reliable for determining the Gibbs free energy and entropy of the undercooled liquid. Additionally, the heat capacity of the undercooled liquid is linked to the structure of the liquid and reflects changes in the ordering dynamics.

- The partial Gibbs free energies of components obtained by e.m.f or vapor pressure measurements and the enthalpy of mixing, to serve as a comparison to the calculated value to ensure that the mixing of components is appropriately determined for use in calculating the Gibbs free energies of metastable phases and calculation of T_0 curves.

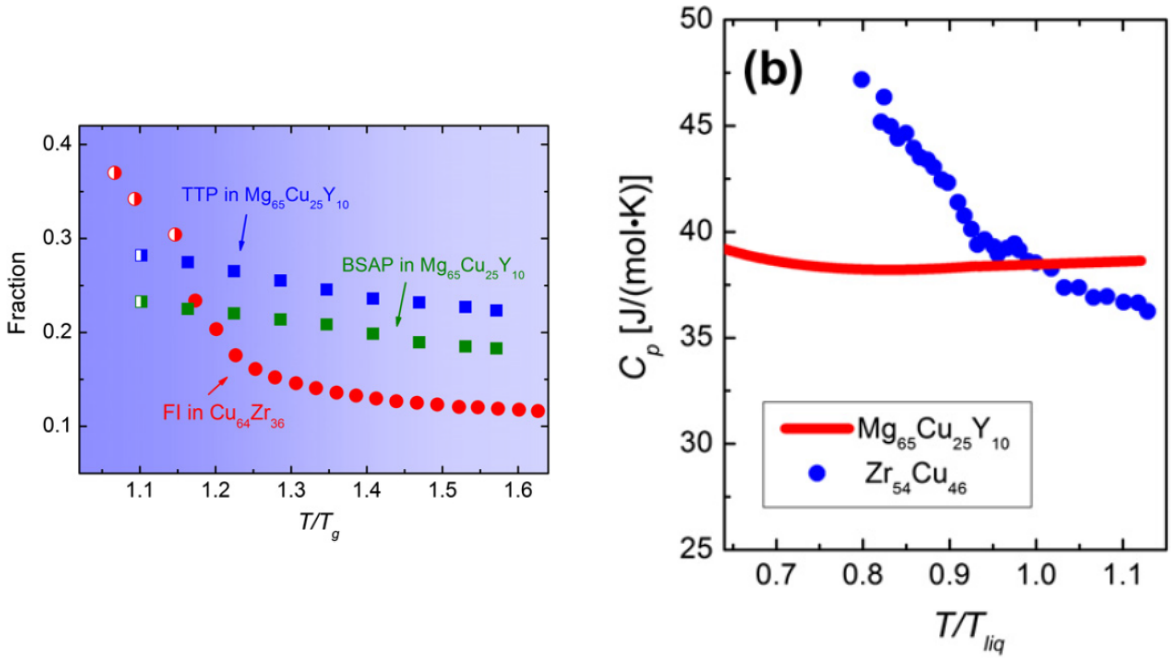

Figure 2.11 Left, fraction of polyhedra as a function of temperature, tetragonal tri-capped polyhedra (TTP) and bicapped square antiprisms (BSAP) are the dominant ordering in $Mg_{65}Cu_{25}Y_{10}$ and full icosahedra (FI) are the dominant ordering in $Cu_{64}Zr_{36}$[24, 25]. Right, heat capacities of the undercooled liquid [24]. It is presented by Ding et. al. that the fraction of ordering directly correlate to the heat capacity behavior.

2.3 Molecular Dynamics Simulations

Given that the goal of MD simulations is the understanding of a system at the atomic level, an efficient way to relate the atoms to each other must be developed. A quantum description (like *ab initio* calculations) would be ideal, however in practice these simulations are difficult to implement even for very small systems [78]. A simple approach, treating individual atoms as point masses connected by 'springs', allows for calculation of greater system sizes [79] although there is generally some loss of accuracy compared to quantum mechanical descriptions. In the field of MD, it is therefore critical to determine an accurate effective potential, the relationship between atoms, through a variety of measurements of which thermodynamic measurements are just one component. These are called semi-empirical potentials, and the goal is that they have the accuracy to reproduce experimental data but still have the large sample size and longer

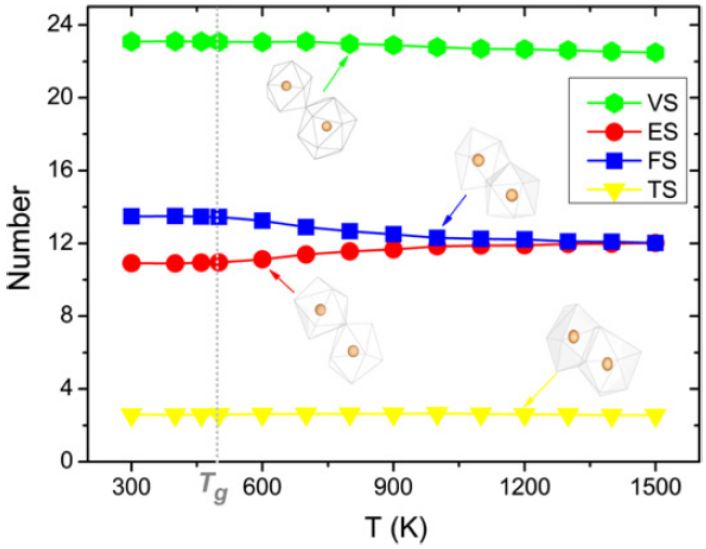

Figure 2.12 The average number of connected structural motifs, from vertex sharing (VS), edge sharing (ES), face sharing (FS), and tetrahedral sharing (TS) as a function of temperature, from Ding et. al. [24]. It can be seen that there is no temperature dependence.

available simulation times afforded by an approximation. Many-body interatomic potentials such as the embedded atom method (EAM) [80] or Finnis-Sinclair [81] method are commonly used to retain accuracy without sacrificing computational ability.

The embedded atom method is based on the quasiatom theory [82] which defines the energy of a quasiatom as [80]:

$$E = E_Z(\rho_h(R)) \tag{2.9}$$

where $\rho_h(R)$ is the electron density of the host without impurity at R, the site the impurity is placed, and E_Z is the quasiatom energy of an impurity with atomic number Z [80]. Daw and Baskes treat all atoms as being embedded in a host consisting of all other atoms, with the embedding energy being density dependent (which has the advantage of always being definable)[80]. In their 1984 paper, Daw and Baskes use perfect crystal data to fit their semi-empirical potential. Mendelev et. al. present that perfect crystal potentials are ineffective in simulating liquids or situations that deviate from perfection (dislocations, grain boundaries, etc.) and that liquid data can be used to fit potentials [83]. The main thermodynamic comparisons are that of the melting point, and thermal expansion [84], with some groups also

comparing the Gibbs free energies [26] and enthalpies (such as enthalpies of melting [85, 86], mixing, and formation [87]). An example of a thermodynamic comparison can be seen in Figure 2.13.

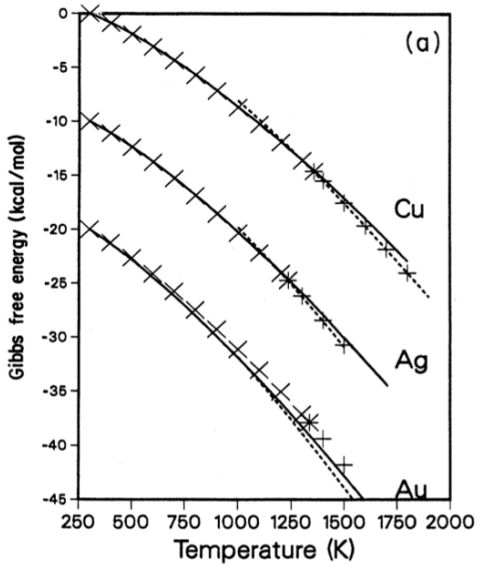

Figure 2.13 Thermodynamic comparison by Foiles et. al [26]. Solid curves are calculated for crystal, dashed for liquid. Symbols are experimental values.

Monte Carlo simulations can be used to determine the enthalpy of solid and liquids, but these generally do not include quantum effects so low temperature calculations require qausi-harmonic calculations [84]. Quasi-harmonic calculations can not be applied to higher temperatures because the thermal vibrations are large enough that the harmonic approximation is not accurate. In the Structures and Dynamics group at Ames Laboratory, development of potentials has been improved by considering liquid diffraction data, as well as thermodynamic properties of liquids such as the enthalpy of mixing, and liquid density [88, 89]. The consideration of the thermal expansion is important because it tests the anharmonic portion of the interactions [84], as the complete harmonic interactions yield zero thermal expansion. The undercooled liquid heat capacity can also be calculated for comparison, although generally it is difficult to have agreement between MD enthalpy measurements and experimental [90].

In summary the most valuable thermodynamic measurements for Molecular Dynamics simulations are:

- Measurements of Gibbs free energies, enthalpies of mixing, and liquid densities to refine potentials and serve as a comparison to the calculated values to ensure that the simulation reflects reality.

2.4 Principles of Thermodynamic Measurements

In this section, the principles of thermodynamic measurements will be reviewed, with experimental methods being described in the next chapter. The utility of each experimental method, calorimetry, vapor pressure, and electromotive force, arises from their definition in relation to known thermodynamic principles. The main goal of thermodynamic measurements for metal alloys is generally is the determination of partial or integral values of the Gibbs free energy, the enthalpies of formation and mixing, as well as heat contents as a function of temperature and composition [54]. The enthalpy of the undercooled liquid is of particular value for analyses with respect to glass formation, as was just described. This section will summarize the experimental pathways to access the Gibbs free energy, from the various definitions of Gibbs free energy. For metals, almost all experiments are carried out at constant pressure. Computational techniques and examinations of gases can be carried out at constant volume, however [91].

Calorimetric techniques are used to establish integral and partial enthalpies, but are limited when determining partial Gibbs free energy, and the related activities [62]. Second law methods such as electromotive force measurements and vapor pressure measurements are used to determine partial free energies of reaction (mixing or formation) [92].

2.4.1 Calorimetry

Considering the change of Gibbs free energy, ΔG, and its definition,

$$\Delta G = \Delta H - T\Delta S, \tag{2.10}$$

if ΔH, the change in enthalpy, T, the temperature in Kelvin, and ΔS, the change of entropy, were known, it would be possible to calculate the Gibbs free energy difference at one temperature, T. How then can we obtain ΔH and ΔS (and their relationships with composition and temperature) to determine the free energy?

If we then consider that the direct measurement of entropy is not practically possible it becomes evident that measurement of enthalpy is instead the only pathway to obtaining the Gibbs free energy in this definition. While direct measurements of entropy are practically limited, as a result of the third law of thermodynamics (at absolute zero the entropy of an ordered system should be zero) the entropy at a temperature T can be determined:

$$S(T) = \int_0^T \frac{C_p}{T}\, \mathrm{d}T \tag{2.11}$$

in which C_p is the constant pressure heat capacity. The constant pressure heat capacity as a function of temperature can determined by the measurement of enthalpy:

$$C_p = \frac{\delta Q}{\delta T} = \frac{\delta H}{\delta T}. \tag{2.12}$$

From the first and second laws of thermodynamics, every possible substance has a fixed value of H and S. If we define the formation of a simple alloy of constituents A and B (in their standard states), and amounts j and k [93] as $jA + kB = A_jB_k$, the resulting change of the enthalpy can be represented by:

$$\Delta H_f = H_{A_jB_k} - (jH_A + kH_B) \tag{2.13}$$

where H_A and H_B are the standard state enthalpies of the pure components and ΔH_f is defined as the enthalpy of formation of the alloy.

Similarly, the enthalpy of mixing can be described in the same manner,

$$\Delta H_{mix} = H_{A_jB_k} - (jH_A^{liq} + kH_B^{liq}), \tag{2.14}$$

where H_A^{liq} and H_B^{liq} are the enthalpies of A and B in their liquid states.

The magnitudes of these quantities reveals information regarding the lattice stabilities of the system. If we consider the potential energy of a system as a function of interatomic radius, seen in Figure 2.14, the depth and width of the well is related to various material properties such as melting point and elastic modulus by virtue of the strength of the bonding. The enthalpies of formation and mixing therefore contain valuable information about the nature of the arrangement of the atoms, for example, one of the empirical rules for glass formation

proposed by Inoue [49] is that glass formation is enhanced with a highly negative enthalpy of mixing. This is thought to improve the formation of short-range ordering as the atoms are more closely related, and a decreased liquid free-volume is thought to have a strong effect on glass formation and tendency of short-range ordering.

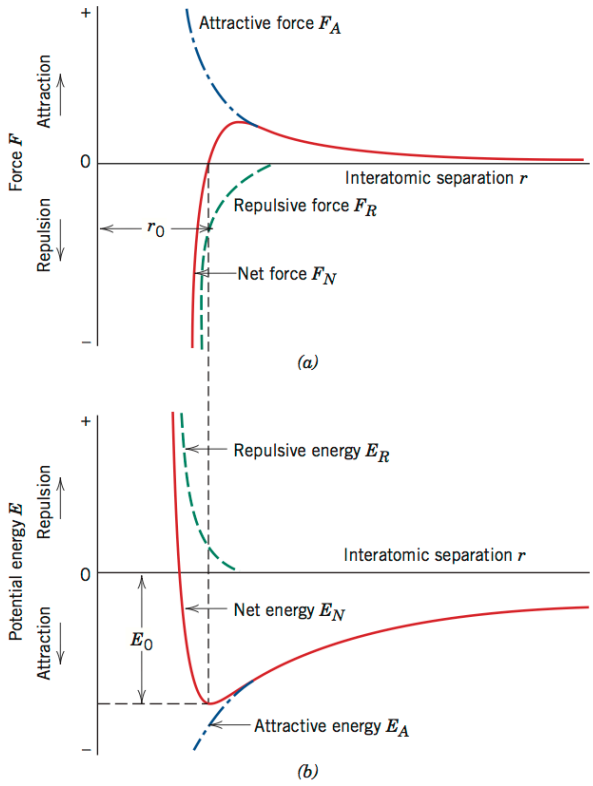

Figure 2.14 For an isolated pair of atoms, the force and potential energy are described as a function of interatomic distance [27]

Both the enthalpy of formation and entropy are usually reported at a temperature of 298.15 K, as a matter of convention these are known as the standard enthalpy and entropy, usually denoted with the standard temperature, e.g. H_{298}, or with a superscript zero, H^0, or both H^0_{298}.

Having both a value for the entropy and enthalpy, it is now possible to calculate the Gibbs free energy:

$$G_{298} = H_{298} - TS_{298}. \tag{2.15}$$

Often, free energy data for temperatures beyond 298.15 K are desirable, in which heat capacities

must be considered:

$$\Delta G(T) = \Delta H_{298} + \int_{298}^{T} \Delta C_p \, \mathrm{d}T - T\Delta S_{298} - T \int_{298}^{T} \frac{\Delta C_p}{T} \, \mathrm{d}T \tag{2.16}$$

and if there are any transformations in the temperature region 298.15 K to T, enthalpies and entropies of phase transitions must be considered.

2.4.2 Second-Law Methods

The second-law methods, vapor pressure and e.m.f, are elegant in their simple description and access to the Gibbs free energy. These methods, however, present substantial experimental challenges.

If we consider another definition of the free energy for a reaction,

$$\Delta G = G_{products} - G_{reactants}, \tag{2.17}$$

where ΔG represents the maximum work done in the reaction at a constant pressure [93], it is clear that in the case of a reversible reaction if the relationship between products and reactions is known, the Gibbs free energy can be determined. The work of van't Hoff, Nernst, and others lead to the development of the relationship of free-energy and an equilibrium constant [94]:

$$\Delta G = -RT \ln K, \tag{2.18}$$

where R is the universal gas constant, T the temperature, and K the equilibrium constant.

2.4.2.1 Vapor Pressure Methods

If we now consider a pure metal in a solid state at some high T, the formation of some finite vapor is the only product. Thus the Gibbs free energy can be determined by measuring the partial pressure of the vapor formed:

$$\Delta G = RT \ln(p). \tag{2.19}$$

When considering an alloy, if an adequate temperature is chosen in which only one component is volatile, it is possible to compare the pressure of the volatile component to that of

the pressure generated by that same component in its pure state to obtain the activity of that component in the alloy [54, 95]:

$$\Delta\overline{G}_i = RT \ln \left[\frac{P_i}{P_i^o}\right] = RT \ln a_i \tag{2.20}$$

where $\Delta\overline{G}_i$ is the partial Gibbs free energy of component i, P_i is the pressure of the component in an alloy, P_i^0 the pressure of the pure component at the same T, which is then the activity, a_i of component i in the alloy. Activities describe a relation for the solution compared to the ideal case, which is useful when calculating the mixing of pure components.

2.4.2.2 Electromotive Force Methods

Electromotive force methods are based on the work of Gibbs in 1876 for the definition of a reversible (perfect) electrochemical apparatus [96]:

$$V_2 - V_1 = -\frac{\mathrm{d}\zeta}{\mathrm{d}e} \tag{2.21}$$

in which V represents a potential, de is an infinitesimal quantity of electricity, and dζ the change in isothermal-isobaric free energy (related to Gibbs free energy).

Later the relationship was presented in the most practical form by the work of Lewis, et al [97]:

$$\Delta G = -z \cdot F \cdot E \tag{2.22}$$

in which zF represents a charge transfer, z being the valence and F the Faraday constant, and E is the electromotive force produced by the cell. This relationship represents the amount of work that is required in a galvanic cell to transfer one mole of a pure element to a solution or compound. This implies some experimental challenges in realizing the technique, which will be discussed in Chapter 3. With a suitable electrode, the description of galvanic cells is generally described as follows:

$$A \mid \text{ionic electrolyte} \mid A_xB_{1-x} \tag{2.23}$$

where A and A_xB_{1-x} represent some component and alloy, either of which can be solid or liquid.

The electromotive force in the cell is therefore related to the partial Gibbs energy (or activity) of A [1]:

$$\Delta\overline{G}_A = -zFE = RT \cdot \ln\, a_A \tag{2.24}$$

where a_A is the activity of A in A_xB_{1-x}. It is now evident that both vapor pressure and e.m.f techniques are used to measure the partial activities of components, from the same definition (Equation 2.18).

If the EMF voltage can be monitored as a function of temperature, the partial enthalpy,

$$\Delta\overline{S}_A = ZF\left(\frac{\partial E}{\partial T}\right), \tag{2.25}$$

and entropy can be determined [54],

$$\Delta\overline{H}_A = ZF\left[T \cdot \left(\frac{\partial E}{\partial T}\right) - E\right]. \tag{2.26}$$

The conventional methods for obtaining free energies can be summarized as follows:

- Free energies may be calculated from heats of formation, entropies, and specific heats using the relationships described in subsection 2.4.1.
- Free energies can be determined by combining partial measurements, which are obtained directly from the measurement of equilibrium constants (partial pressures or e.m.f) as described in subsection 2.4.2.

2.5 Conclusions

From the literature reviewed here and analyses reported, the following conclusions can be drawn regarding the role of thermodynamic measurements to elucidate glass formation:

- The specific heat capacity of the undercooled liquid provides insight regarding the structural nature of the liquid, which underpins the behavior the liquid and the associated potential formation of metallic glasses.
- The specific heat capacity of the undercooled liquid enables calculation of the Gibbs free energies, enthalpies, and entropies of the undercooled liquid, which can be used to calculate T_0 curves to identify thermodynamically viable compositions of glass formation. The

entropy of the undercooled liquid can be used to calculate the Kauzmann temperature, or ideal glass transition temperature.

- A variety of behaviors for the temperature dependence of the undercooled heat capacity have been reported, where, in general, strong liquids have a weak temperature dependence and fragile liquids have been reported with both no temperature dependence and second order temperature dependence. Fragile liquids also generally display a peak in the heat capacity prior to the glass transition. MD simulations reveal that the small temperature dependence in strong liquids is a result of a high degree of ordering at the melting point, thus the degree of ordering does not increase considerably on cooling, and that fragile liquids undergo a large degree of ordering prior to the glass transition.

- Enthalpies of mixing, liquid density, and thermal expansion measurements are useful for development and comparison of MD potentials.

CHAPTER 3. Traditional Experimental Techniques for Thermodynamic Measurements

3.1 Introduction

As described in Chapter 2, the most widely used thermodynamic techniques are based on the analysis of heats, calorimetry, and the second-law methods consisting of electromotive force and vapor pressure techniques. A brief historical perspective will be given.

The roots of modern calorimetry can probably be linked to Joseph Black. Black described his first experiments in the 1760s for what is now known as specific heat by placing a cubic inch of iron and wood into an oven and realized that the iron felt hotter and continued to feel hotter for longer [98]. Black made the important distinction between temperature and heat, however it was not until the works of James Joule in 1850 that heat was proven as a form of energy rather than matter, and that a given amount of work could be converted to heat [99]. Indeed, the accurate quantitative study of heat is a relatively recent phenomenon which is often marked by the publication by White regarding the construction and operation of calorimeters [100]. In time, those desiring to obtain thermodynamic data extended beyond those who exclusively studied heat and the increased demand and usage lead to commercial offerings and adoption of thermal analysis techniques to many subsets of physical science [93, 101]. Use of thermal analysis techniques has since expanded to many everyday aspects of our lives such as: determination of drug purity [102], food labels [103, 104], and of course extensive use in materials processing [105, 106, 107].

Both the vapor pressure methods and the electromotive force methods are related, in that they are both defined from the natural tendencies for systems to move towards equilibrium and maximum entropy (the second law of thermodynamics). In both methods, the free energy

is measured by attaining a reversible equilibrium and determining the driving force for the equilibrium. In his publication *On The Equilbrium of Heterogenous Substances* Gibbs described a perfect reversible electrochemical cell in which the potential of the cell was related to the isothermal-isobaric free energy [108]. Helmholtz then derived the function in terms of Helmholtz free energy in his publication in 1882. In 1886 van't Hoff proved that work was related to an equilibrium constant through his "equilibrium box" thought experiment [109], which could then later be related to the free energy change. Nernst developed the relation between electromotive force and free energy in 1889 [110]. Thus at this point, there were two working definitions to measure the free energy, however, at this time, researchers had difficulty applying ideal thermodynamic theories to real solutions and gases [109]. Lewis developed the concept of the activity in 1907 [111] (as well as fugacity in 1901 [112]), and then along with Randall, measured free energies for 25 years to publish one of the most important texts in thermodynamics [97].

3.2 Calorimetric Methods

The use of thermal analysis techniques to analyze metals (and therefore metallic glass forming alloys) generally requires higher temperatures which introduces several experimental obstacles such as oxidation, reactivity of crucible materials, small size of experimental heat effect compared to background, and potential non-uniform vaporization. A number of excellent reviews of high temperature calorimetry for metallic systems available [113, 114, 115] as well as more focused reviews targeting reaction (solution) calorimetry [116, 117, 54]. In general, the non-reaction calorimetric methods are applied to measure heat capacities, and enthalpies (including transformation enthalpies). Reaction calorimetry methods are applied to measure heats of formation and mixing.

Calorimetric methods are among the most popular for obtaining thermodynamic data, along with electromotive force measurements. When choosing a calorimetric technique to obtain thermodynamic measurements, it is worthwhile to understand the principles of the techniques and limitations. Each calorimeter type is generally suited for different tasks, and each handle three aspects of calorimetry differently: T_c, the temperature of the calorimeter, T_s the temperature of the surroundings, and Q the heat produced per unit time. Each technique

is primarily concerned with eliminating or properly accounting for heat leakage.

The classification of calorimeters is in itself somewhat of a challenge. There have been many attempted methods to classify calorimetric methods [93, 101, 118, 119, 120, 114]. I found the most logical classification presented by Rouquerol and Zielenkiewicz [119] in which the main distinction is between adiabatic, "ordinary", and isothermal. Defining the total heat as the sum of accumulated heat and exchanged heat [119],

$$Q_{total} = Q_{accumulated} + Q_{exchanged}, \tag{3.1}$$

where $Q_{accumulated}$ describes heat that is contained within the calorimeter, and $Q_{exchanged}$ describes heat that is transferred with the surroundings. This description allows for the distinction between the three types to be quite natural. The first being those in which $Q_{total} = Q_{accumulated}$ and there is no heat lost, described as perfect adiabatic. The converse, in which $Q_{total} = Q_{exchanged}$ represents a perfect heat flow calorimeter. A calorimeter in which some heat is accumulated and lost is therefore the ordinary calorimeter. This definition, while useful, requires some measure of the quality of a calorimeter, i.e. if an adiabatic calorimeter is not perfectly adiabatic, it is an ordinary calorimeter.

Rouquerol and Zielenkiewicz went on to present the main criteria based on how the calorimeter vessel and shielding temperatures are handled [119]:

i) Adiabatic types have traditionally maintained a temperature control such that the temperature of the calorimeter block and shielding are measured and the shield temperature follows that of the vessel via some power compensation ("sample following"). For example, after a heat introduction, the shield temperature rises to match that of the calorimeter temperature to minimize heat leakage, i.e. the shield follows the sample temperature.

ii) Ordinary calorimeters maintain no fixed or controlled relationship between the calorimeter block and the shielding, but the shielding is generally maintained at a constant temperature. These are also referred to as Isoperibolic.

iii) Isothermal calorimeters are opposite to adiabatic, in that the calorimeter follows the shielding temperature ("shield following"). An ice bath in contact with the calorimeter would fit

this description, where after an introduction of heat the calorimeter temperature follows the shield.

Adiabatic calorimeters are well suited for reactions that are relatively slow [93] as the adiabatic condition can be maintained for extended periods of time to measure long reactions. If the reaction rate exceeds the rate at which the calorimeter-shield temperatures can be matched, the adiabatic condition is no longer achieved. Additionally, as the operating temperature increases the adiabatic condition becomes more difficult to maintain [121].

Isothermal calorimeters maintain the calorimeter and the shielding at the same temperature, which is constant even with the introduction of heat. The constant temperature is maintained by either a phase-change of a material (ice calorimeter for example) or by some external compensation [114]. An ice calorimeter can be used in the following way, the sample is dropped into a calorimeter which is insulated with ice. The heat produced from the sample melts an amount of ice, which can be used to determine the heat of the sample. The use of isothermal calorimeter for the analysis of metals is scarce today, although there has been use for isothermal calorimeters in titration reactions in which the heat evolution is continuously measured.

Isoperibolic calorimeters, in which the term isoperibol is from greek, meaning same (iso) and surroundings (peribol) [114], maintains the temperature of the calorimeter jacket at the same temperature. In comparison to adiabatic or isothermal techniques, there is a finite and well defined thermal resistance in which the heat flows away. Therefore proper usage of the technique involves consideration of the heat leakage.

Accurate calorimetry does not rely on elimination of all heat leakage if the heat leakage flows away in a manner of the known physical laws [100]. The physical laws governing the heat loss in a calorimeter system are often assumed to obey newtonian cooling, where the rate of heat leakage, $\frac{\mathrm{d}T}{\mathrm{d}t}$, is proportional to the thermal gradient. As a result of the finite thermal leakage, there also exists some heat leakage during the heat introduction period. For example, the calorimeter apparatus of Schaefers et. al. [28] maintain a constant jacket temperature above the calorimeter temperature, where the temperature of the calorimeter continuously drifts towards the jacket temperature. By fitting the temperature drifting portions of the

curve (process shown in Figure 3.1) and determining the mid point of heat transfer, the true temperature can then be determined by evaluating the temperature of the cooling fit at the time of mid point of heat transfer.

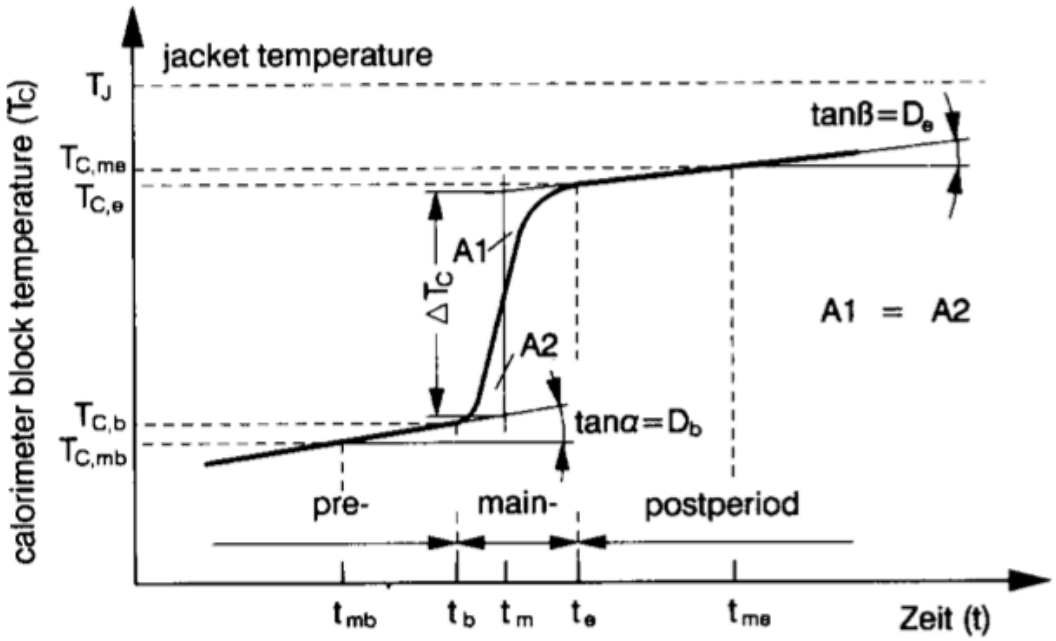

Figure 3.1 Reconstruction of the true temperature increase resulting from heat introduction [28].

Given the vast array of available calorimeters, selecting a calorimeter design depends on several factors related to the experimental goals [114]:

a) The property to be measured, i.e. enthalpy of mixing vs heat capacity.

b) The temperature range to be explored.

c) The size of the thermal effect and required accuracy.

For the determination of heat capacity for instance, all of the calorimeter types have been employed. Considering that many of the types are suitable, it is important to remember that the goal is still to obtain reliable data without wasting effort [116]. The most limiting aspect of selecting a calorimeter type is the temperature range. Luck, Predel et. al reported a

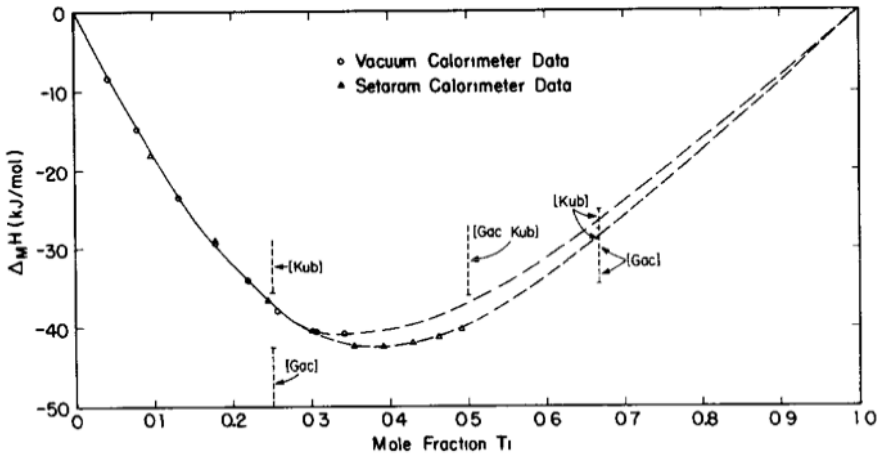

Figure 3.2 Comparison between two calorimeters in the measurement of the enthalpy of mixing of Ni-Ti [29].

comparison between two different calorimeters for the same measurement which is somewhat rare in literature [29] which can be seen in Figure 3.2.

Their comparison was between a rather complex calorimeter, the commercial SETARAM calorimeter (details available in [122]), and a vacuum calorimeter [123]. Their results indicated that chemical factors (especially oxygen and nitrogen reactions) were more critical than simply maximizing accuracy in temperature measurement. These also further confirm some of the experimental challenges with reactions when employing high temperature calorimetry.

3.2.1 Reaction Calorimetry

Reaction calorimetry is used to determine the enthalpy of mixing in liquids, or the enthalpies of formation of phases and compounds. The principle of the technique is that two components are introduced (both of known heat content), the temperature continuously measured and the heat of the reaction (either formation or mixing) is measured. The various calorimeter operating modes described previously apply to reaction calorimetry as well. Calorimeter designs vary due to specific problems in certain systems, such as vaporization of one component: a breakable silica ampoule of one component can be submerged in the liquid of another component and broken [114].

An example of a mixing calorimeter is that of Kleppa's [30], which can be seen in Figure 3.3.

The twin-cell calorimeter in Figure 3.3 can also be operated in a drop method, in which one component is at room temperature [40]. This can be seen in Figure 3.15.

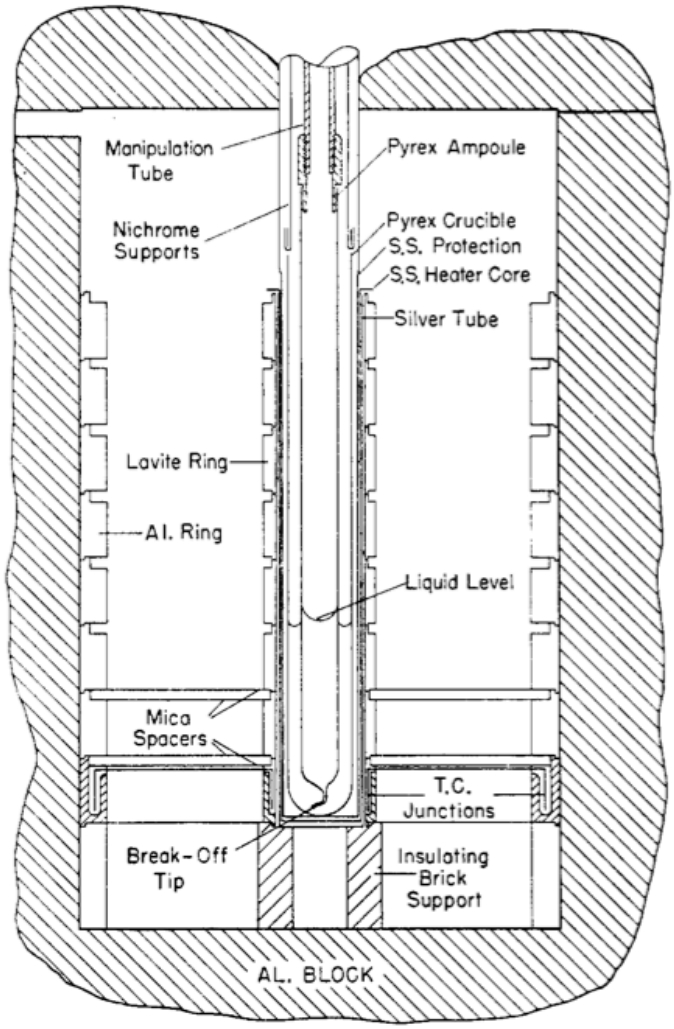

Figure 3.3 One calorimeter cell of Kleppa's mixing calorimeter [30]. It can be seen there are two liquid levels, in which the fine tip of one tube can be broken to initiate mixing.

Clever calorimeter designs which allow for continuous introduction of one component allows for the determination of mixing or formation over a wide composition range in one experiment [54]. Additionally, one component may be liquid, the other at room temperature. If the enthalpy of the sample at room temperature is known it can be added to the liquid and either mixing or formation may be calculated depending if the sample melts or forms a compound.

An example of the calculation of the heat of mixing will now be presented from Itagaki

and Yazawa [31]. First, high purity metal constituents are placed in the calorimeter. Then the calorimeter is evacuated and backfilled with argon. The calorimeter is then heated to operating temperature and held for a period to stabilize. A heat pulse from an electrical calibration method is introduced, and the calibration checked. Then the metal samples are allowed to mix, and the heat response measured. The procedure then involves an introduction of another calibration pulse, and it is checked against the first pulse to ensure accuracy. The heat of mixing is then calculated by:

$$m \cdot \Delta H = W \cdot \Delta T_1, \tag{3.2}$$

where m is the mole amount of the alloy, ΔT_1 is the temperature change related to mixing, and W the water equivalent (calorimeter constant) of the calorimeter. The temperature response of the calorimeter can be seen in Figure 3.4.

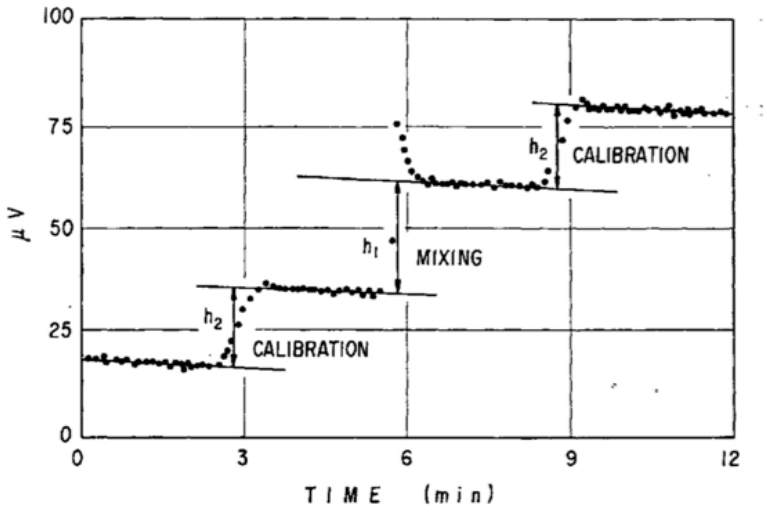

Figure 3.4 Temperature response of a mixing calorimeter to calibration pulses and mixing from Itagaki and Yazawa [31]

Different ratios of the metals are then used for additional experiments to measure the heats of mixing over the composition range desired. This usually requires at least 10 measurements.

3.2.2 Non-reaction Calorimetry

Non-reaction calorimetry is the standard determination of heat contents, without a reaction, such as the enthalpy, heat capacity, and heats of transformation. The main methods used are drop calorimetry, differential thermal methods, and adiabatic calorimeters. In general, differential scanning calorimeters are limited to lower temperatures although there is research in this area to increase the operating temperature [124]. The more general differential thermal analysis (DTA) calorimeters do not have power compensation for well controlled heating/cooling rates but can be extended to higher temperatures. Adiabatic calorimeters also have upper temperature limits, usually around 1500-1800 K. Drop techniques can be extended to very high temperatures (∼3000 K) with the combination of a levitation coil, which is discussed in Chapter 4.

Drop methods have been used to determine the heat contents of metals for over one hundred years [125], as the drop method is a logical conclusion to minimize error from moving a sample from an external furnace to a calorimeter. As mentioned in the previous chapter, the heat capacity is defined as the derivative of the enthalpy with respect to temperature and enthalpy increments are measured with drop calorimetry. Performing several enthalpy measurements at different temperatures will allow for the determination of the heat capacity. Heats of transformation can be determined by performing enthalpy measurements prior to the transformation and after. Two examples of an adiabatic drop calorimeter technique is that of Levinson [32] and Barth, et. al. [33], which can be seen in Figure 3.5.

The furnace component of each differs considerably. The furnace of Barth et. al. is an electromagnetic levitation furnace, the technique which will be further discussed in Chapter 4. The furnace of Levinson is a traditional furnace, which can be seen in Figure 3.6.

Not to be confused with adiabatic drop calorimetry, the principle behind adiabatic calorimetry is the input of energy increments and the measurement of the response of the sample, and because there is no heat loss the change of the heat capacity is then directly related to the energy input[126]:

$$C_p = \frac{\Delta E}{\Delta T} \tag{3.3}$$

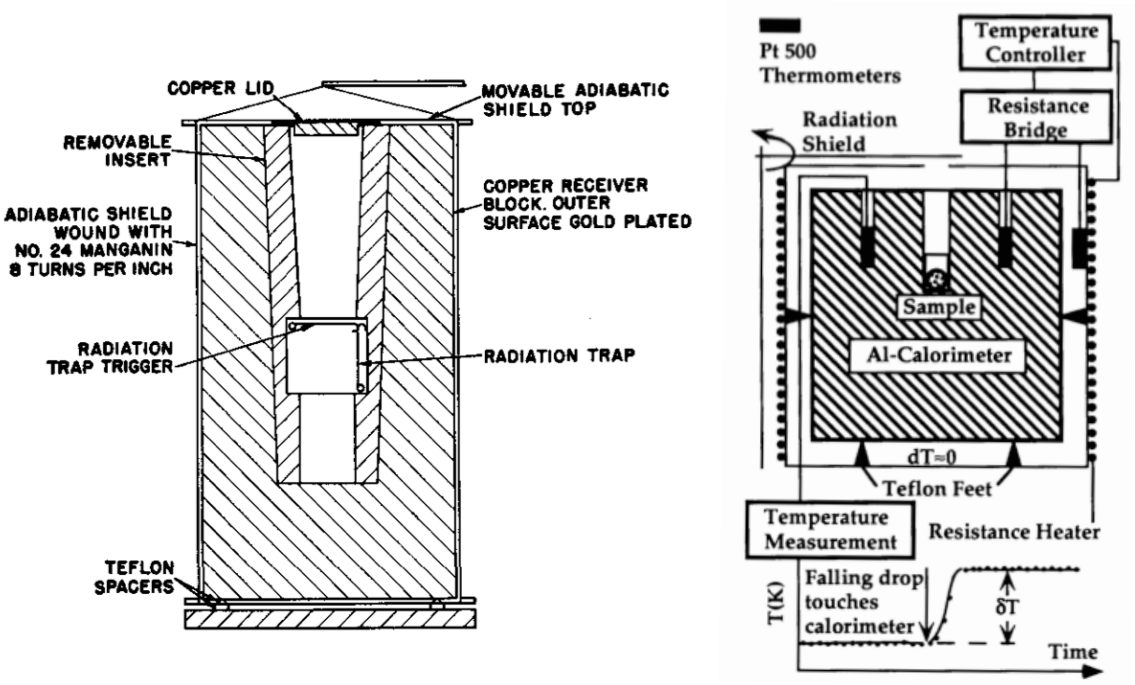

Figure 3.5 Adiabatic drop calorimeter receiving wells which feature "sample following" heating jacket. Left: high temperature drop calorimeter receiving well of Levinson [32]. Right, that of Barth et. al. [33].

where C_p is the heat capacity for the midpoint of the temperature difference ΔT. Ideal adiabatic conditions are not practically achievable, although through complex designs heat exchange with the surroundings can be minimized. Some adiabatic mixing or drop calorimeters can be used as adiabatic calorimeters. An example of this is the calorimeter of Dench et. al. [127], which was developed as a high temperature mixing calorimeter. It was used in this adiabatic method to determine the heat capacity of iron [128].

The two main methods for determining the heat capacity with differential scanning calorimeters are the scanning method and the step-scan method. In the scanning method an empty sample pan is scanned over some temperature range. Then the sample is introduced and scanned over the same range, and after that a reference material of known heat content is scanned over the same range. In each case the empty pan is subtracted, and the heat content of the sample can be compared to that of the reference. In the step-scan method, a series of heat pulses are introduced followed by an equilibration time in which the enthalpy is determined. The heat capacity can then be derived. More information on the step-scan method can

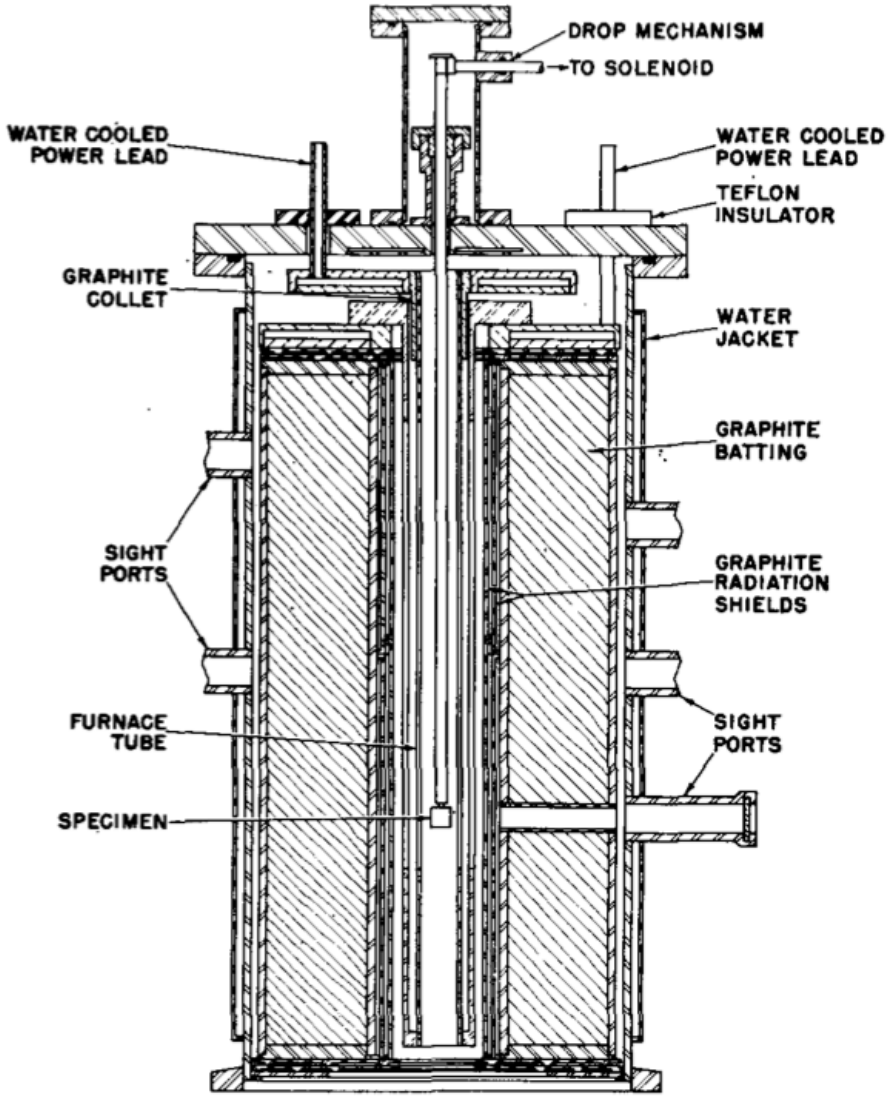

Figure 3.6 High temperature drop calorimeter furnace of Levinson [32]. The sample is connected to a graphite rod, which is notched. A mechanical shock breaks the graphite rod and the sample falls into the receiving well in Figure 3.5.

be found in these publications by Mraw and Naas [129], as well as Cerdeirina et. al. [130]. It is also worth mentioning that this method can be applied in a similar fashion to that of the scan method, in which the empty pan can be subtracted, and a reference material can be used.

3.2.3 Measurements of the Undercooled Liquid

The largest obstacle to obtaining the undercooled liquid is that of heterogeneous nucleation sites provided by a container or substrate. Despite this, there have been several techniques to obtain large undercoolings. Some of these were summarized by Perepezko in 1984 [34] and can be seen in Figure 3.7:

a) fluid dispersion techniques [131, 132]

b) substrate techniques, like that of Turnbull [133, 134] and Vonnegut [135]

c) processing an alloy in a temperature region in which small volumes are generated [136]

d) inorganic fluxing techniques [137]

e) electromagnetic levitation

The substrate techniques were the first studies of liquid metal undercooling of large magnitude. In general, fine powders (10-100 μm diameter) were placed on heated silica slides, melted, and cooled by allowing the melts to cool radiatively or flowing helium [138]. The melted droplets were observed with optical microscopy and nucleation could be determined when the surface texture changed as a result of solidification. Higher undercoolings were obtained by emulsification techniques, likely due to the potency of the substrate in previous investigations. Indeed, the work of Turnbull and Hoffman showed that surfaces can dramatically reduce the energy barrier to form a critical nucleus [134, 61]. Emulsification techniques better isolate the effect of surfaces and internal catalysts. The fluid dispersion techniques are based on the principle of dividing the bulk volume of a melt into small parts, which would isolate inherent nucleants, and the surface potency is reduced by the addition of a surfactant that reacts with the metal droplets to form a coating that has a low catalytic potency [139]. The emulsification technique can be seen in Figure 3.8.

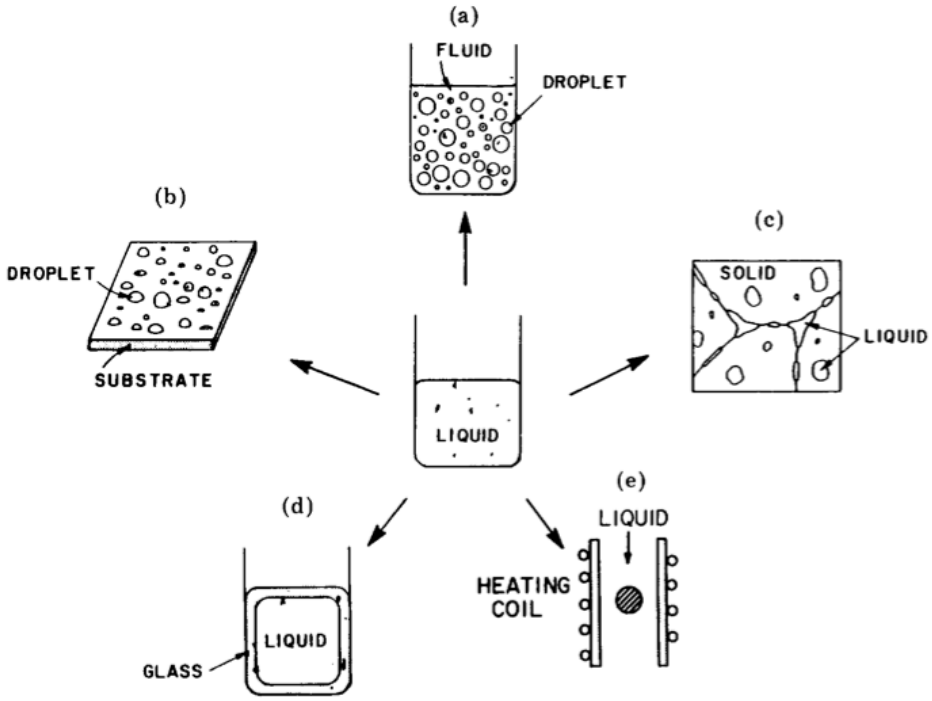

Figure 3.7 Summary of techniques for attaining the undercooled liquid from Perepezko [34].

The metal regions are isolated by using a stirring motor in an inert atmosphere, and additional chemicals are added to the mixture that react with the surface of the isolated metallic droplets to reduce the surface potency, as well as ensure that the metallic regions are not continuous. The highest undercoolings can be achieved when the melts can be divided into the smallest regions possible. This technique is generally limited to 400-500°C for organic oils, however the technique has been demonstrated using molten salts as the carrier fluid to undercool cast-iron [140]. Vonnegut used emulsification techniques in conjunction with XRD to determine the period for which an emulsification mixture was liquid or solid, and determined that the mixture could be undercooled and the rate at which the XRD signal indicated crystallinity was proportional to the nucleation rate [135]. These studies analyzed higher undercoolings within the framework of classical nucleation theory [141].

Thermodynamic properties of the undercooled liquids were generally not measured until the use of DSCs became more prominent [69, 142, 143]. Dispersion and fluxing techniques have been used with success to obtain the heat capacity of undercooled melts using DTA

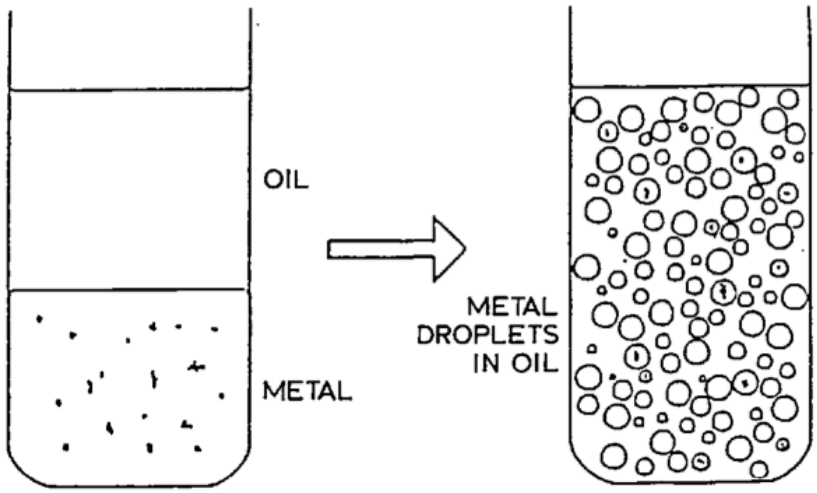

Figure 3.8 Principle of fluid dispersion technique, where catalytic sites are isolated and allowing for large undercooling in the bulk of the metallic droplets [35].

or DSC [139, 3, 144], although it requires careful accounting of the emulsification or fluxing medium. Additionally, the technique in general is limited to lower temperatures, both of the emulsification medium (generally organic oils) or fluxing agent and the DSC or DTA. Another common technique is heating an already amorphous sample and measuring the heat capacity continuously. This requires consideration of the time and temperature rate dependent effects of devitrification. For example, Johnson et. al. prepared an amorphous $Zr_{41}Ti_{13}Cu_{13}Ni_{10}Be_{23}$ sample and devitrified the sample *in-situ* using DSC [21] which can be seen in Figure 3.9. In general, *in-situ* devitrification results in a limited temperature range where the liquid resists crystallization and the heat capacity can be measured. This then requires measurement of the higher temperature liquid heat capacity to connect the data.

Since Perepezko's summary in 1984, there have been a number of other containerless techniques developed such as electrostatic, aerodynamic, and acoustic levitation as well as drop-tube and microgravity experiments which have been included in a review by Herlach et. al. [35]. With respect to the levitation techniques, the heat capacity can be obtained in several ways. The sample can be dropped into a calorimeter (outlined in the next chapter), or if free cooling conditions are possible (limited to ESL [36]), measurement of sample temperature as a function of time along with consideration of Planck's law results in determination of the heat capacity

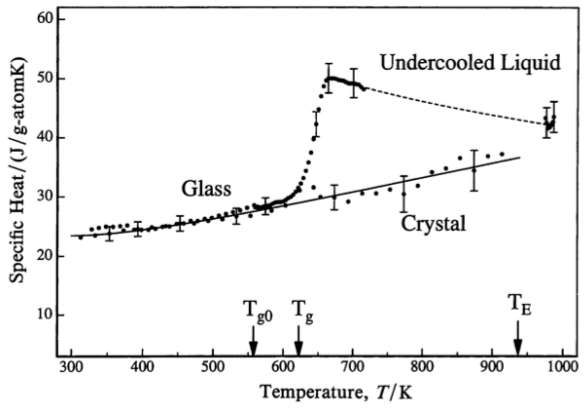

Figure 3.9 Heat capacity measurements of $Zr_{41}Ti_{13}Cu_{13}Ni_{10}Be_{23}$ in the crystalline, glassy, undercooled liquid and liquid state [21].

as radiation is the only energy loss. Additionally, the sample can be levitated in microgravity and modulated RF power applied (TEMPUS project [145],[146]) where the heat capacity of the sample can be determined from the observed thermal response.

In free cooling conditions, the heat capacity of a sample is related to Planck's law [36],

$$mC_p(T)\frac{dT}{dt} = -\epsilon_T(T)A\sigma(T^4 - T_s^4), \tag{3.4}$$

where m is the sample mass, $C_p(T)$ the heat capacity as a function of temperature, $\epsilon_T(T)$ the hemispherical total emissivity as a function of temperature, A the surface area of the sample, σ the Stefan-Boltzmann constant of value 5.67×10^{-8} J S^{-1} m^{-2} K^{-4}, T the sample temperature, and T_s the temperature of the surroundings. The hemispherical total emissivity is generally not known. Thus researchers can report C_p as a function of ϵ_T, or in some cases measure ϵ_T to obtain the heat capacity. In the work of Busch et. al., a glassy Zr-based BMG was devitrified *in-situ* to obtain the heat capacity to obtain ϵ_T. Their results can be seen in Figure 3.10. The more ideal case is that in which the total hemispherical emissivity can be measured directly, however laser reflectance techniques are not commercially available, requiring considerable effort into their construction and calibration [147].

In general, container less processing provides several advantages compared to emulsification and fluxing techniques. The techniques are inherently high purity, for example, in EML, electromagnetic convection continuously exposes the liquid to either high vacuum or some inert

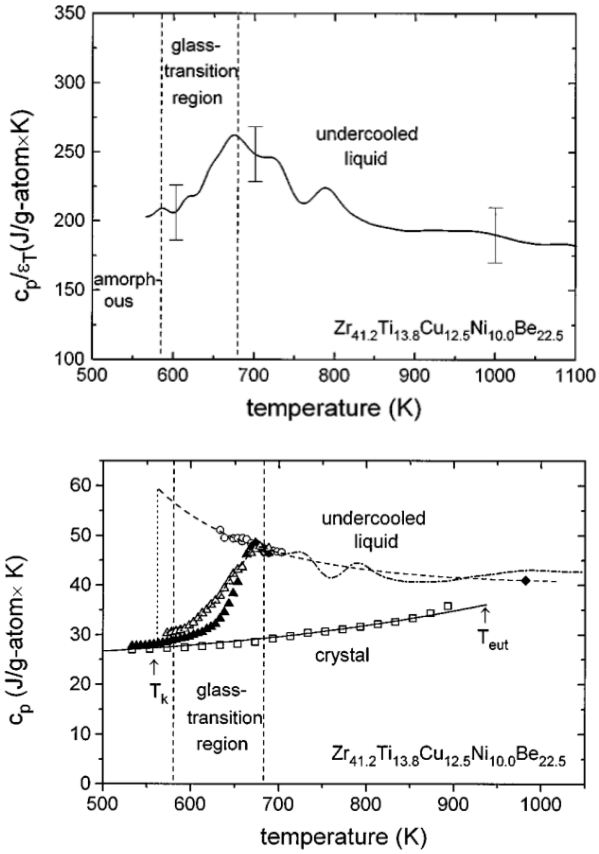

Figure 3.10 Free cooling method to obtain the undercooled heat capacity. Top, measured C_p/ϵ_T for a free-cooled $Zr_{41.2}Ti_{13.8}Cu_{12.5}Ni_{10}Be_{22.5}$ alloy. Bottom, measured heat capacity from DSC and free cooling curve. Both figures from [36].

atmosphere. The stirring velocity can be seen in Figure 3.11, where it can be seen that the stirring effect continuously exposes the internal liquid to the surface.

Electrostatic levitation is restricted to high vacuum due to the high potentials applied. Either high purity atmosphere is an advantage in the reduction of impurities that may act as nucleation sites. The other primary advantage is that the undercooling ranges can be of large magnitude, and are continuous. The next chapter details the use of EML drop calorimetry for the measurement of the undercooled heat capacity.

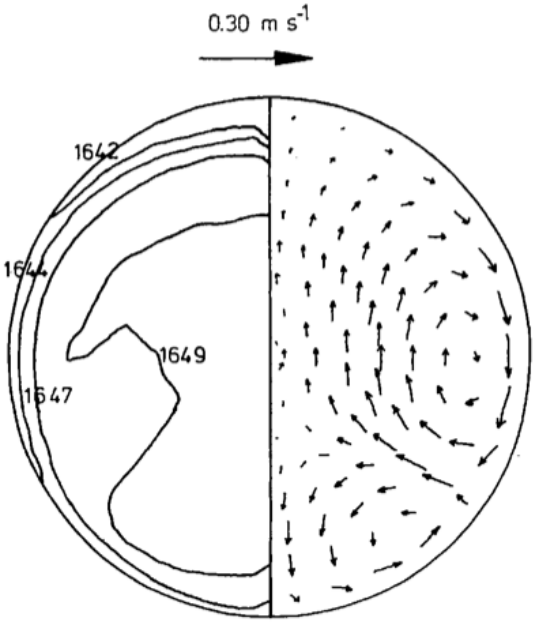

Figure 3.11 Calculated temperature fields (left) and velocity fields for a 6mm diameter Fe sphere [37].

3.3 Electromotive Force Methods

Recalling from chapter 2, that the amount of work that is necessary for a cell to transfer one mole of an element (at valence z) to a solution or compound is related to the Gibbs free energy by

$$\Delta G = -z \cdot F \cdot E, \tag{3.5}$$

where F is faraday's constant, and E is the electromotive force in the cell. As mentioned previously, the cell must operate in a perfectly reversible fashion. This is generally represented by the requirement that there is no external current flowing, requiring measurements to be made on an open circuit with high resistance measuring devices [1]. The main challenges for setting up an e.m.f measurement are [148]: finding a suitable electrolyte, and the identification of the single reversible process at each electrode. There must only be a single reversible process because the ions must have one valence to use in the calculation. Additional challenges involve the materials involved in the construction of the cell, temperature gradients, vaporization of any component, and any reaction other than the one being studied [62, 149].

The electrolyte must be purely ionic, as the definition of the method requires transfer of ions being the only reaction ideally of only one species [150]. It is possible to correct for cells in which there is also electronic conduction, although in general it is desirable to minimize this effect.

With a suitable electrode, the description of galvanic cells is generally described as follows:

$$A \mid \text{ionic electrolyte} \mid A_xB_{1-x} \tag{3.6}$$

where A and A_xB_{1-x} can be solid or liquid.

The electromotive force in the cell is therefore related to the partial gibbs energy (or activity) of A [1]:

$$\Delta\overline{G}_A = -zFE = RT \cdot \ln a_A \tag{3.7}$$

where a_A is the activity of A in A_xB_{1-x}.

Selection of the electrolyte is a critical part of an electromotive force measurement. Aqueous solutions of ions seem obvious as ions have much greater diffusion in liquids. The reality of the situation is that as temperatures are increased, it becomes more likely for a liquid component to become volatile rendering the measurement uncertain. Liquid electrolytes have been used up to about 200 ^{0}C by Babanly et. al. who used Ti^+ in glycerol solutions [151]. The first use of the technique to determine thermodynamic data with solid electrolytes was done by Kiukkola and Wagner in 1957 [152], in which they used oxide cells to determine the Gibbs energies of the formation of oxides. There were several demonstrations of solid oxides before this, however the work by Kiukkola and Wagner was the first use in thermodynamic measurements using them. Solid oxide cells can generally used at higher temperatures and thus are generally more useful to metallurgical thermodynamics. Ionic conductivity in solid electrolytes is usually caused by lattice defects, which can result from a variety of conditions [1]:

- Doping the electrolyte, leading to vacancies in the lattice (YSZ, explained later),
- large cation disorder (Ag-I),
- low packing density structures (tunnel or layered, β-alumina),

Table 3.1 Examples of some solid electrolytes suitable for use in metallurgical thermodynamics studies [1]

Material Base	Conduction Type	Example
Oxide	Anion	ZrO_2, HfO_2, ThO_2, Bi_2O_3, $CaZrO_3$
	Cation	β-alumina, β''-alumina, Pyrex, fused silica, $SrCeO_{3-\delta}$
Halide	Anion	MgF_2, CaF_2, SrF_2, BaF_2, PbF_2, LaF_3, $BaCl_2$
	Cation	CuCl, α-AgI, Ag_3Si, $RbAg_4I_5$
Oxyhalide	Anion	LaOF
Sulfide	Cation	CaS, MgS
Sulfate	Cation	Li_2SO_4, Na_2SO_4, K_2SO_4
Complex oxide	Proton	$SrCeO_3$, $BaCeO_3$, $CaZrO_3$, $SrZrO_3$
Other	Cation	NASICON ($Na_3Zr_2Si_2PO_{12}$), LISICON ($Li_{14}Zn(GEO_4)_4$)

- amorphous materials or network structures (NASICON, etc.).

A list of types of solid electrolytes from a recent review by Ipser [1] will be described in Table 3.1.

An example of an cell setup and EMF measurement will now be described from Jacob et. al. [38]. The activities of Rh in Pd-Rh were measured between 950-1350 K with the following cell:

$$\text{- Rh, } Rh_2O_3 \mid Y_2O_3 + ZrO_2 \mid Pd_{1-x}Rh_x, RH_2O_3 +$$

where it can be seen the electrode was a Yttria Stabilized Zirconia (YSZ) type. The experimental apparatus can be seen in Figure 3.12. The procedure used has been used by others [153].

The oxygen ion transfer follows:

$$O_{2\ alloy} \rightarrow O_{2\ pure\ Rh}$$

Thus the EMF can be measured by:

$$E = \frac{-RT}{4\mathrm{F}} \ln \left[\frac{P_{O_2\ pure}}{P_{O_2\ alloy}}\right] \tag{3.8}$$

where P_{O_2} is the oxygen potential measured (by comparing the oxygen partial pressures in each tube), and the valence is four for two oxygen ions. The partial Gibbs free energy can be obtained once E is known,

$$\Delta\overline{G}_{\mathrm{Rh}} = -3\mathrm{F}E = RT\ln\, a_{\mathrm{Rh}}, \tag{3.9}$$

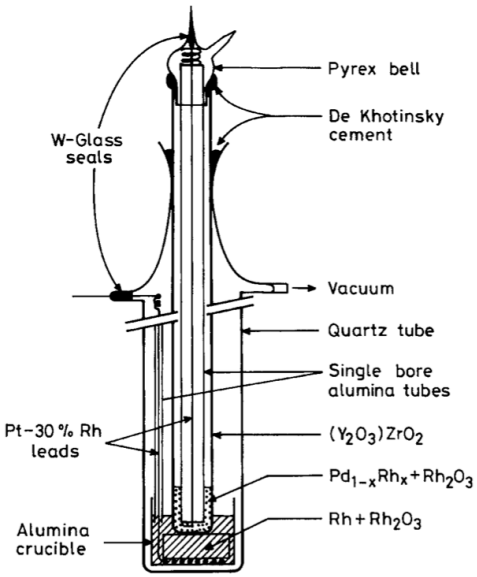

Figure 3.12 Schematic diagram of the galvanic cell used by Jacob et. al. [38]. It can be seen that the two evacuated tubes are connected by the electrical leads. The oxygen pressures are compared in each tube once equilibrium is established.

where the valence is 3 because Rh exists as Rh^{+3} in Rh_2O_3.

3.4 Vapor Pressure Measurements

A heterogenous phase equilibrium including a gas phase has been used as a convenient way to determine the Gibbs free energy of a substance. The goal of vapor pressure techniques are to determine the partial pressure of the gas species in equilibrium with a solid, from which free energy changes and activities of components can be obtained [154, 149].

The main applications of vapor pressure techniques are gas equilibration, and Knudsen effusion (after M. Knudsen [155, 156, 157]). Of the two, Knudsen effusion has been used the most in the application to metallurgical thermodynamics and will be discussed here.

The Knudsen cell is a small cylindrical crucible, containing an equilibrium between a condensed material and a gas phase, in which a small hole (0.1 to 1mm) exists [115]. The principle of the technique is in the small hole, in which a small amount of the gas phase effuses out of the cell, with the assumption that the flow does not disturb the equilibrium in the cell. Additionally the cell contains a thermocouple or port for pyrometric temperature determination.

Knudsen developed a relation for the effusing gas [155],

$$p = \frac{\Delta m}{ks\tau}\sqrt{\frac{2\pi RT}{M}}, \tag{3.10}$$

where Δm is the mass loss during a time τ, M the molar mass of the vapor, s the cross-sectional area of the orifice, and k the Clausing probability factor. The Clausing probability factor can be calculated by the geometry of the orifice [158]:

$$k = \left[1 + \frac{3l}{8r}\right]^{-1} \tag{3.11}$$

where l is the length, and r the radius of the orifice. It is evident from Equation 3.10 that measurement of the mass can lead to the determination of the pressure, when the effusion period is known. This has been done by da Silva et al. in the study of crystalline organic compounds[158, 159], where masses are assessed before and after to an accuracy of ± 0.02mg and effusion times are three to eight hours.

The most modern implementation is that of the combination of a Knudsen cell with a mass spectrometer (first done by Drowart[160]). Based on the fact that the vapor pressure measured by a mass spectrometer is low, the fugacity of a monatomic species is assumed to be equal to its partial pressure [161, 162]. The activity of a component i in the condensed phase is thus [161]

$$a_i(x_i, T) = (p_i/p_i^o)_T \tag{3.12}$$

where p_i and p_i^o are the partial pressures at constant temperature T of the pure component i and the vapor of the component i from the alloy respectively. The requirement of knowledge of the pressure of both the alloy vapor and pure material vapor introduces experimental difficulty.

The pressure is measured by the mass spectrometer method in the following way [95],

$$P_i = \frac{I_i T}{S_i} \tag{3.13}$$

where P_i is the partial pressure of component i, I_i is the measured intensity of the ion beam, and S_i is the sensitivity factor which is dependent on the instrument configuration and experimental conditions. Researchers quickly determined that venting the chamber, and switching the cells could lead to modification of the value of the sensitivity by up to a factor of 3 [161]. There are

several ways to get around this limitation. One simple way is to have a valve to separate the knudsen chamber from the ionization chamber, so that the ionization properties can be held constant. Not all experimental setups can be used in this way.

Another is the ion-current-ratio which relies on a Gibbs-Duhem integration and measurements of ion-current ratios over a range of composition. For some alloy AB, the activity can be described as [163]:

$$\ln \gamma_A = -\int_{X_A=0}^{X_A=X_A} x_B d\left[\ln\left(\frac{I_B}{I_A}\right) - \ln\left(\frac{x_B}{x_A}\right)\right] \tag{3.14}$$

where γ_A is the activity for component A, x_A is the mole fraction of component A, x_B the mole fraction of component B, I_A and I_B the ion intensities for components A and B.

Another method to obtain activities is that of Berkowitz [164], which requires the system have a dimmer-monomer equilibrium:

$$2A(g) = A_2(g). \tag{3.15}$$

The activity is then given by:

$$a_A = \frac{I_{A_2}(alloy) I_A(pure)}{I_A(alloy) I_{A_2}(pure)} \tag{3.16}$$

A modern solution is to use two Knudsen cells in an experimental chamber simultaneously, in which the activity is measured directly [95]:

$$a_i = \frac{p_i}{p_i^o} = \frac{I_i}{I_i^o}. \tag{3.17}$$

where the partial pressures of the pure component (p_i^o) and the vapor of the component in an alloy (p_i) which are measured simultaneously using the intensity from the spectrometer. A dual-cell apparatus can be seen in Figure 3.13, and the overall schematic of a Knudsen Effusion Mass Spectrometer apparatus can be seen in Figure 3.14.

The automatic positioning of the effusion cells (all held at a constant T) allows for the measurement of several pressures *in-situ*, avoiding the sensitivity issue. The vapor from the cell (dubbed molecular beam by some) is limited by an aperture and then impacted with an electron beam to ionize it, producing this general reaction:

$$M + e^- \rightarrow M^+ + 2e^- 1 \tag{3.18}$$

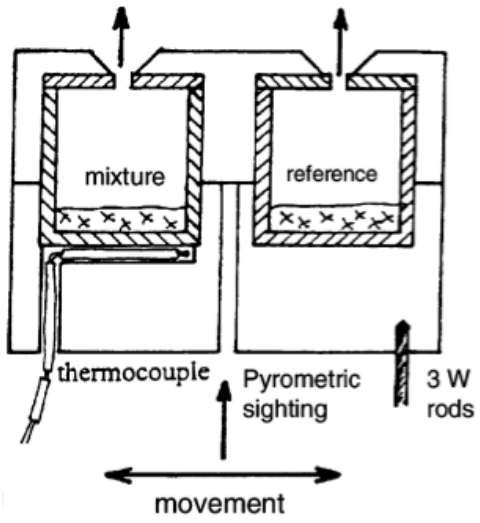

Figure 3.13 Dual Knudsen Effusion cell for direct measurement of activities from Heyrman et. al. [39].

where M is some metal and M^+ some metal ion. The ions are then accelerated with a potential and separated with the magnetic sectoring, and then counted. The temperature of the cell can be measured using thermocouples or pyrometry. By creating a blackbody cavity in the effusion cell, the emissivity is approximately unity, eliminating a lot of the uncertainty in using a non-contact pyrometer. Thermocouples require feedthroughs and can require re-calibration if they are held at high temperatures for extended periods of time. The counting of the ions is then related to ion intensities which provides the activity. Further experimental details can be seen in a review by Drowart [165].

3.5 Conclusions

From the review presented here, the following conclusions can be drawn:

- The main experimental techniques for generating thermodynamic data are calorimetry, electromotive force, and vapor pressure techniques.
- The techniques for measuring thermodynamic properties undercooled liquids are emulsification and fluxing techniques in combination with DSC, *in-situ* devitrification in DSC, levitation drop techniques, and levitation free-cool techniques.

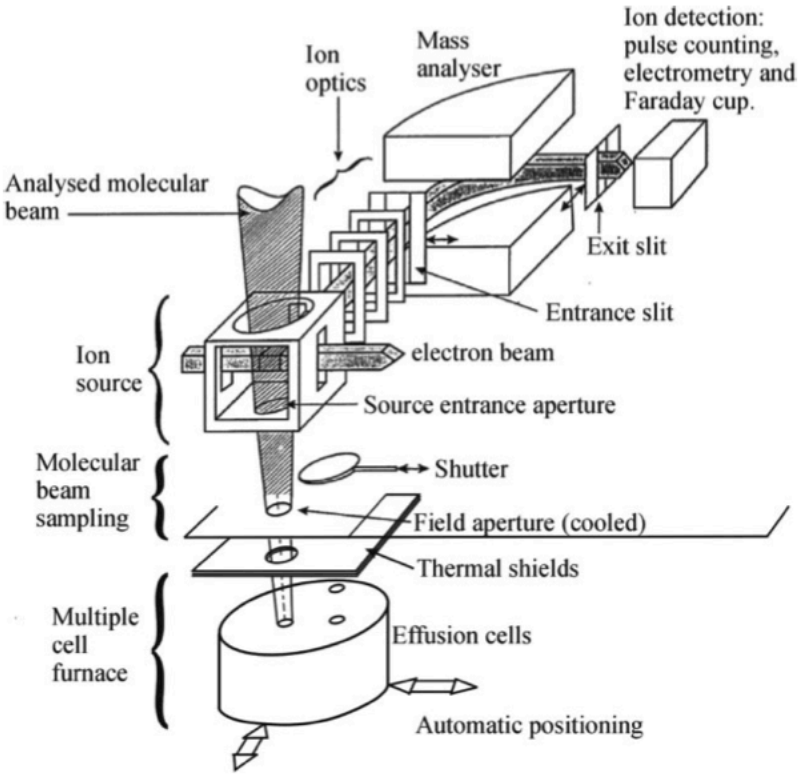

Figure 3.14 A schematic of KEMS apparatus by Heyrman et. al. [39].

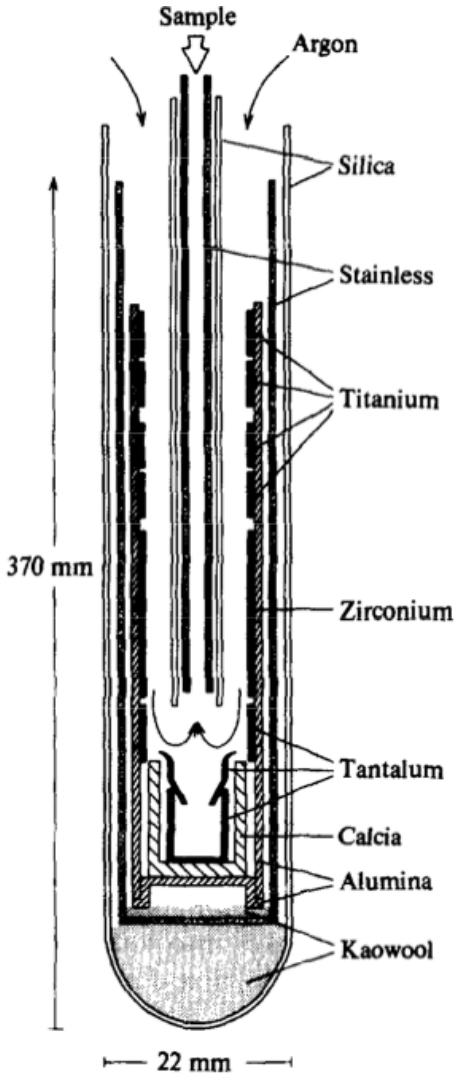

Figure 3.15 One calorimeter cell of a twin-type calorimeter, here used in a high temperature drop method [40].

CHAPTER 4. Development of Levitation Calorimetry Technique

4.1 Overview

When a metal is placed within an energized induction coil, the time-varying magnetic field generated by the coil induces eddy-currents in the object. The interaction between the induced currents and the applied magnetic field produces an electromagnetic force, known as a Lorentz force [166]. When the strength of the Lorentz force is greater than the strength of gravity, the metal levitates. The induced currents also causes resistive heating (also known as Joule heating) which can melt the metal. The principle of the drop calorimetry technique is the establishment of thermal equilibrium between the experimental sample at high temperature, and the calorimeter at room temperature, with precisely known heat capacity. The metallic liquid is introduced into the calorimeter, and the temperature response of the calorimeter evaluated to determine the enthalpy of metallic melt.

4.2 History

The concept of electromagnetic levitation was proposed and patented by Muck in 1923 [167], however it wasn't until 30 years later that some engineers at the Westinghouse Research Laboratory constructed and proved the concept [168]. One reason stated in literature for the extended time before Westinghouse further developed the technique was the lack of both a profitable application and the hardware necessary to generate the required electromagnetic field strengths [169]. The motivations behind the construction of the Westinghouse levitator was to reduce contamination from crucibles when processing Titanium, Zirconium, and Tantalum [168, 170]. Several researchers attempted to find industrial applications, and there was even an article in LIFE magazine (seen below in figure 4.1) that spoke of purifying metals for jets

and nuclear power plants by scaling up the Westinghouse design [171] however such industrial applications were never realized due to problems related to relatively large sample sizes (30g) [168]. It can be seen in the LIFE magazine article that one problem related to large samples is that "dripping" of the sample is controlled by the surface tension of the sample. There have been attempts to levitate toroidal samples to minimize dripping for industrial applications [172]. Other applications that were explored included using vacuum to vaporize metals, in which uranium was vaporized and deposited in a controlled manner [173].

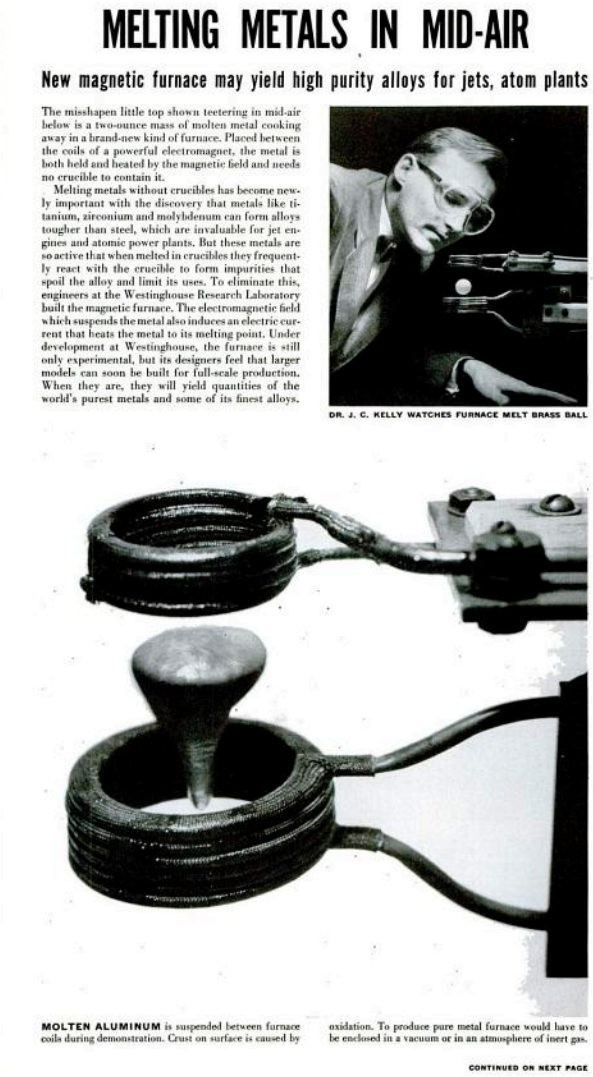

MELTING METALS IN MID-AIR

New magnetic furnace may yield high purity alloys for jets, atom plants

The misshapen little top shown teetering in mid-air below is a two-ounce mass of molten metal cooking away in a brand-new kind of furnace. Placed between the coils of a powerful electromagnet, the metal is both held and heated by the magnetic field and needs no crucible to contain it.

Melting metals without crucibles has become newly important with the discovery that metals like titanium, zirconium and molybdenum can form alloys tougher than steel, which are invaluable for jet engines and atomic power plants. But these metals are so active that when melted in crucibles they frequently react with the crucible to form impurities that spoil the alloy and limit its uses. To eliminate this, engineers at the Westinghouse Research Laboratory built the magnetic furnace. The electromagnetic field which suspends the metal also induces an electric current that heats the metal to its melting point. Under development at Westinghouse, the furnace is still only experimental, but its designers feel that larger models can soon be built for full-scale production. When they are, they will yield quantities of the world's purest metals and some of its finest alloys.

DR. J. C. KELLY WATCHES FURNACE MELT BRASS BALL

MOLTEN ALUMINUM is suspended between furnace coils during demonstration. Crust on surface is caused by oxidation. To produce pure metal furnace would have to be enclosed in a vacuum or in an atmosphere of inert gas.

CONTINUED ON NEXT PAGE

Figure 4.1 Excerpt from the June 16, 1952 issue of LIFE magazine showing EML.

Much of the work after this period was the investigation of practical aspects of levitation

such as maintaining levitation until melting, reducing dripping of the liquid metal during levitation, and determining coil designs by build and test methods. However, in 1965, Fromm examined the effect of specific levitation parameters [174], which determined and quantified the result of varying the applied current and frequency, in addition to sample size and electrical conductivity.

Beginning in the 1970s, levitation drop calorimetry was developed to measure the properties of high temperature liquids that would react with traditional containers (such as Ti, Mo [175], Pt, Nb, Ta [176], and many of the rare earth elements [121, 177, 178, 179]). Later, chamber designs for levitation calorimetry began to include vacuum systems which extended the limited undercooling levels achieved previously [180, 33, 28, 181, 182, 90, 183, 184]. Indeed, reduction of heterogeneous nucleation sites by containerless processing enables access to hundreds of degrees of undercooling [185, 35].

Levitation drop calorimetry requires several modifications to an electromagnetic levitation apparatus for successful use of the technique. The development of a levitation drop calorimeter is presented as though a functional electromagnetic levitation chamber (RF generator, vacuum sealed chamber) already exists. Primarily the modifications consist of allowing for stable introduction of cooling gas (without introducing impurities or electrical breakdown) and incorporating a calorimeter to measure the heat content of samples.

4.3 Refinement of EML Apparatus for Levitation Calorimetry

4.3.1 Optimization of Levitation Coils

A fellow group member, Zach Royer, combined a genetic algorithm and an analytical model from Fromm, et al. ([174] to optimize levitation parameters for lower temperatures to better reach the undercooled liquid state. The algorithm determines the power input to the sample (heat flux) and lifting force from a given coil design, then varies one loop to determine if it would be beneficial. This can then be explored thousands of times efficiently with a computer to sample a large variety of coil designs. The resulting experimental coil geometry used for most of the experimental work can be seen in Figure 4.2. His work can be viewed in his thesis

[48] or in a more concise publication [41].

z-Position (m)	Radius (m)
0.000	0.012
-0.0045	0.012
0.004	0.012
0.004	0.016
0.013	0.012
0.015	0.016

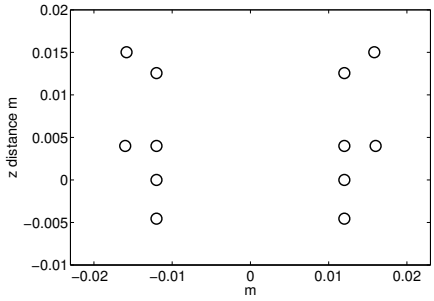

Figure 4.2 Experimental coil geometry used from [41]

The optimization resulted in a decrease of 70 degrees from a commonly used seed coil. Later, it became necessary to increase the levitation power. It was found that the existing design could be made smaller (reduced radius) which increased levitation power without an excessive increase in temperature.

4.3.2 Cooling Gas Introduction

The resistive heating inherent to the levitation process is an obstacle to achieving sample temperatures below their melting point. The high power RF sources (5 kW in our case, research levitators usually are 5-25 kW [186]) provide ample opportunity to cause electrical breakdown in a low pressure environment. Practically this means that when introducing cooling gas to an energized vacuum, the cooling gas can form a plasma and create a conduction path between the electrical leads, causing a short circuit and interrupting levitation. This is most likely to occur when the pressure is in a transient state that is not high vacuum, or nearing a full atmosphere (approximately 10 mbar Helium, 4kW power in the experimental chamber), the exact pressure is dependent on the cooling gas used, the power, and lead gap distance, however. The mechanisms of electrical breakdown in vacuum and gas atmospheres have been known for some time [187], and the voltage breakdown of a gas as a function of voltage, pressure, and gap spacing can be calculated by Paschen's law [188]:

$$V_b = \frac{apd}{ln(pd) + b} \tag{4.1}$$

where V_b is the breakdown voltage in volts, p is the pressure (bar), d is the electrode gap distance in meters. a and b are constants based on the composition of a gas. By differentiating with respect to pd, and assuming a constant gap distance, breakdown voltage can be calculated as a function of pressure. These are usually referred to as Paschen curves. These have been measured [187] for several gases and can be seen in Figure 4.3.

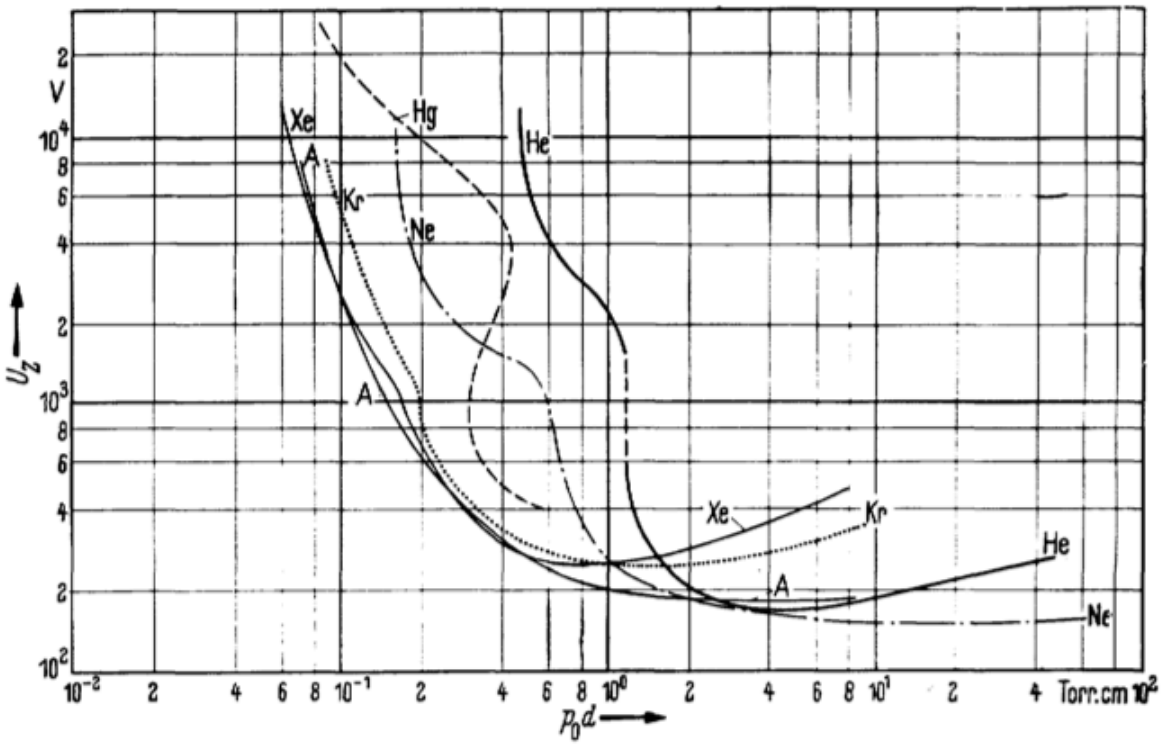

Figure 4.3 Paschen curves measured for various gases assuming a gap distance of d =1cm

It can be seen in figure 4.3 that the minimum voltage for Helium for a gap spacing of 1cm to be approximately 200 V. These gap distances and applied powers are commonly used in EML. Electrical insulation is therefore a requirement for successful use of cooling gas. It was found that the most intense (and therefore most likely) arcing occurred at the high power feedthrough between the high power leads where the gap distance is small, and therefore the most critical area to insulate properly. The solution implemented was to use pure silica, which has a very high electrical resistance and epoxy it in place between the power leads using a high vacuum epoxy which greatly increases the effective gap distance. For future work, the electrical leads

and coil will be wrapped with silica-based fiberglass, which has sufficient electrical resistance and completely encompasses the leads which should more be more effective.

After insulating the power feedthrough, Kapton CR (corona-resistant, where corona is ionized gas that has not yet formed a plasma) film was wrapped along the leads and possessed a suitable resistance to reduce (but not eliminate) ionization. It is possible for discharges to occur that would not interrupt levitation, and the use of film reduced their occurrence.

The next point of electrical interruption was found to be between the coil loops. The solution to this was to use heat shrink on the copper tubing prior to winding the coil. The heat shrink reduced the possibility for the tubing to come in contact with each other and short. Eventually after a period of several months it was found that the heat shrink tubing would wear (potentially from corona formation, the mechanism was not determined). This requires either spot-correction with an insulating material or replacement of the coil.

It is also worth considering the efficiency of the levitation coil. For the study of Al-RE (discussed later) a relatively inefficient coil was used that resulted in lower temperature levitation but required more care when dealing with insulation. Alternatively when using an approximately 50% more efficient coil, electrical concerns were minimized when 50% lower power could be used for the same materials. It has been reported for researchers using 15 kW power supplies that vacuum operation was not possible at all due to the formation of corona, although there was no reports of use of insulation [176, 121].

Cooling gases have been used in many cases in EML, although if the target is undercooling the most sensible gas to use is Helium. When the experimental goal is higher temperature levitations, argon can be used to increase the chamber pressure and reduce vaporization without the potent temperature reduction of Helium. Gas purity and vacuum purity go somewhat hand-in-hand, and when considering gas purity (and therefore price) it is prudent to consider the overall purity of the system. Considering a 99.999% pure gas, impurities are 0.001% or one part per thousand which corresponds to the low pressure edge of medium vacuum (1 mbar). 99.9995% (UHP gas) therefore nets double the purity, or .5 mbar which is on the high pressure edge of high vacuum. For experiments in which the chamber is to be backfilled with Argon, for instance, researchers should note that extended vacuum pumping times to achieve higher

purity is not worthwhile. For situations in which the sample is going to be melted in vacuum, and then cooling gas is introduced, it can still be beneficial to improve the vacuum level beyond that of the purity of the gas.

4.3.3 Motion Translation and Vaporization Shield

Over the years there have been several strategies for initially holding the metallic sample prior to levitation. There has been use of thin cotton string that eventually burns off [176], but the more common use of an actuator in conjunction with a small crucible. Depending on the desired measurement, it may be sufficient to only have a linear actuator in which the crucible can move within the axis of the levitation coil. For drop calorimetry, it is necessary to rotate the crucible out of the way of the coil to allow the sample to fall into the calorimeter. Rotational actuators therefore must have the linear travel in order to move the crucible out of the coil and at least enough rotation to move it out of the way. In our studies it was also helpful to mount a vaporization shield approximately 45 degrees rotated from the crucible. Once the sample is levitated, the crucible is moved out of the coil and vaporization shield rotated into the path between the sample and the pyrometer. This allows for protection of the optical path in case of vaporization prior to the introduction of cooling gas, which eliminates concerns of vaporization changing the apparent temperature measurement between experiments.

The modified EML apparatus can be seen in Figure 4.4

4.4 Isoperibolic Calorimeter Development

The principle of the drop calorimetry technique is the establishment of thermal equilibrium between the experimental sample at high temperature, and the calorimeter at room temperature, with precisely known heat capacity. Isoperibolic describes calorimeters for which a constant surrounding temperature is maintained [101]. In contrast to adiabatic calorimeters, heat is lost to the surroundings during the sample-calorimeter heat transfer period, which requires temperature correction in order to accurately determine the enthalpy of the sample. In the isoperibolic design employed here the initial calorimeter temperature is the same temperature as the surroundings prior to the introduction of heat from the sample, at which point the

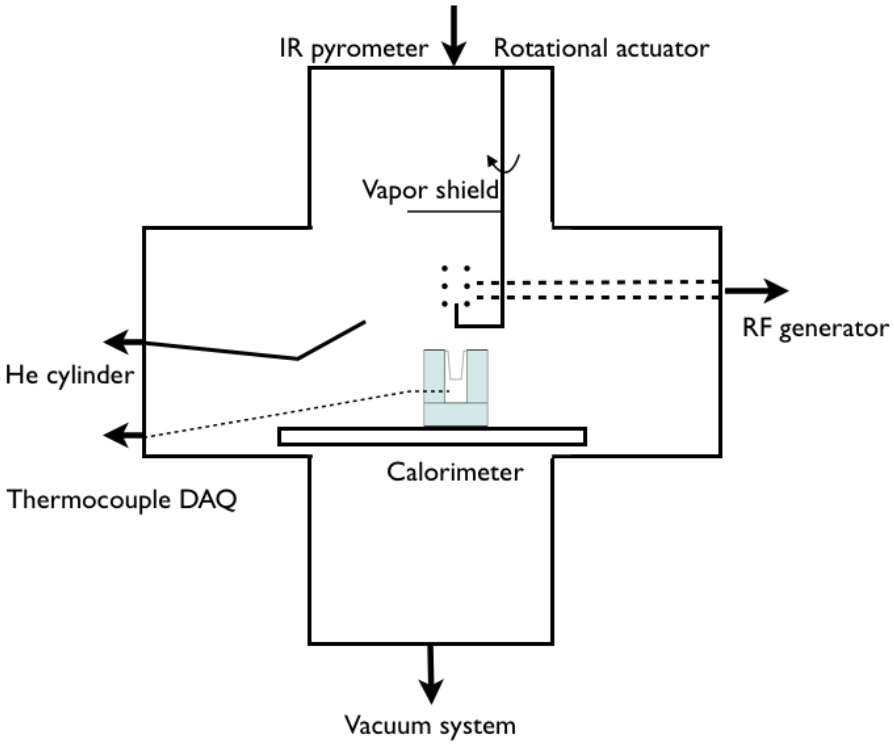

Figure 4.4 Description of levitation drop calorimeter apparatus.

calorimeter temperature rises (sample-calorimeter heat transfer period) and eventually returns to the initial temperature (calorimeter-surroundings heat transfer period).

Due to the use of vacuum and high temperature samples, aneroid (metal block) calorimeters must be used. The most suitable block material was determined to be pure copper due to its high thermal conductivity and reasonable cost. Several block shapes were evaluated throughout the process of development and will be described below. All of the calorimeter blocks were made from sections of a 1" copper rod as the intention was to have the calorimeter block be relatively small. A smaller calorimeter block will have a greater signal to noise ratio when measuring a change in temperature of the calorimeter block as well as a faster heat transfer period.

Compared to the ∼2.5kg aluminum calorimeters of Bonnell [176] or the ∼6.4 kg copper calorimeter of Schaefers et. al. [28], the main heat transfer period is considerably shorter. The heat transfer period duration reported by Bonnell is on average 1000 seconds, and the average heat transfer period duration reported by Schaefers is 780 seconds. The heat transfer period for the final calorimeter presented here is approximately 40 seconds. The natural result is a shorter period for which heat can be lost, reducing the overall temperature correction and requirement for strict environmental control. For comparison, the reported temperature corrections by Bonnell are on average 1-2°C [176], in this work the overall temperature correction is .1-.5°C.

The calorimeter is thermally connected to the stainless steel chamber via a finite heat conduction path through the insulation. In this way, the initial and final calorimeter temperatures vary with each experiment but are approximately constant. The sample-calorimeter heat transfer period is on average 40 seconds, and the calorimeter-surroundings heat transfer period on average is two hours. The final calorimeter temperature after the period of two hours is on average within 3% of the initial temperature. As described previously, the small-size calorimeter was designed to minimize the sensitivity to overall temperature correction, and it is assumed the minor fluctuations in the final calorimeter temperature contribute to random error in the temperature correction. As will be demonstrated, the overall sensitivity of the technique is within the expected accuracy, ±1-3 % error, while having considerable advantages of size and construction simplicity making the technique suitable for implementation in existing EML systems designed for other purposes.

In the development of the calorimeter, several block geometries and thermocouple configurations were tested.The first calorimeter was an approximately 100g solid copper cylinder with a hole drilled in the block with an ordinary drill bit, with additional holes drilled in the side for thermocouples. It was used in proof of concept measurements, however it was quickly replaced due to the inability to remove samples after experiments. The second calorimeter was a two-piece construction to separate the bottom and remove the sample. This was used in vacuum, however the calibration was not suitable for examining materials of vastly different densities because it was found that less dense materials would contact the upper calorimeter block and change the temperature response. Thus it was determined that a one-piece calorimeter block would be best. It was also at this point that open-cell polyimide foam was used as an insulating material. Open cell foams are suitable for use in vacuum systems and the use of foam prevents convection over most of the surface area of the calorimeter block (with the exception being the inside surface area). The third calorimeter was designed with an extreme taper to simplify sample removal after experiments, which was suitable for evaluating pure copper however when attempting to test aluminum there was excessive splashing, however in spite of the splashing the calorimeter was able to successfully measure the enthalpy of Cu and Al within reasonable error when calibrated for only one material, proving that the one-piece calorimeter block was essential to the accurate measurement of enthalpy. The second and third calorimeters can be seen in Figure 4.5.

The final calorimeter utilized a flat bottom hole to minimize splashing, and a 4° taper throughout to ensure sample removal. In Figure 4.6 the specifications and an image can be seen. The deep hole also minimizes the angle for which a sample could potentially splash out.

4.4.1 Calorimeter Temperature Measurement

In the past (and relatively recent years), there have been use of quartz thermometers [175, 28] however quartz thermometers are no longer being produced. There also have been arguments for the construction of thermistor circuits due to their fast time constant and high sensitivity [189].Thermocouples were chosen due to their ease of use and commercial availability of passthrough and data acquisition hardware. It was initially determined that the method

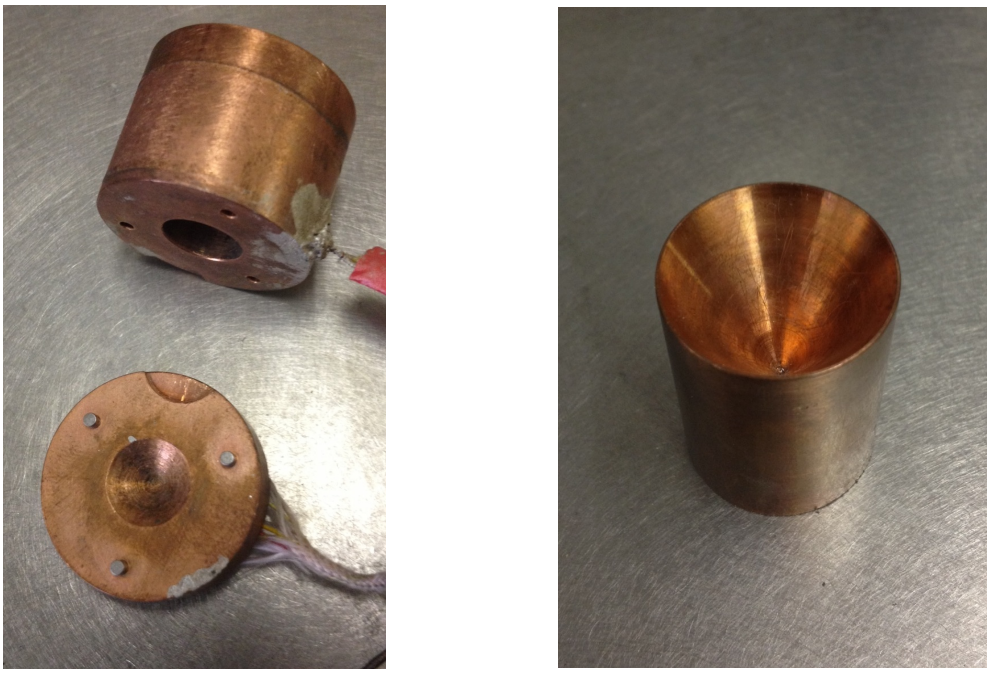

Figure 4.5 Incremental calorimeter designs. Left, two part calorimeter with separate thermocouples. Right, conical calorimeter with thermocouple on bottom.

should be evaluated with thermocouples, and if greater sensitivity were later required other avenues would be pursued.

The thermocouples were constructed by welding 0.005 inch diameter chromel and alumel wires into a Type-K thermocouple using a thermocouple wire welder. Thermocouples were fixed in place by drilling a shallow 5/64" hole and held in place with conductomet silver epoxy. The placement of thermocouples was evaluated and in general the best position was considerable distance from the heat introduction location. This is primarily due to the possibility of "heat damming" [93] which is a temporary spike related to the transient conduction of heat before the entire block is the same temperature. This can be seen in Figure 4.7.

Type-K thermocouple feedthroughs were used to pass the thermocouple signals to a National Instruments USB-9211 data acquisition system. LabView Signal Express software is used to record the temperature of the calorimeter block at a rate of 3 Hz and accuracy of ± 0.02 K.

Isoperibolic describes calorimeters for which a constant surrounding temperature is maintained [101]. In contrast to adiabatic calorimeters, heat is lost to the surroundings during the sample-calorimeter heat transfer period, which requires temperature correction in order

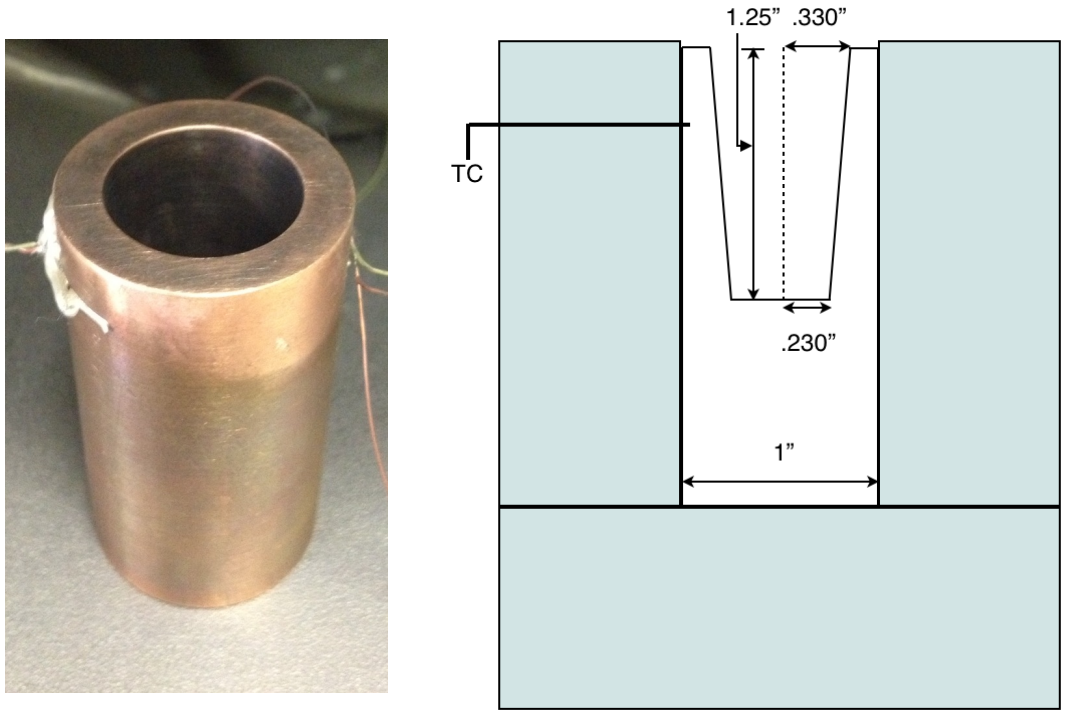

Figure 4.6 Final calorimeter design featuring a flat bottom hole to minimize splashing and tapered sides for sample removal.

to accurately determine the enthalpy of the sample. In the isoperibolic design employed here the initial calorimeter temperature is the same temperature as the surroundings prior to the introduction of heat from the sample, at which point the calorimeter temperature rises (sample-calorimeter heat transfer period) and eventually returns to the initial temperature (calorimeter-surroundings heat transfer period). The temperature response of the calorimeter from a 880.2mg copper sample at 1426.4 K can be seen in Figure 4.8. The calorimeter presented here is designed to be compact to minimize the duration of the sample-calorimeter heat transfer period, as well as the drop distance to reduce the overall sensitivity to temperature corrections for both the calorimeter as well as radiative and convective losses during the drop period.

The method for determining the true temperature was presented by Bonnell [176] in which a newtonian cooling fit (where dT/dt is proportional to the temperature difference of the object and its surroundings) is applied to the cooling portion of the temperature response curve, which is then used to determine the time-lag free temperature rise of the calorimeter. In the work

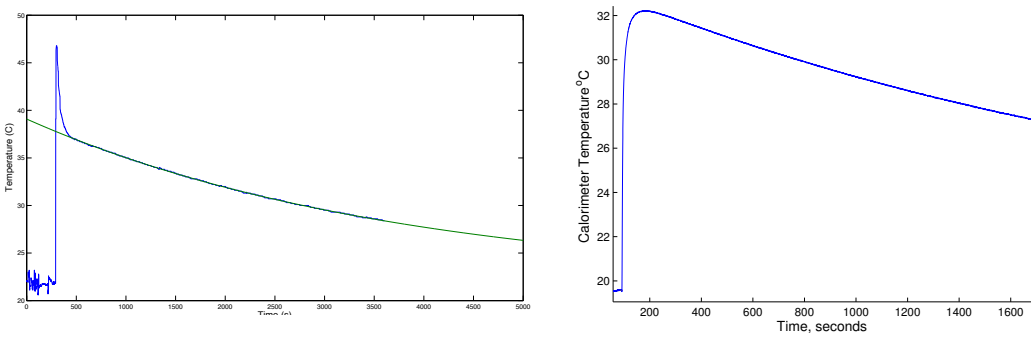

Figure 4.7 Transient heat conditions can render the peak temperature unknowable, green line represents newtonian cooling fit, blue line experimental measurement. On left, improper thermocouple placement results in temperature spike.

of Bonnell [176], the calorimeter jacket temperature is fixed at a temperature which is greater than the calorimeter temperature throughout the experiment. The calorimeter temperature then constantly drifts towards the jacket temperature, and the corrected temperature rise is calculated at the mid-point of heat transfer. In this work, the initial and final calorimeter temperatures are assumed to be constant, thus the temperature correction is calculated at the time in which the sample was introduced. T_δ is defined as the resulting temperature from the heat input, $T_i + \Delta T$.

4.4.2 Non-contact Sample Temperature Measurement

Levitated sample temperatures are measured using a non-contact infrared pyrometer, in which the basis of temperature measurement is from Planck's law, which describes the radiation emitted by a blackbody at a given temperature at thermal equilibrium. Levitated samples are considered greybodies, in which emissivities are used to relate the sample to blackbody conditions.

4.4.2.1 One-color pyrometry and multiple-color pyrometry

One-color pyrometry was chosen in this application, however the merits of multiple-color pyrometry will be discussed. Multi-color pyrometry has been described as one of the most commonly misunderstood approaches to solving the emissivity problem related to levitated

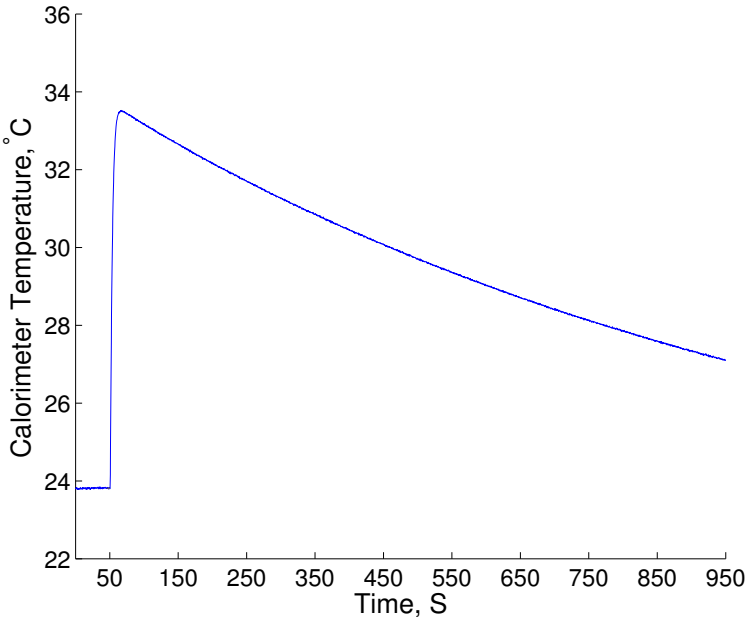

Figure 4.8 Temperature response of the calorimeter block from a 880.2mg copper sample at 1426.4 K

samples [147]. Implicit in the assumption of multi-color pyrometry is that the ratio of the emissivity at two temperatures does not vary. If we consider pyrometry, with two radiated intensities I_1 and I_2, at wavelengths γ_1 and γ_2 respectively, where the intensity is described as,

$$I(\gamma_1, T_a) = C\gamma \exp(-\frac{C_2}{\gamma_1 T_b})\epsilon_1 \tag{4.2}$$

and

$$I(\gamma_2, T_a) = C\gamma \exp(-\frac{C_2}{\gamma_2 T_b})\epsilon_2 \tag{4.3}$$

where C_2 is the second radiation constant that has the value 14.3877×10^6 nm K [190], T_b is the black-body temperature, and ϵ the emissivity to relate the observed temperature, T_a, to the blackbody temperature T_b. The assumption of two-color pyrometers is the ratio of the above equations, such that $\frac{\epsilon_1}{\epsilon_2}$ is implicit in the measurement,

$$\ln(\frac{I_1\gamma_1}{I_2\gamma_2}) = (\frac{C_2}{T_b})(\frac{1}{\gamma_2} - \frac{1}{\gamma_1}). \tag{4.4}$$

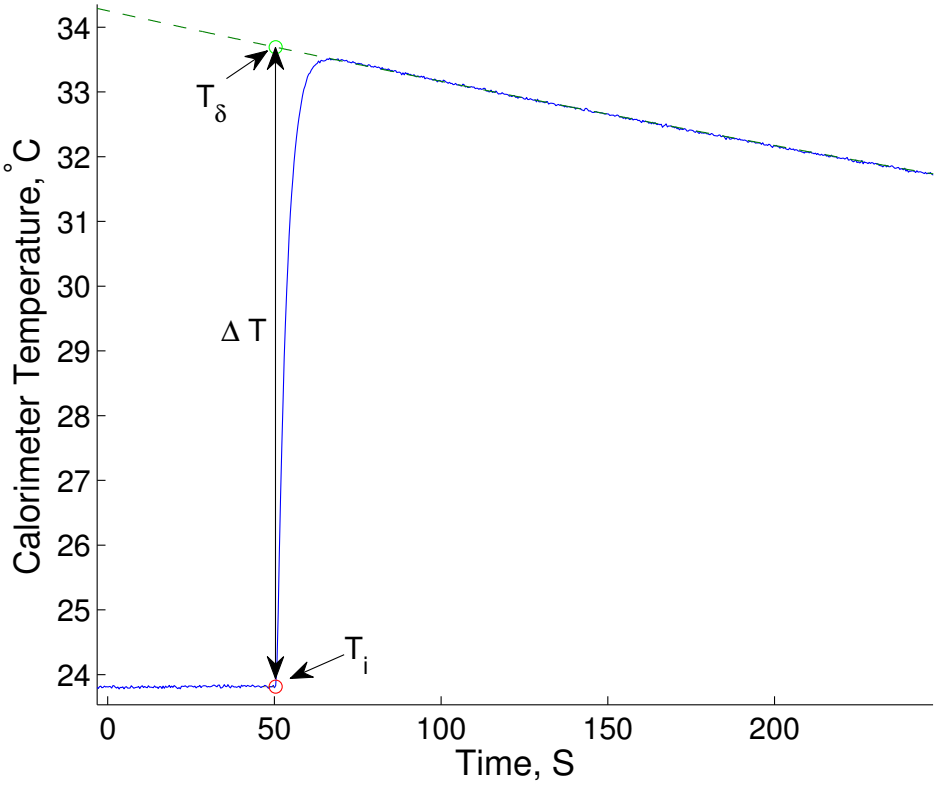

Figure 4.9 Corrected temperature rise of the calorimeter block from a 880.2mg copper sample at 1426.4 K

The validity of this assumption has been analyzed by Coates [191], in which the conclusion is that the best usage of multi-color wavelengths is as multiple-single color pyrometers, where the emissivity must be calibrated.

The pyrometer used is a Pyrometer Instrument Company Pyrofiber II, which measures radiated intensities at 1.550 μm with focusing optics that produce a 1.9 mm spot size at a working distance of 14". The operating mode used produces readings at a rate of 8 Hz. The emissivities of the melts were determined using an equilibrium thermal signal, such as a melting plateau, to measure the apparent temperature at which point the emissivity may be corrected such that the known thermal signal is represented in the temperature measurement. Using

Wien's approximation to Planck's law the emissivity can be determined by [182, 28]

$$\epsilon_\gamma(T_m) = \exp\left[\frac{C_2}{\gamma}(\frac{1}{T_m} - \frac{1}{T_a})\right], \tag{4.5}$$

where T_m is the published or experimentally determined temperature of the thermal signal, T_a is the measured apparent temperature of the thermal signal from the pyrometer, γ is the wavelength measured by the pyrometer, and C_2 is the second radiation constant that has the value 14.3877×10^6 nm K [190]. The temperature measurement is therefore dependent on the assumption that the emissivity of the liquid is constant. This assumption has been used by many other researchers using this technique [192, 175, 176, 121, 90, 183].

Another factor to consider when determining the emissivity of the melt is removal of an oxide layer if present. The physical mechanism for oxide removal has not been fully established. A consistent mass loss can be observed for aluminum samples of nearly the same size and it has been presented that the oxide layer is removed along with a vaporization of a small amount of aluminum [193]. Limited publications in this area seem to confirm that higher temperatures can remove oxide layers [194]. The oxide layer and underlying liquid can be identified by the stark difference in brightness due to an approximately 50% difference in emissivity [180]. The oxide removal process can be seen below in Figure 4.10. It has been determined that higher vacuum levels allow for more rapid vaporization of the oxide layer, but cooling gas should be introduced quickly to reduce further vaporization than is necessary. Once the temperature measurement is determined to be stable, the RF power supply is turned off and the sample drops into the calorimeter.

4.5 Enthalpy Increment Calculation

The enthalpy increment of a sample at temperature, T, can be calculated with respect to the increased calorimeter temperature, T_δ, in the following manner,

$$H(T) - H(T_\delta) = C_p^{cal}\Delta T\frac{M}{m} + Q_{lost}\frac{M}{m}, \tag{4.6}$$

in which C_p^{cal} is the heat capacity of the calorimeter, ΔT is the corrected temperature rise of the calorimeter, M is the molar mass, m is the sample mass, and Q_{lost} represents the heat lost

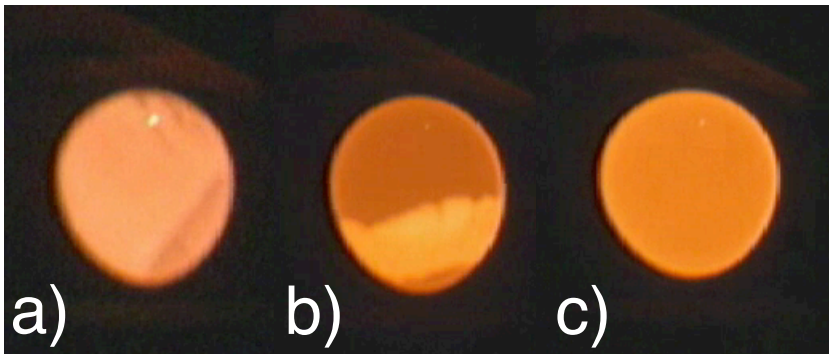

Figure 4.10 Removal of oxide layer of pure Al in vacuum conditions: a) oxidized b) partially removed c) 99% removed.

during the drop from radiation and convection ($Q_{lost} = Q_{rad.} + Q_{conv.}$). It is generally more useful to have measured enthalpy increments be in reference to the same final temperature, usually 298 K. This requires the addition of the remaining enthalpy from T_δ to 298 K, which requires experimental determination of the heat capacity or estimation from thermodynamic data. The heat capacity is generally assumed to be constant over the small range (6-10 K) [28, 90] of T_δ to 298 K. In this work, the heat capacity for pure materials is obtained from the Scientific Group Thermodata Europe (SGTE) database [42], and if no reference is available the heat capacity is measured in reference to a sapphire standard with application of the isothermal step method [129, 130] using a Perkin-Elmer Pyris 1 DSC. The room temperature heat capacity of the sample is used in the following manner,

$$H(T_\delta) - H(298) = C_p^{298}(T_\delta - 298), \tag{4.7}$$

which is added to Equation 4.6 to calculate the enthalpy increment for a fixed reference temperature, $H(T) - H(298)$, which has been commonly used [121, 169, 90, 184],

$$H(T) - H(298.15) = C_b \Delta T_b \frac{M}{m} + Q_{lost}\frac{M}{m} + [H(T_\delta) - H(298)]. \tag{4.8}$$

A schematic of the enthalpy increment measurement can be seen in Figure 4.11.

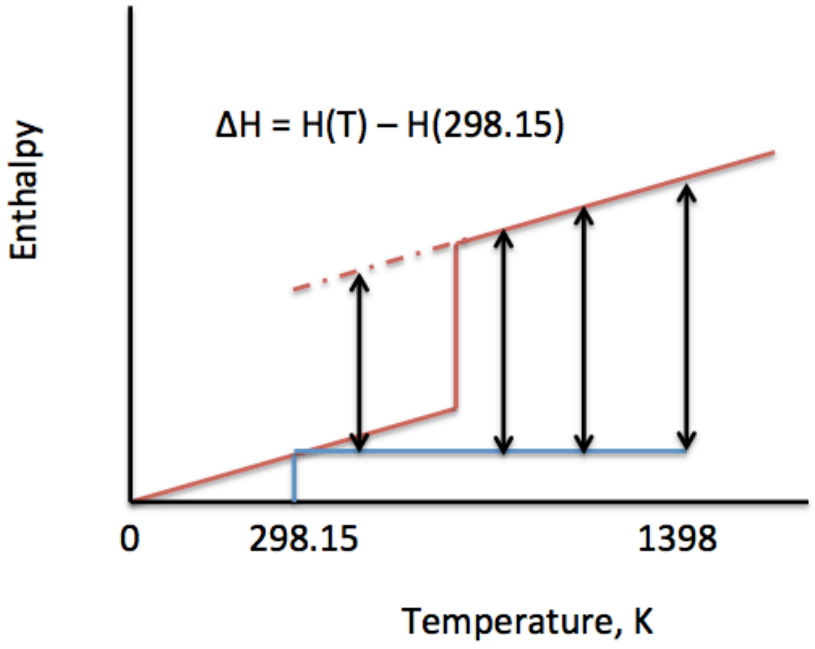

Figure 4.11 Schematic of enthalpy as a function of temperature. Each arrow represents an enthalpy increment measurement. Dashed line represents the undercooled liquid.

4.5.1 Heat Loss During Drop Period

The total Q_{lost} during the sample drop period can be calculated individually as losses from radiation and convection, ie

$$Q_{lost} = Q_{rad.} + Q_{conv.}. \tag{4.9}$$

$Q_{rad.}$, the heat lost due to radiation, can be calculated by the integration of Stefan and Boltzmann's law for the sample drop period,

$$Q_{rad} = \int_0^{t_d} \epsilon_t \sigma A (T_s^4 - T_r^4)\ \mathrm{d}t \tag{4.10}$$

which results in [28],

$$Q_{rad} = \epsilon_t \sigma A (T_s^4 - T_r^4) t_d \tag{4.11}$$

where ϵ_t is the total hemispherical emissivity, σ is the Stefan-Boltzmann constant of value $5.67{\times}10^{-8}$ J S^{-1} m^{-2} K^{-4}, A is the surface area of the sample, t_d is the time of the drop period, T_s is the temperature of the sample, and T_r is the temperature of the surroundings, room temperature in this calculation. The total hemispherical emissivity is generally not known,

others have presented estimating the value from the determined spectral emissivity [176]. The surface area can be estimated from the assumption of a spherical sample, where the volume can be calculated from the the liquid density to determine the surface area ($A = 4\pi r^2$). In some cases the liquid density is reported, otherwise it has been presented that estimating the liquid density to be 10% less than the room temperature crystalline state is reasonably consistent with reported data [186]. The drop time, t_d can be determined by assuming free fall conditions,

$$t_d = \left(\frac{2h}{g}\right)^{1/2} \tag{4.12}$$

where h is the drop height, and g the standard acceleration due to gravity, 9.806 m/s^2.

The magnitude of the radiative losses during the drop period is small for moderate temperatures, noting the T^4 dependence. Considering pure aluminum, m = 509.4 mg, A = 8.02 x 10^{-4} m^2 (from liquid density of 2.375 g/cm^3 [195]), T_s = 1389 K, T_r = 298 K, t_d = 0.178 seconds, ϵ_t = 0.084 (value estimated as 20% more than the spectral emissivity, from [121], the enthalpy lost was 133.9 J/mol which represents 0.3% of the measured enthalpy increment.

Convective heat losses are calculated using the method presented by Stretz [121], where the primary assumptions are a stationary spherical sample where the gas flow velocity is approximated as the free-fall sample drop velocity. The heat losses due to convection can be written as

$$Q_{conv.} = A(T_s - T_g) \int_0^{t_d} \alpha \, \mathrm{d}t, \tag{4.13}$$

where t_d is the sample drop time, A the surface area, T_s the sample temperature, T_g the gas temperature (usually assumed 298 K),and α the heat transfer coefficient,

$$\alpha = \frac{\lambda}{D}\left[2 + 0.6(\mathrm{Re})_f^{1/2}(\mathrm{Pr})_f^{1/3}\right], \tag{4.14}$$

where λ is the gas thermal conductivity, D the sample diameter, Re the Reynolds number, and Pr the Prandtl number. The Reynolds and Prandtl number are calculated using the gas film temperature ($T_f = \frac{(T_s - T_g)}{2}$). The Reynolds number and Prandtl number are defined as

$$\mathrm{Re}_f = \left(\frac{D\rho_g v_{gas}}{\mu_f}\right) \tag{4.15}$$

and

$$\mathrm{Pr}_f = \left(\frac{C_p^{gas}\mu_f}{\lambda}\right) \tag{4.16}$$

where v_{gas} is the gas velocity, ρ_g the gas density, μ_f the dynamic viscosity at T_f, C_p^{gas} the gas heat capacity. As an approximation for the gas velocity, the sample velocity as a function of drop time is substituted, where the modified Reynolds number takes the following form,

$$\mathrm{Re}'_f = \left(\frac{D\rho_g g t_d}{\mu_f}\right). \tag{4.17}$$

When the modified Reynolds number is combined into Equation 4.14, and Equation 4.13 evaluated, the final form can be written as

$$Q_{conv.} = A(T_s - T_g)\frac{\lambda}{D}\left[2t_d + 0.4(t_d)^{3/2}\left(\mathrm{Re}'_f\right)^{1/2}\left(\mathrm{Pr}_f\right)^{1/3}\right]. \tag{4.18}$$

Considering again pure aluminum, m = 509.4 mg, A = 8.02 x 10^{-4} m^2, T_s = 1389 K, T_g = 298 K, the total enthalpy lost is 265 J/mol, which is 0.61% of the total heat content. Convective losses are linearly temperature dependent $(T_s - T_g)$ compared to the fourth order dependence for radiative losses $(T_s^4 - T_r^4)$, meaning the overall sensitivity to temperature dependent changes is decreased. Due to a hardware limitation, gas pressure measurements are limited to the range 1x10^{-6} to 30 mbar, whereas experimental conditions can exceed 30 mbar for some materials. Due to this limitation, convective losses are assumed to be negligible.

Table 4.1 Summary of variables for calculation of radiative and convective losses. Some values are calculated for each sample condition.

	Description	Value	Ref.
ρ	Al liquid density	2.35 g/cm^3	[195]
r	Sample radius	calculated, assume sphere	$(\frac{\text{volume}}{\pi} \cdot 3/4)^{1/3}$
A	Surface area of sample	calculated	$A = 4\pi r^2$
t_d	Sample drop time	0.178 seconds	$t_d = \left(\frac{2h}{g}\right)^{1/2}$
ϵ_t	Total hemispherical emissivity of liquid Al	0.084	estimated [121]
σ	Stefan-Boltzmann constant	5.670×10^{-8} W/m^2K^4	[190]
T_s	Sample temperature		
T_r	Temperature of surroundings (room temp)	298 K	
T_g	Temperature of gas	298 K	
λ_f	Thermal conductivity of fluid at T_f	calculated	[196]
μ_f	Dynamic viscosity at T_f	calculated	[196]
ρ_g	Density of gas	calculated	[196]
C_p^{gas}	Heat capacity of helium	5193.1 J/ kg^{-}1 K^{-}1	[28]
T_f	Fluid temperature	calculated	$T_f = \frac{(T_s - T_g)}{2}$
MW	Molecular weight of helium	40.002602 g/mol	[197]

4.5.2 Calibration

The heat capacity of the calorimeter, C_b, is determined using 99.999% pure aluminum. Enthalpy increments are measured and calculated with Equation 4.8, and the results compared to

the value in the SGTE database [42]. The heat capacity of the calorimeter, C_b, is then adjusted to minimize the error between the measured results and the reference. The apparent spectral emissivity of unoxidized liquid aluminum at 1.550 μm, ϵ_γ, was determined to be 0.07. The results from calibration are listed in Table 4.3, and can be seen in Figure 4.12. There are many other techniques that have been used for calibration of calorimeters, including electrical calibration (joule heating) [176, 189], Peltier cooling, or other techniques such as radioactive materials, summarized by Ferro [198]. Each calibration method has advantages and disadvantages, and it was determined that calibration using a known material would be sufficient.

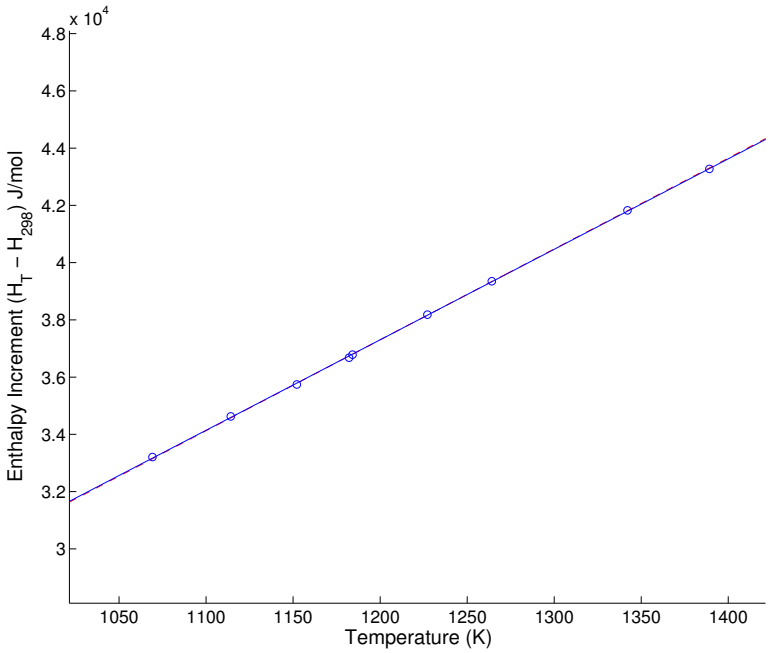

Figure 4.12 Measured enthalpy increments of pure aluminum for calibration (○), and experimental fit (solid line). Red dashed line for reference is from the SGTE database [42].

Once the calorimeter is calibrated, another material of well known enthalpy is evaluated using the levitation calorimeter to confirm the calibration value. Pure copper is well described in literature and is chosen to evaluate the calibration. The apparent spectral emissivity of liquid copper, ϵ_γ at 1.550 μm, was determined to be 0.019. The measured enthalpy increments are summarized in Figure 4.13 and Table 4.4. The determined heat capacities, C_p, for aluminum

and copper are presented in Table 4.2.

Table 4.2 Determined liquid and undercooled liquid heat capacity from linear fit of enthalpy data, and intercept for the form H(T) - H(298) = C_p·T + b, with 95% confidence intervals given.

Sample	C_p (J/mol K)	b (kJ/mol)	% Deviation from [42]
Al	31.76±0.31	-0.808±0.37	-0.03
Cu	31.59±7.06	-0.479±10.67	-0.67

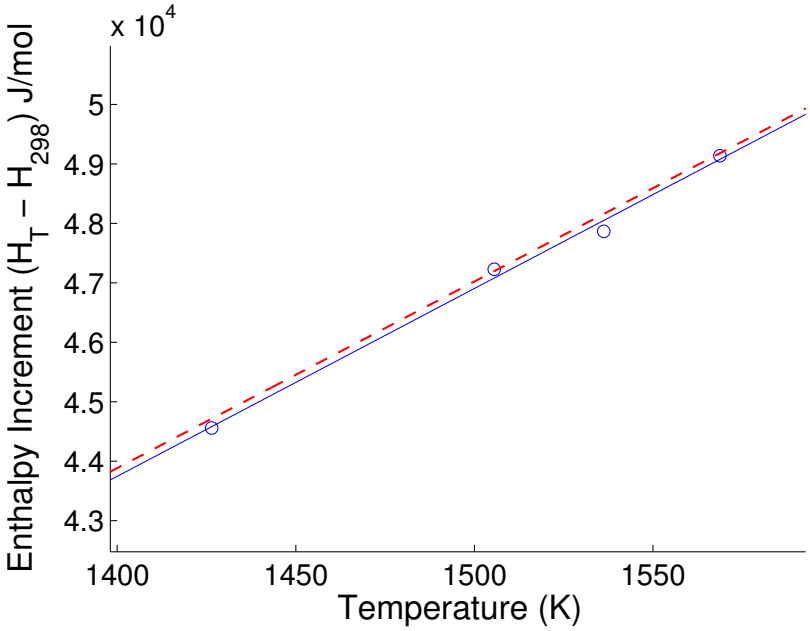

Figure 4.13 Measured enthalpy increments of pure copper (∘) and fit (solid line). Red dashed line for reference is from the SGTE database [42].

Indeed, the drop calorimetry method is successful in determining the enthalpy of liquid melts within 1%. The error observed is likely a combination of the uncertainty involved in experimental emissivity determination for copper and aluminum, which is a result of the limitation of IR pyrometry.

4.6 Conclusions

In summary, in order to achieve high accuracy enthalpy measurements the following must be considered when developing a levitation drop calorimeter:

- Cooling gas introduction requires proper electrical insulation and evacuation of the gas lines prior to use.
- The calorimeter block shape and thermocouple placement require consideration for achieving a proper temperature response without splashing or measurement of transient heat conditions.
- The non-contact sample temperature measurement requires some emissivity calibration from a known temperature signal.
- The enthalpy increment calculation requires the calorimeter be properly calibrated, and the heat lost during the fall period be calculated.

Table 4.3 Measured enthalpy increments of pure aluminum used for calorimeter calibration.

Mass (mg)	Temperature (K)	$H_T - H_{298}$ (kJ/mol)	% Deviation from [42]
509.43	1389.7	43.30	0.05
514.64	1227.5	38.20	-0.07
515.57	1264.0	39.37	-0.09
518.00	1184.5	36.81	0.01
512.75	1342.9	41.85	-0.03
516.01	1153.0	35.76	0.11
509.10	1114.7	34.65	-0.12
514.52	1072.1	33.22	0.03
487.59	1182.4	36.70	0.10

Table 4.4 Measured enthalpy increments of pure copper.

Mass (mg)	Temperature (K)	$H_T - H_{298}$ (kJ/mol)	% Deviation from [42]
878.2	1426.5	44.56	0.32
848.5	1536.3	47.87	0.60
728.3	1568.8	49.14	0.09
740.0	1505.6	47.23	-0.06

CHAPTER 5. Thermal Analysis of Aluminum-RE Binary Glass Forming Alloys

5.1 Introduction

Aluminum based materials have traditionally been investigated due to their low weights, and adequate strength for use in transport applications. Rapidly solidified binary aluminum alloys were initially investigated using splat quenching techniques with an aluminum-metalloid system, such as Al-Si by Predecki, et. al. in 1965 [199], and Al-Ge in 1972 by Ramachan. et. al. [200]. In the Al-Ge system, it was found that at high cooling rates the high temperature metastable phase could almost be completely retained. Also in 1972, Davies and Hull successfully formed a fully amorphous phase in a metal-metal sample with splat cooling of the Al-Cu system [201]. In 1977 Furrer and Warlimont further investigated a fully amorphous phase by performing *in-situ* annealing experiments and monitoring crystallization in the Al-Cr system [202]. Until 1981, the amorphous phases formed were in the extremely thin sections of foils resulting from the rapid solidification. The increased cooling rate from the melt spinning technique by Liebermann and Graham in 1976 [203] aids in the formation of larger amorphous samples. Inoue, et. al. were able to make fully amorphous samples that were large enough to perform mechanical testing (microhardness) using melt spinning in the Al-Fe-B, Al-Ni-B, and Al-Co-B systems [204]. The resulting alloys were very brittle, and had limited ductility. The first results of Al-based amorphous alloys with good ductility were achieved also by Inoue, et. al. in 1987 [205]. In 1988, a lot of progress was made with ductile Al-based amorphous alloys by Inoue et. al [206, 207, 208, 209, 210], as well as He et. al. [211]. The results were high strength (1000 MPa fracture strength) and a strength to weight ratio that exceeded high strength aluminum alloys [206]. In 1991, Kim et. al. discovered fcc-Al nanocrystals dispersed

in an amorphous matrix, providing another great leap in tensile strength to 1300 MPa [212]. It was presented that the great increase in strength was a result of the homogenous dispersion of the fcc-al crystallites, which are free of defects and smaller than shear defects, which blocks the shear mechanism greatly increasing strength.

Initially the Al-RE (RE = rare earth) binary alloys were investigated because it was thought they would be good for dispersion strengthening for high temperature applications due to several reasons that can be explained by the phase diagram in Figure 5.1.

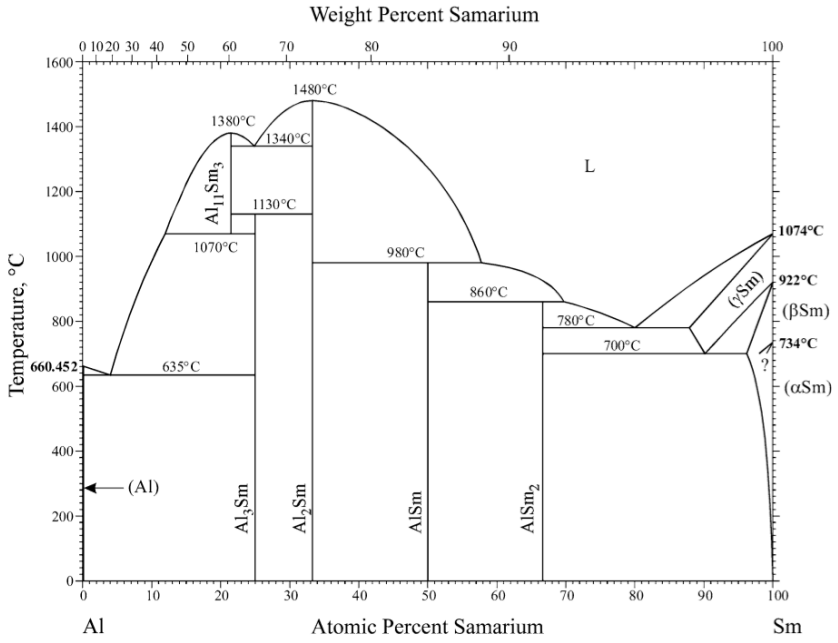

Figure 5.1 Al-Sm phase diagram from Okamoto [43].

It can be seen that there exists several properties for a high temperature dispersion strengthened alloy [213]:

- a high melting point intermetallic compound ($Al_{11}Sm_3$)
- high liquid solubility
- low solid solubility in Al
- the solid state diffusion of rare earths in Al is slow [214]

Inoue et. al then investigated the rapid quenching of Al-RE binary systems with melt spinning, determining the range of glass formation for many of the binary Al-based glass formers [215]. A plot of the formation ranges, larger in scope from a later review by Inoue, can be seen in Figure 5.2. Their results attracted some attention because the determined composition range for glass formation is off-eutectic, making them an exception to the commonly used empirical rules for glass formation: the eutectic liquid by definition is stable at a lower temperature, making it easier to reach the glass transition [216]. The systems also form a high density of nanocrystals (order of 10^{23-25} m^{-1}) embedded in an amorphous matrix which also exhibit exceptional tensile strengths beyond that of an entirely amorphous sample [217, 44, 218].

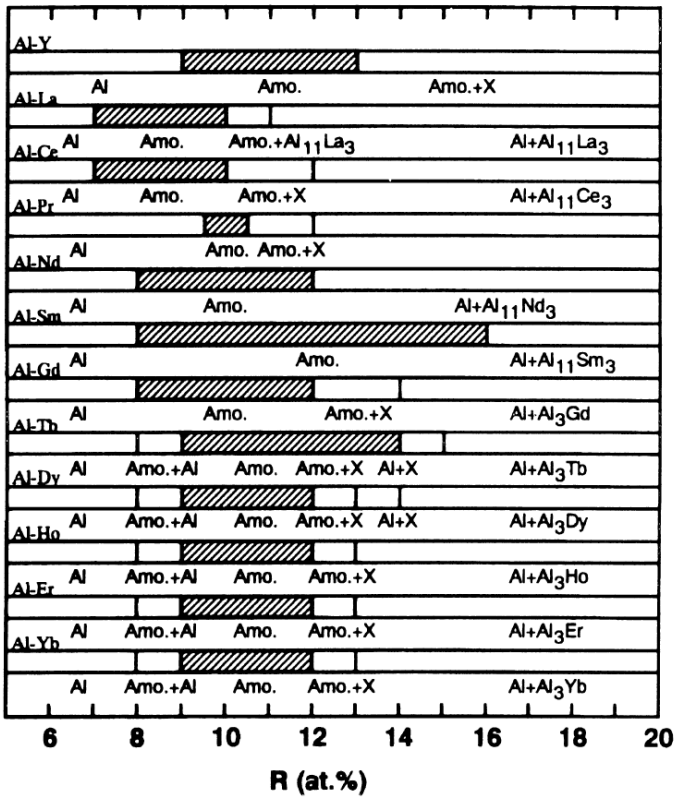

Figure 5.2 Glass forming range of Al-Re alloys [44].

The mechanisms for the formation and growth of the nanocrystals began to be investigated soon after their discovery in 1990. Al-Fe-Co glass forming alloys violate another rule of glass formation, the atomic size criterion proposed by Egami [219], which lead Hsieh, et. al. to investigate Al-Fe-Ce alloys with 90 at. % Al using pulsed neutron and synchrotron X-ray

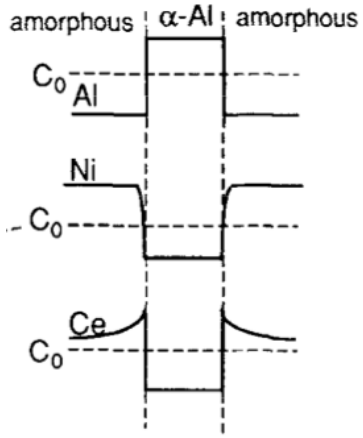

Figure 5.3 Compositional profile for Al-Ni-Ce showing strong chemical isolation of α-Fcc [45].

scattering in 1990 [220]. Their results indicated strong chemical and topological ordering that they indicated reduced the effective atomic radius to aid glass formation. A compilation of the scattering investigations of amorphous Al-based ternary alloys is available in a section in a review by Cheng and Ma [50].

Nakazato et. al investigated Al-Ni-Ce with DSC and TEM in 1993 [221], and their main conclusions were that the crystal growth was very fast, only existed when Al content exceed 87 at. %, and that there was no signal for nucleation in DSC, thus they suggested that the nuclei pre-existed. This argument was supported by another investigation using DSC [222]. In 1994, Hono et. al investigated Al-Ni-Ce using an atom probe field ion microscope [45], and their results indicated strong compositional segregation, which can be seen in Figure 5.3.

The amorphous-nanocrystal composites are formed by growing the FCC aluminum nanocrystals at a temperature at which the growth of the Al-R compound is suppressed [44]. It has been presented that nucleation of the other phases is suppressed due to interfacial effects isolating the pure Al regions, and that the long-range diffusion necessary (also the sluggish diffusion of RE in Al) prevents primary crystallization [218].

In 1997, Tsai et. al. used small angle X-ray scattering to determine strong composition fluctuations in Al-Ni-Ce at the composition of 87 at. % Al [223], further supporting the argument of Nakazato and confirming the results obtained by Hono. Wilde, et. al. investigated the Al-Sm binary system and formed an amorphous sample using mechanical means [224].

Usually when the glass transition temperature is investigated in these systems the onset FCC aluminum growth obfuscates the glass transition temperature. The amorphous samples formed by mechanical means did not exhibit crystal growth, and thus the T_g was able to be accurately determined to be 172^o C in $Al_{92}Sm_8$. In 2001, Wu et. al. applied modulated DSC of melt-spun ribbons to measure the glass transition [225], which agreed well with the measurement by Wilde. In 2005, Stratton et. al. used fluctuation electron microscopy (FEM) to investigate the ordering in Al-sm [226]. The technique examines spatial fluctuations in scattering patterns, a review of the technique was presented by Treacy, et. al. [227]. Stratton found medium-range order in amorphous $Al_{92}Sm_8$ at. % formed by rapid quenching, which supported the quenched-in nuclei theory, although the formation of the nuclei was not yet elucidated. Investigations by Kalay et. al. in 2008 using high resolution transmission electron microscopy, atom probe topography, and high energy X-ray diffraction confirmed that the nuclei were indeed quenched in from the melt, and that local ordering existed [228]. Further investigation of the structure of rapidly solidified Al-Sm in 2010 by Kalay et. al. lead to the claim that the medium range ordering in the liquid was the mechanism for nanocrystal formation [229], and additional analysis of Al-Tb using atom probe topography and fluctuating electron microscopy confirmed chemical separation of pure Al and Tb rich clusters, confirming the pure Al regions are the precursor to the FCC Al nanocrystals [230].

To date, all investigations of the Al-Sm and Al-Tb systems in far-from-equilbrium conditions were done by rapid cooling. In the current work, the deeply undercooled liquid state was examined using levitation drop calorimetry to investigate the unique liquid properties inherent to the Al-based glass forming alloys. Levitation processing enables access to high undercoolings for a period of minutes.

5.2 Enthalpy Measurements

The following Al-Tb and Al-Sm enthalpy measurements are going to be included in a publication titled "Thermal Analysis of Undercooled $Al_{90}Tb_{10}$ and $Al_{90}Sm_{10}$ at.% Melts by Electromagnetic Levitation Drop Calorimetry" with authors C. Tackes, Z. L. Royer, and R. E. Napolitano, the entire publication can be viewed in the appendix.

$Al_{90}Tb_{10}$ and $Al_{90}Sm_{10}$ at.% alloys were created from 99.999% pure Al, and rare earth purity of at least 99.995% overall by the Materials Preparation Center at Ames Laboratory [a] in an arc-melting furnace. The apparent spectral emissivity of each sample composition was determined using Eq. 4.5, with the reference T_m value from both calculated phase diagrams [231, 232] and DTA. The room temperature heat capacities were measured using stepwise DSC, the results of which are in Table 5.1. Applying the levitation drop calorimetry technique described in chapter 4 to $Al_{90}Tb_{10}$ and $Al_{90}Sm_{10}$ at.% alloys the enthalpy of the liquid as well as the undercooled liquid were obtained. In both cases it was determined that a linear fit is sufficient to represent the experimental data. The measured enthalpy increments are presented in Figure 5.4 and Figure 5.5. The heat capacity, $\frac{\delta H}{\delta T}$, is the slope of the fit and is presented in Table 5.2. For each material, it was necessary to check that the crystalline phases formed after being dropped into the calorimeter were consistent, as the formation of differing phases would affect the measured enthalpies. Using XRD and SEM, it was determined that the $Al_{90}Tb_{10}$ at.% samples formed Al_3Tb-δ and and f.c.c. aluminum, and the $Al_{90}Sm_{10}$ at.% samples formed Al_4Sm-β and f.c.c. aluminum. There is more variation in the $Al_{90}Sm_{10}$ at.% enthalpy measurements, which is likely a result of the higher vapor pressure of Samarium which is an experimental obstacle considering the necessity of removing the oxide layer in vacuum. This results in less oxide layer removal compared to the $Al_{90}Tb_{10}$ at.% samples, which acts as a heterogenous nucleation site, influencing the maximum undercooling achieved. The maximum relative undercooling achieved for $Al_{90}Tb_{10}$ at. %, $\Delta T/T_m = 0.185$, is consistent with the range reported for EML [185].

Table 5.1 Measured heat capacities at 298 K from stepwise DSC for use in Equation 4.7 with 95% confidence intervals given.

Sample (at. %)	C_p at 298 K (J/mol K)
$Al_{90}Tb_{10}$	23.3 ±0.19
$Al_{90}Sm_{10}$	23.8 ±0.36

The present work employs levitation drop calorimetry to quantify the enthalpy of undercooled marginal glassforming $Al_{90}Tb_{10}$ and $Al_{90}Sm_{10}$ at.% alloys. High energy X-ray diffraction (HEXRD) studies of liquid $Al_{91}Tb_9$ at.% above melting indicate a small intensity pre-peak at

Table 5.2 Determined heat capacity from linear fit of enthalpy data, and intercept for the form H(T) - H(298) = C_p·T + b with 95% confidence intervals given.

Sample	C_p (J/mol K)	b (kJ/mol)
$Al_{90}Tb_{10}$	45.79±0.86	-17.09±1.010
$Al_{90}Sm_{10}$	32.24±3.62	-1.521±4.397

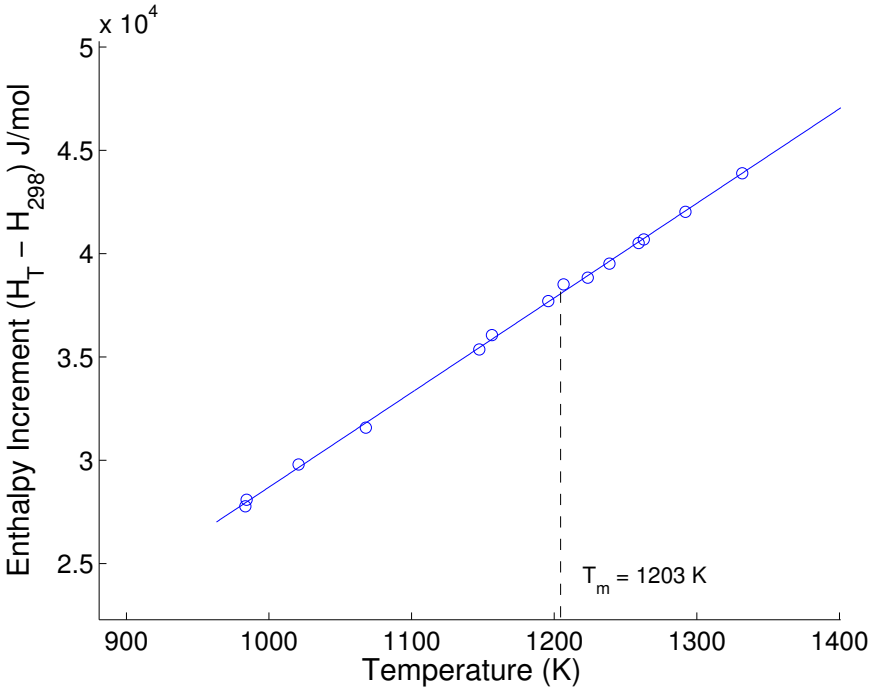

Figure 5.4 Measured enthalpy increments of $Al_{90}Tb_{10}$ alloy (○), and fit (solid line). T_{melt} is indicated by the dashed line.

low Q which is evidence for the existence ordering in the liquid [230]. HEXRD of as quenched samples revealed a higher intensity peak at the same location[230], and further analysis using fluctuation electron microscopy, atom probe topography suggested a highly networked medium range order structure.

The temperature dependence of the undercooled heat capacity can vary depending on the liquid behavior, i.e. 'fragile' or 'strong' liquids. For a strong liquid, $Pd_{40}Ni_{40}P_{20}$, the temperature dependence of the undercooled heat capacity has been shown to be linear [20], and it has also been shown that there can be essentially no temperature dependence to the heat capacity prior to a peak near T_g, such as the measured results for $Pd_{77.5}Cu_6Si_{16.5}$, a 'fragile'

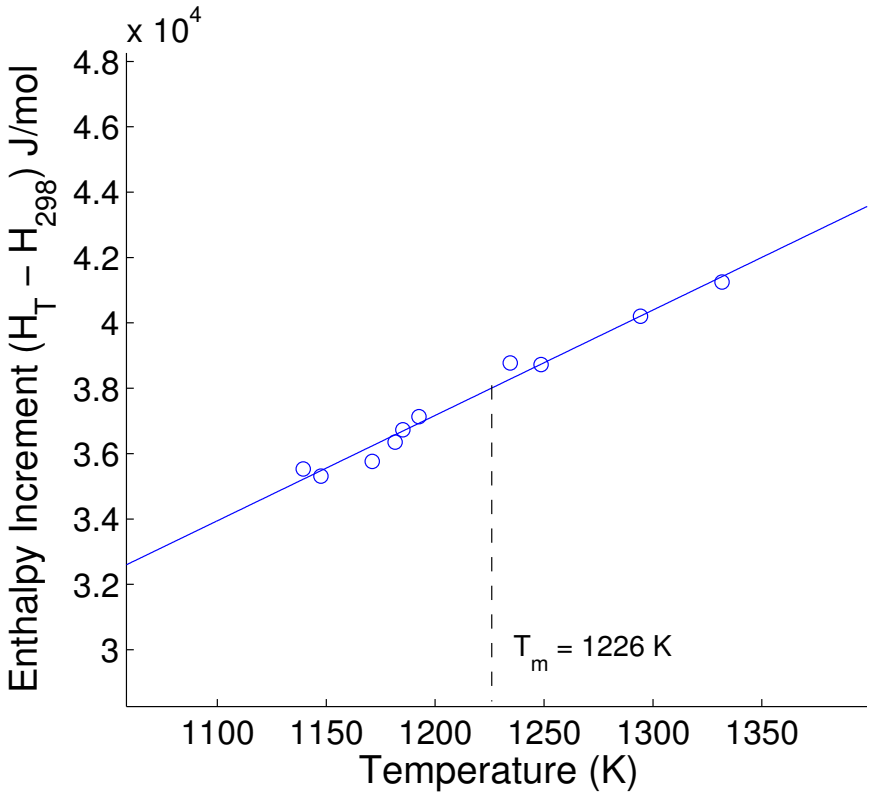

Figure 5.5 Measured enthalpy increments of $Al_{90}Sm_{10}$ alloy (○), and fit (solid line). T_{melt} is indicated by the dashed line.

liquid [20]. One of the best bulk metallic glass forming alloys, $Mg_{65}Cu_{25}Y_{10}$, has been shown to display very little temperature dependence of the heat capacity [4], similar to the results for other excellent glassforming alloys such as the Zr-based Vitreloy compositions [2]. Recent MD investigations reveal a strong correlation between the fraction of polyhedral structures observed as a function of temperature and the specific heat capacity as a function of temperature [24], indicating that fragile liquids undergo a large degree of structural ordering prior to glass formation. The heat capacity measurements presented here do not include any temperature dependence, which raises several questions regarding the dynamics of the ordering processes and liquid behavior of Al-RE alloys. The continued ordering could occur at lower temperatures, or the highly networked MRO may not reflect an experimentally observable deviation in heat capacity. For the Al-Re alloys, further undercooling is a difficult experimental range to access. Given the quenched in nanocrystal nuclei, the heat capacity of the undercooled liquid cannot

be determined from *in-situ* devitrification, and thus the only likely solution to further quantify the structural dynamics of Al-Re alloys is through the use of computational techniques, such as molecular dynamics.

5.3 Calculation of the Enthalpy of Mixing from Levitation Calorimetry

The following is a description of the motivation and use of the levitation calorimetry technique to determine the enthalpy of mixing, which will be included in a publication. Given that the publication also involves first-principles calculations and solution based modeling, the following text summarizes only the levitation calorimetry experiments. The manuscript is titled "Phase stability for the Al-Tb system: first-principles, experiments and solution-based modeling", by authors S.H. Zhou, Y. Huo, C. Tackes, and R. E. Napolitano.

The primary motivation for calculation the enthalpy of mixing using the levitation calorimeter is because the technique can be applied to reactive alloys. Group member S. Zhou applied the CALPHAD method to the Al-Tb system [232], and used solution calorimetry measurements to provide a comparison to the calculated model. It was found that significant reactions with the crucible occurred when terbium content of the alloy exceeded 10 at. %. Therefore the levitation calorimeter was employed to measure the enthalpy of $Al_{80}Tb_{20}$ at. %, and measured results for $Al_{90}Tb_{10}$ at. % were also used. It will be presented how the enthalpy of mixing can be determined from levitation calorimeter measurements.

Defining the enthalpy of liquid Al-Tb alloy as the sum of contributions of both the pure materials and the enthalpy of mixing,

$$H_{Liq} = x_{Al}H_{Al(Liq)} + x_{Tb}H_{Tb(Liq)} + \Delta H_{mix}, \tag{5.1}$$

and considering the measurement from the levitation calorimeter,

$$\Delta H = H_{Liq} - H_{298}, \tag{5.2}$$

it is evident that if H_{298} was known, the enthalpy of mixing could be determined.

Now considering a definition of H_{298},

$$H_{298} = x_{Al}H_{Al(FCC)} + x_{Tb}H_{Tb(HCP)} + \Delta H_f, \tag{5.3}$$

in which the contributions from the pure materials includes specification of the equilibrium phases, if we also have the enthalpy of formation of the compound the enthalpy at 298 K can be calculated.

The enthalpy of formation was calculated by S. Zhou using the Vienna ab initio simulation package (VASP), which calculates the total energy of the system and energy of each phase at 0 K, E^0. The enthalpy of formation can then be calculated by subtracting the energy of each phase:

$$\Delta H_f^0 = E_{total}^0 - x_{Al} E_{Al}^{0fcc} - x_{Tb} E_{Tb}^{0hcp} \tag{5.4}$$

More details are available in other publications using the same technique by S. Zhou [10, 46]. The enthalpies of the pure materials ($H_{Al(fcc)}$ and $H_{Tb(hcp)}$) are determined from the SGTE database [42].

For $Al_{80}Tb_{20}$ at. % the calculation of H_{298} is presented with H values from SGTE [42] and H_f from upcoming publication by S. Zhou:

$$H_{298} = 0.8 \cdot 4540 \frac{J}{mol} + 0.2 \cdot 9426 \frac{J}{mol} - 40 \frac{kJ}{mol} = -34.48 \frac{kJ}{mol} \tag{5.5}$$

Levitation samples were prepared by the Materials Preparation Center, and the enthalpy measured as outlined in Chapter 4. It was then necessary to check that the phases present were consistent with those used in the calculations, which was done with XRD and SEM. The XRD patterns for $Al_{90}Tb_{10}$ and $Al_{80}Tb_{20}$ at. % were overlaid as well as the peak positions for the equilibrium fcc Al and $AlTb_3$ phase and can be seen in Figure 5.18. SEM images for $Al_{90}Tb_{10}$ and $Al_{90}Tb_{20}$ can be seen in Figure 5.19.

The calculation can be seen in Table 5.3 and the results can be seen in Figure 5.6.

Table 5.3 Calculation of ΔH_{mix} from levitation calorimeter measurements. All enthalpy values are given in kJ/mol.

x(Tb) at. %	T_{drop} (K)	ΔH_{alloy}	$H_{T\delta}$	H_{liq}	ΔH_{mix}
0.1	1326.0	43.07	-17.11	25.69	-16.32
0.2	1406.5	54.54	-34.52	20.02	-25.48
0.2	1439.5	56.77	-34.55	22.21	-24.45

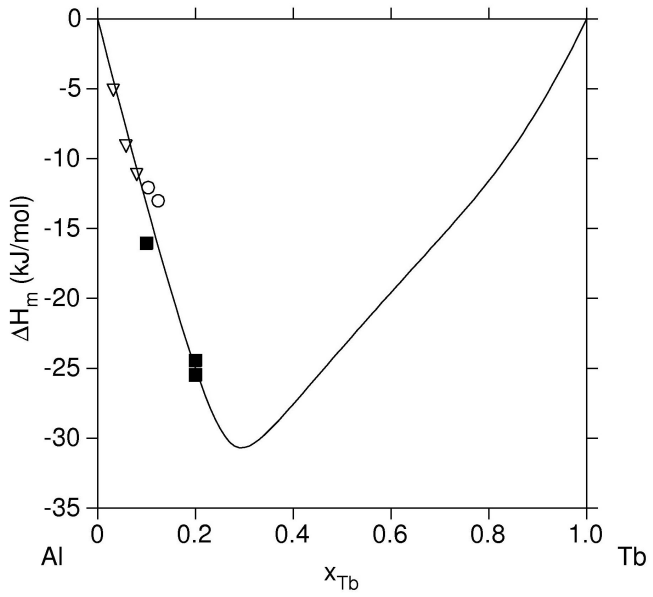

Figure 5.6 Enthalpy of mixing calculations done at 1200 K in comparison to solution calorimetry ($\triangledown, \circ$) and levitation calorimetry ($\blacksquare$) measurements. Solution calorimetry measurements were completed in two time periods, with $\triangledown$ and $\circ$ representing seperate experimental periods.

5.4 *In-situ* Metastable Phase Formation and Evolution

The following text describes some metastable phase observation experiments, some of which will likely be included in a publication. The publication is titled "Energetic investigation of metastable Al_5Sm-π, Al_4Sm-γ, $Al_{11}Sm_3 - \alpha$ and Al_4Sm-β phase formation", the author list has not been finalized yet.

Throughout the course of the $Al_{90}Sm_{10}$ enthalpy measurements, it was observed that the sample would solidify near maximum undercoolings with little or only a small recalescence. It was therefore hypothesized that the remaining energy was used to form a metastable phase. The maximum cooling rate provided by the cooling gas is 10 K/s, thus it is likely that the stable phase was not kinetically suppressed, but rather growth controlled due to reduction of heterogenous nucleation sites. This small recalescence can be seen in Figure 5.7. The visual difference in solidification behavior can be seen in Figure 5.13 and Figure 5.14. Considering only the Gibbs free energy of the phases, it can be seen that it would be plausible to form the high temperature metastable Al_4Sm-β phase on undercooling. The metastable Al_4Sm-β phase

would also require less diffusion to form, which is also an important factor in phase selection. The Gibbs free energy was calculated by S. Zhou, whose modeling for the metastable phases can be seen in his publication [46].

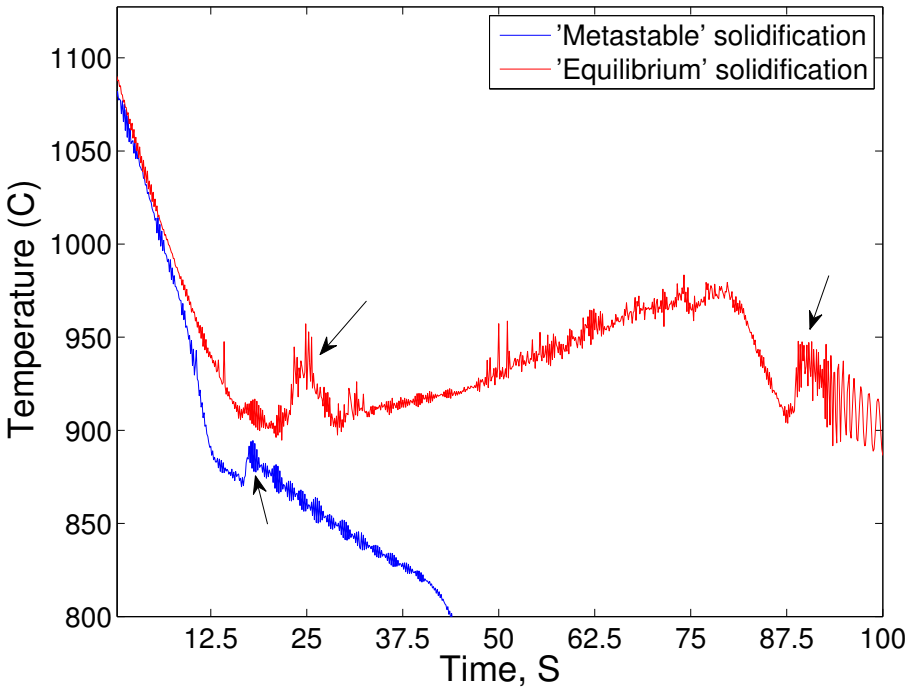

Figure 5.7 Temperature evolution of undercooled $Al_{90}Sm_{10}$. Recalescence events are indicated with arrows.

It was determined that applying isothermal holds would allow for investigation of the metastable phase evolution independent of other power input effects to the sample. This was achieved by maintaining a constant current setting in the power supply and a constant pressure gas atmosphere to cause a steady-state temperature condition. The isothermal holds can be seen in Figure 5.9.

It can be seen that after a period of time there is some ΔT resulting from some reaction. It was then attempted to quench the sample and perform XRD analysis to analyze the phases present. A summary of the sample temperatures and quenches are shown in Figure 5.10. The XRD results confirmed Al_4Sm-β + FCC Al phase formation for the 'metastable' behavior observed (the blue line in Figure 5.7) when quenched. The XRD results for the transformed state

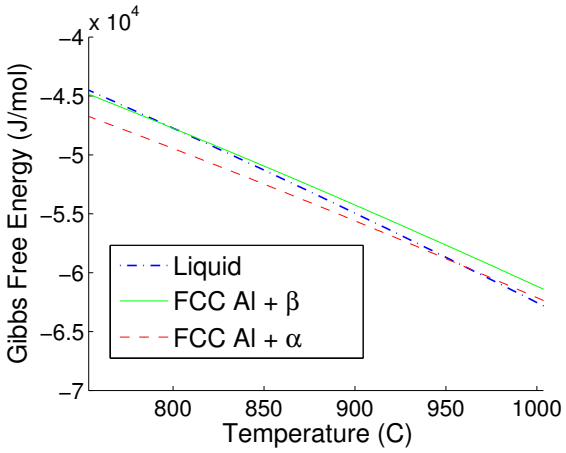

Figure 5.8 Calculated Gibbs free energies for liquid, FCC Al + Al_4Sm-β phase, and FCC Al + $Al_{11}Sm_3$-α phase. Calculated by S. Zhou from previously reported model [46].

have been inconclusive, where it has been found that either Al_4Sm-β+ FCC Al or $Al_{11}Sm_3$-α + FCC Al were detected. Mixtures of compounds were not detected. The most likely transformation is Al_4Sm-β to $Al_{11}Sm_3$-α based on the reported Gibbs free energy of the system [46]. The orthorhombic Al_4Sm-γ phase, and the Al_3Sm-δ phase were never observed. Observations by Zhou et. al. reported extended annealing times were required at the same temperatures to transform the $Al_{11}Sm_3$-α phase to Al_3Sm-δ phase [46] which is likely why the Al_3Sm-δ phase was never observed. The XRD pattern for the small recalescence event seen in Figure 5.7 can be seen in Figure 5.15.

Further XRD was performed on the lower undercooling sample in Figure 5.10 and refined using GSAS. The refinement initially indicated $Al_{11}Sm_3$-α + FCC Al, however the crystallographic information file (.cif) used for Al_4Sm-β was incorrect. The refinement was submitted to Dr. Kramer who used an experimental .cif file, which when used in refinement more clearly indicates that the sample was a mixture of $Al_{11}Sm_3$-α, Al_4Sm-β, and FCC Al. Several 2θ ranges are demonstrated below to show the phases present.

The quench results for the 'transformed' state are inconclusive for unknown reasons. Further experimentation would likely resolve this question. All other results, XRD and visual observations, show the transformation is as expected. The quench process is an experimental compromise, where the sample is dropped into the pure copper calorimeter. There is less heat

extraction control available in this process than what is desirable.

An interesting note is that studies investigating nucleation within the mushy zone have revealed that formation of metastable phases within the mushy zone causes a double recalescence event, as the nucleated metastable phase provides an interface to form the stable phase [47]. The double recalescence event can be seen in Figure 5.12. The presented hypothesis is the metastable Al_4Sm-β phase formation would provide a site for formation of a more stable phase (either $Al_{11}Sm_3$-α or Al_3Sm-δ), however the diffusion is likely so sluggish that a period of minutes is required for the formation of the stable phase. Ideally, in-situ scattering could be used to identify the phases directly.

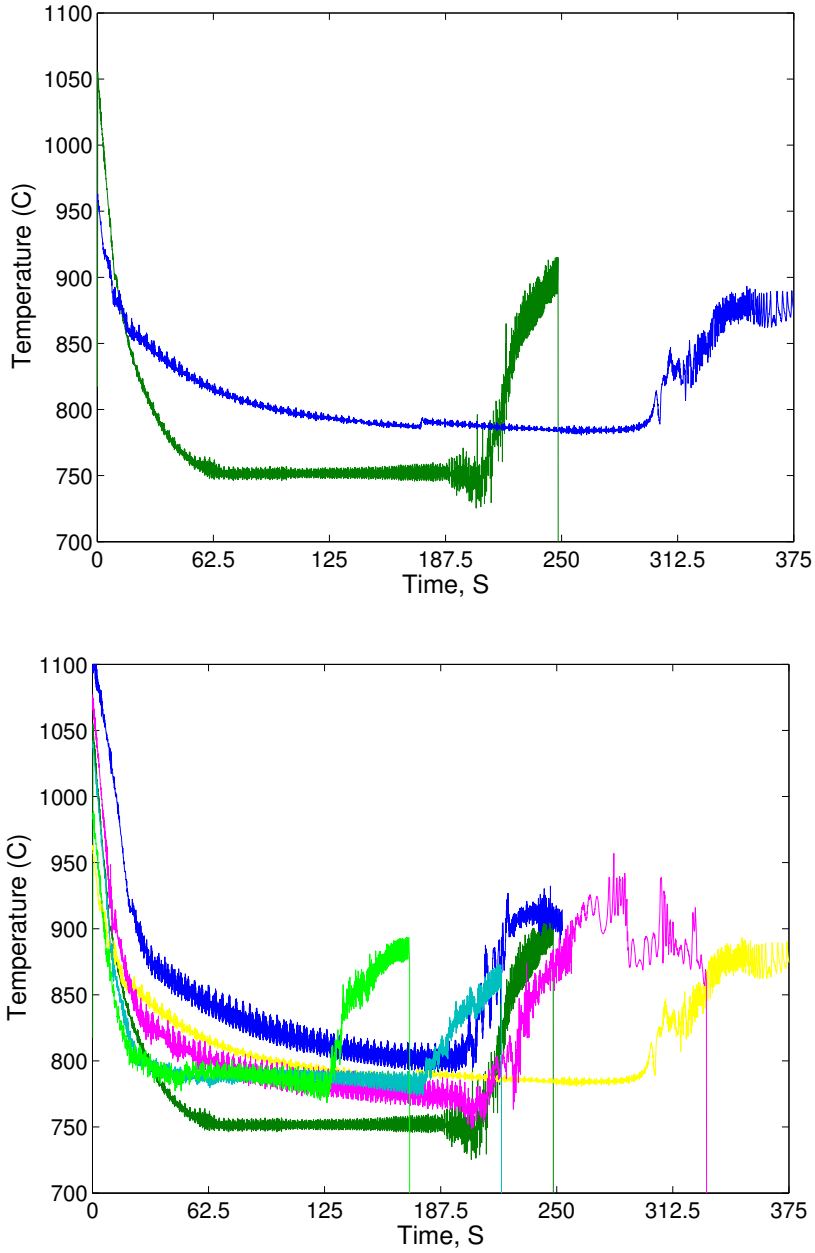

Figure 5.9 Approximate isothermal temperature holds for $Al_{90}Sm_{10}$ samples. The data presented represents a collection of multiple trials under similar experimental conditions. Sample sizes varied from 400-500 mg.

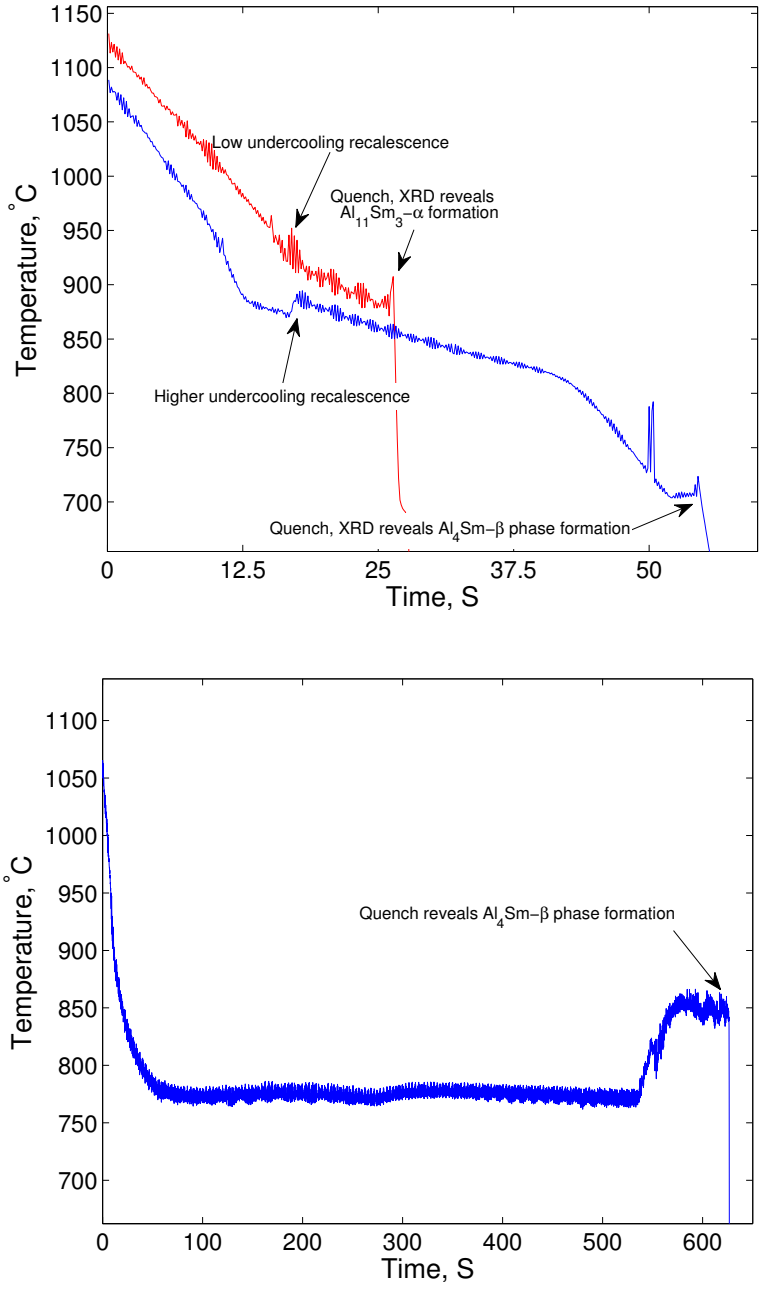

Figure 5.10 Summary of temperature data and determined phases from XRD. Upper figure describes the formation of Al_4Sm-β and $Al_{11}Sm_3$-α phases. Lower figure describes the quench and XRD for an isothermal temperature hold.

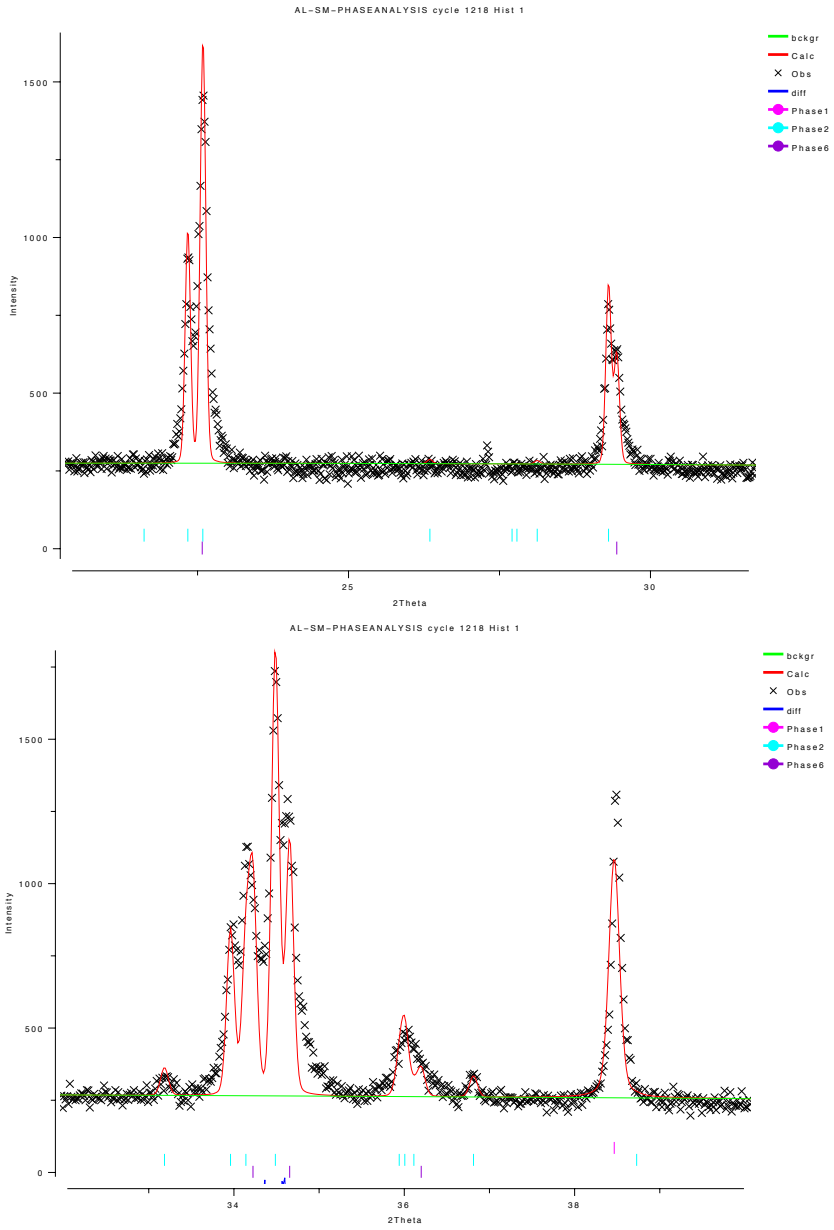

Figure 5.11 GSAS refinement data for low undercooling Al-Sm levitation sample in Figure 5.10. The teal markers (phase2 in legend) are the $Al_{11}Sm_3$-α reflections, the purple markers (phase6) are the experimental reflections for Al_4Sm-β, and pink markers (phase1) are FCC Al reflections. It can be most clearly seen in the bottom figure near 35-2θ that the sample is both Al_4Sm-β, $Al_{11}Sm_3$-α, and FCC Al.

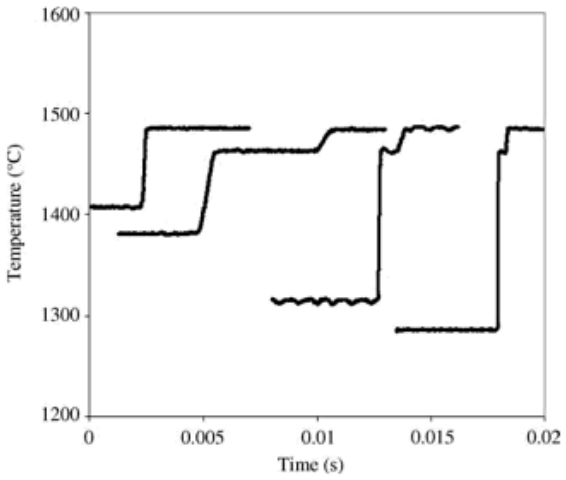

Figure 5.12 Double recalescence event in undercooled Fe-Cr-Ni (stainless steel) alloys from Matson [47].

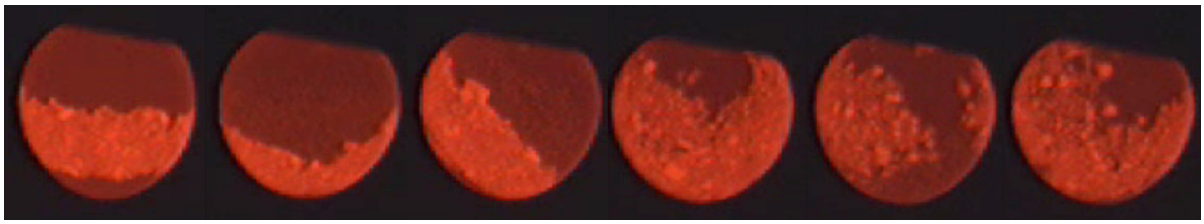

Figure 5.13 Observed 'equilibrium' solidification behavior of undercooled $Al_{90}Sm_{10}$, stirring can be observed as solid moves across the surface.

Figure 5.14 Observed 'metastable' solidification behavior of undercooled $Al_{90}Sm_{10}$, there appears to be considerably less stirring. The third and seventh frames show the same shape of solid as the sample rotates.

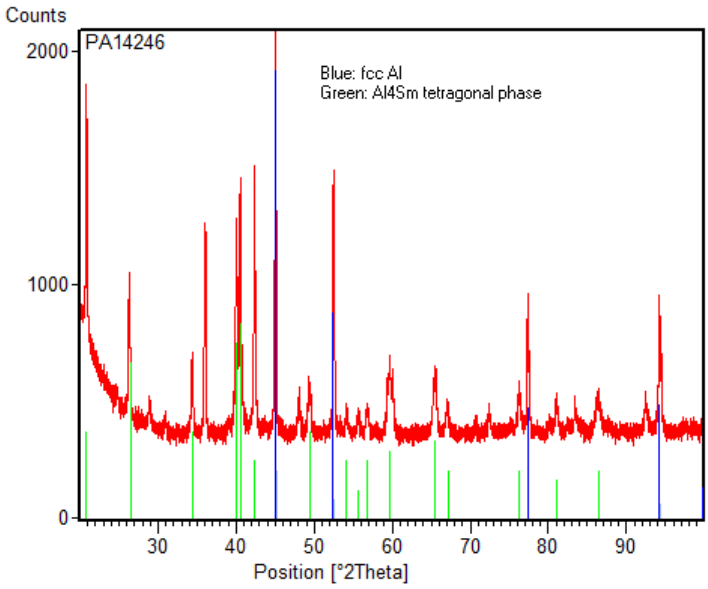

Figure 5.15 XRD pattern for 'metastable' temperature profile after quench. The pattern indicates the Al_4Sm-β + FCC Al phases.

Table 5.4 Measured enthalpy increments of $Al_{90}Tb_{10}$ at% alloy.

Mass (mg)	Temperature (K)	$H_T - H_{298}$ (kJ/mol)	% Deviation from fit
644.00	1331.9	43.86	0.01
738.65	1238.8	39.49	0.28
754.89	1223.6	38.81	0.25
594.55	1195.9	37.68	-0.11
479.64	1292.1	41.99	0.11
464.98	1259.2	40.48	0.13
603.91	1147.5	35.34	0.25
426.98	1068.0	31.55	0.73
464.13	1156.4	36.03	-0.55
347.12	1206.6	38.48	-0.93
509.67	1020.8	29.77	-0.49
516.47	984.4	28.07	-0.38
487.95	1262.8	40.66	0.10
454.60	983.5	27.75	0.60

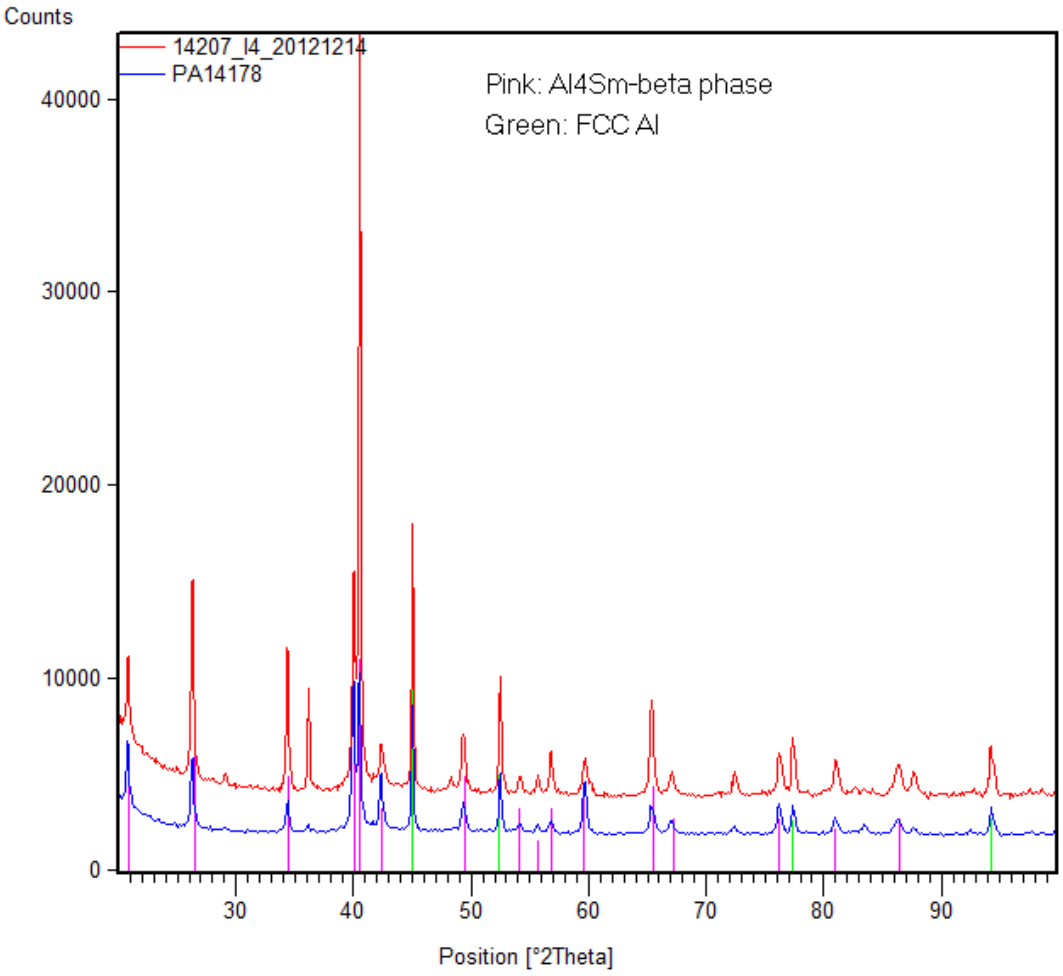

Figure 5.16 XRD analysis of $Al_{90}Sm_{10}$, at high undercooling (blue) and high temperature (red). Peak positions are given from crystal database for notated phases.

Table 5.5 Measured enthalpy increments of $Al_{90}Sm_{10}$ at% alloy

Mass (mg)	Temperature (K)	$H_T - H_{298}$ (kJ/mol)	% Deviation from fit
534.40	1294.3	40.20	0.02
493.28	1234.5	38.77	1.28
611.06	1248.6	38.73	0.02
567.90	1185.1	36.73	0.11
407.30	1192.6	37.13	0.54
493.87	1331.7	41.25	0.39
441.33	1181.6	36.35	0.61
472.00	1171.1	35.76	1.31
369.50	1147.6	35.31	0.48
350.88	1139.4	35.53	0.89

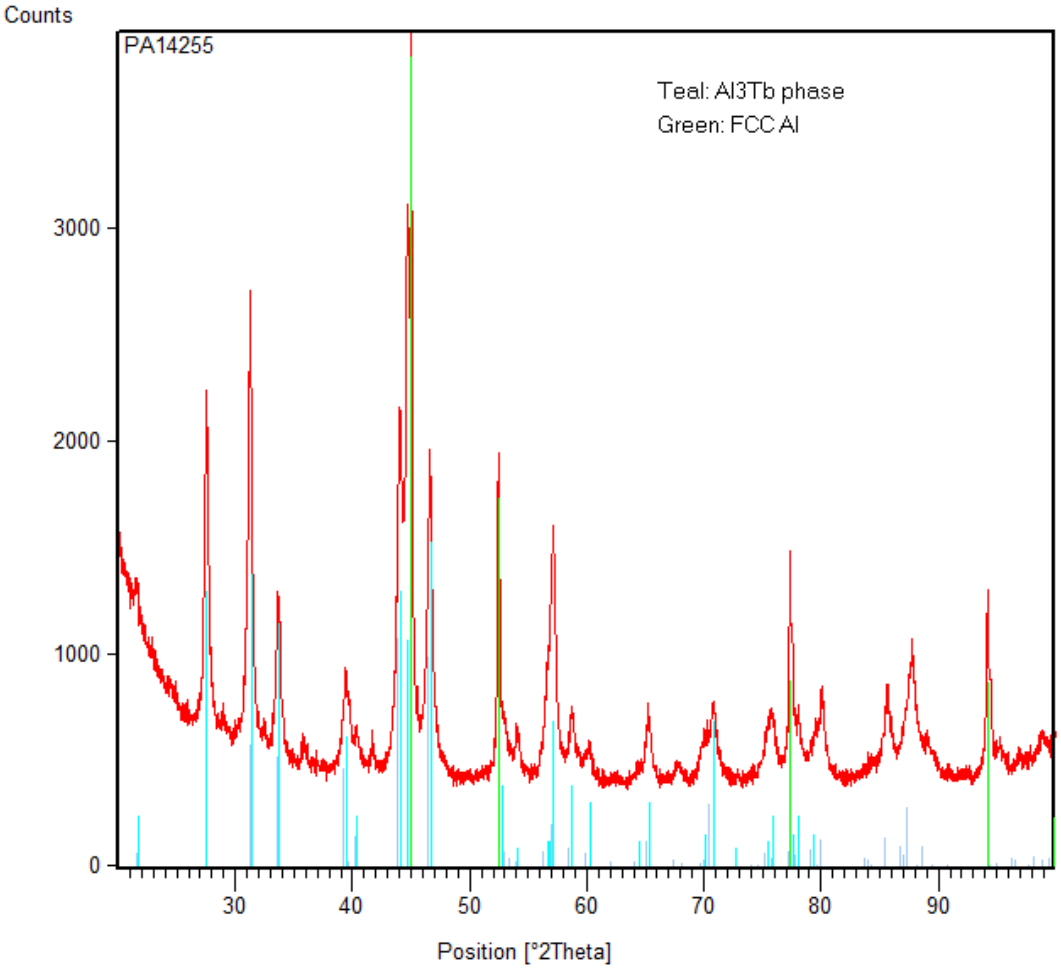

Figure 5.17 XRD analysis of $Al_{90}Tb_{10}$ at.% at high undercooling. Peak positions are given from crystal database for notated phases. The Al_3Tb phase is the most stable phase.

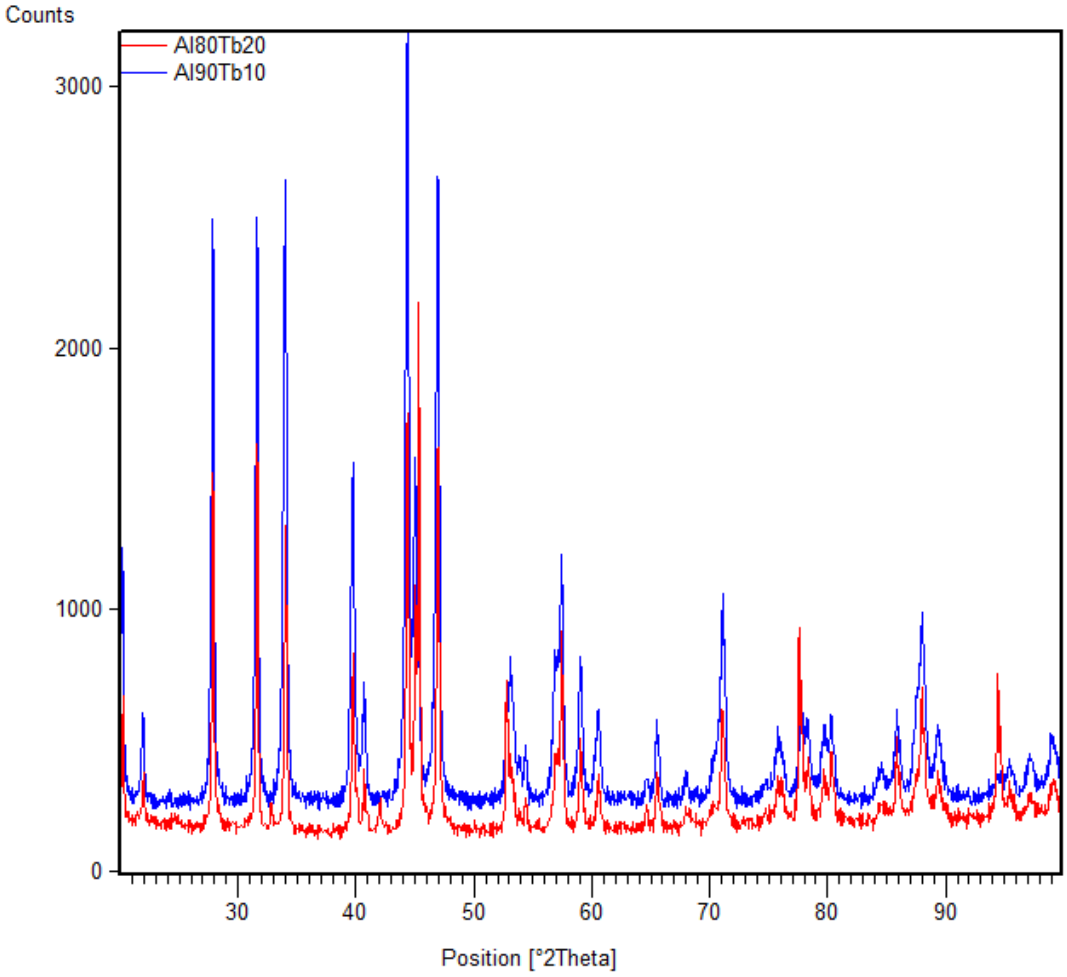

Figure 5.18 XRD analysis of $Al_{90}Tb_{10}$ and $Al_{80}Tb_{20}$. Peak positions are consistent showing in both cases the same phases were formed.

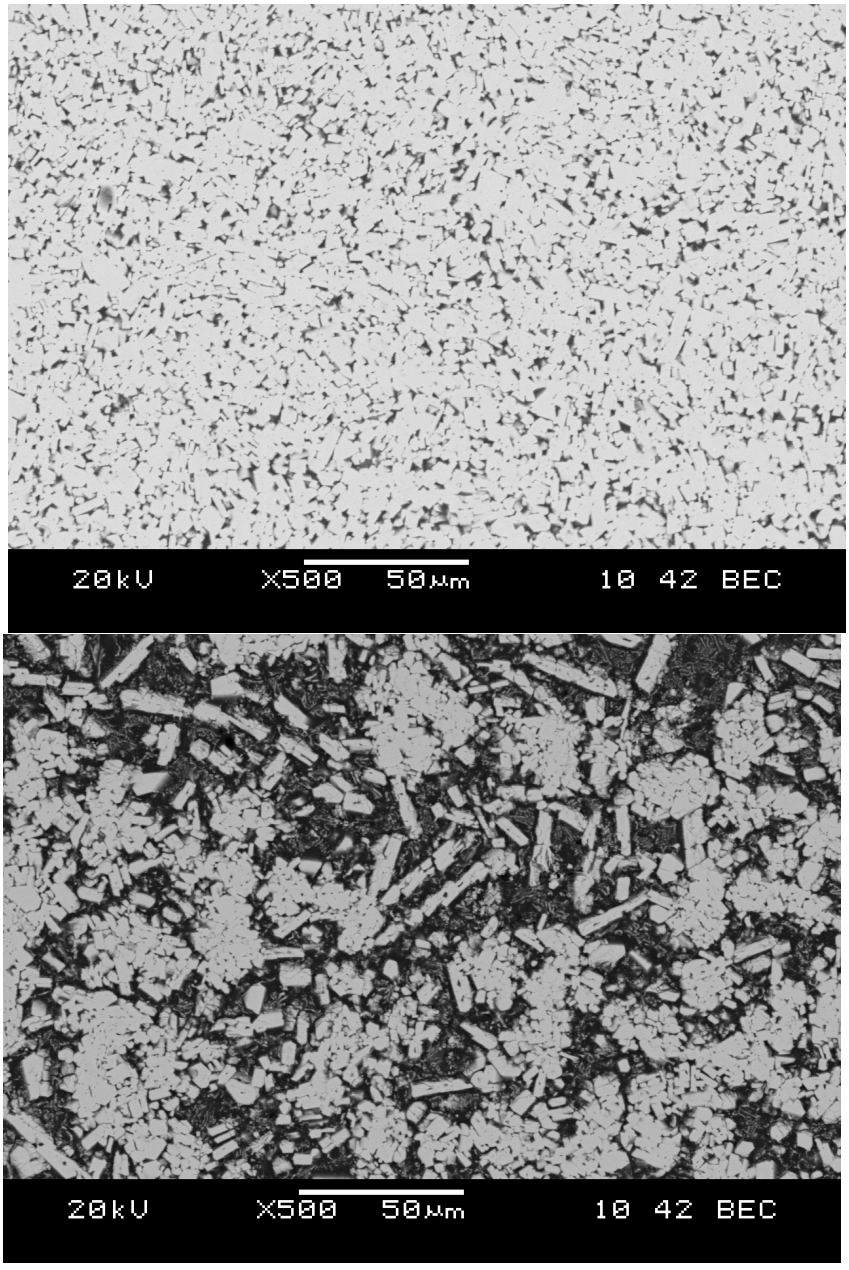

Figure 5.19 SEM images of AlTb alloys, upper image is $Al_{80}Tb_{20}$ at% and lower $Al_{90}Tb_{10}$ at%. EDS analysis revealed phases formed were consistent with XRD.

CHAPTER 6. Conclusions and Future Directions

In this work, the value of a levitation calorimeter apparatus is presented for investigations of various avenues relevant to analysis of the structures and dynamics of glass forming alloys. The undercooled heat capacity can be determined as a function of temperature, which provides insight into the configuration of the liquid that underpins its behavior and response to processing. Considering the available experimental pathways to the heat capacity of the undercooled liquid, levitation calorimetry is one of very few suitable techniques. The critical parameter in the thermodynamic models reviewed is the heat capacity of the undercooled liquid, which can be used to calculate the Gibbs free energy difference between the undercooled liquid and crystalline states, and elucidate the various pathways that can be selected by the far-from-equilibrium liquid.

Furthermore, the heat capacity is derived from measured enthalpy results. High temperature ($\sim$1000°C+) enthalpy measurements are often hard to achieve, and the method presented here can be reliably used for both undercooled liquids and be extended to higher temperatures. This was demonstrated for the measurement of both undercooled $Al_{90}Tb_{10}$ at.% and higher temperature reactive $Al_{80}Tb_{20}$ at.%.

Given the energetic hierarchy and associated structural pathways between various unstable and metastable states, a combination of computational and experimental methods are required to understand the complex dynamics. Computational methods can be very useful in the identification and energetic "ranking" of viable structures. Dynamic pathways are more difficult to predict, particularly when medium- or long-range interactions become important. In such cases, experimental techniques for *in-situ* measurement of such transitions become extremely valuable. EML is one such method, offering the ability to generate large nucleation-controlled undercooling conditions and formation of metastable phases, as well as retaining the ability to

control the sample temperature and monitor phase transitions.

From our results and analyses, we can draw the following conclusions:

- With appropriate instrument analysis through the testing of material standards, the electromagnetic levitation drop-calorimetry technique can provide reliable high-accuracy measurements of enthalpy and related heat capacity for metallic liquids.
- The technique was applied to two difficult to achieve experimental conditions, the far-from-equilibrium undercooled liquid, as well as a reactive liquid for which there was no suitable crucible for conventional calorimetry.
- Levitation calorimetry yielded the following two important measurements of alloy liquid heat capacity:
  - $C_p(Al_{90}Tb_{10})$ = 45.79 J/mol K over the temperature range 983.5 K - 1331.9 K
  - $C_p(Al_{90}Sm_{10})$ = 32.24 J/mol K over the temperature range 1139.4 K -1294.3 K
- The Al-Tb measurements reported here for 10 and 20 at.% Tb, are consistent with solution-based (CALPHAD) mixing enthalpy models.
- The reduction of heterogenous nucleation sites for levitation processed $Al_{90}Sm_{10}$ allowed for the *in-situ* formation of Al_4Sm-β and $Al_{11}Sm_3$-α metastable phases.

6.1 Future Directions

Given the small experimentally measured pre-peak in liquid $Al_{90}Tb_{10}$ at.%, which increases in intensity for melt-spun samples [230], the continued growth of the existing ordering is expected as temperatures decrease, however the dynamics of continued growth have not been well established. The measured results here for undercooled $Al_{90}Tb_{10}$ at.% and $Al_{90}Sm_{10}$ at.% melts indicate a constant specific heat capacity, which suggests two plausible scenarios. The continued ordering could occur at lower temperatures (consistent with fragile liquid behavior), or the highly networked MRO may not reflect an experimentally observable deviation in heat capacity. MD analyses are likely the only technique to further quantify the structures and

dynamics of the Al-Re systems due to the fact that lower temperatures are experimentally inaccessible.

The EML technique is robust in design and operating conditions, from high vacuum (10^{-6} mbar) to 1 atm and anywhere between with a variety of inert gas environments available. In this way, the technique is only limited to samples which are sufficiently conductive, and samples with issues such as vapor pressure can still be evaluated. In this way, it is presented that for whichever future directions may be taken in the analysis of structures and dynamics of metallic liquids, it is likely that the EML apparatus could provide insight when far-from-equilibrium conditions are required. As demonstrated, EML can be used for both the formation of metastable phases as well as quantification of the thermodynamic properties of the undercooled liquid.

A potential future direction would be the investigation of liquid ordering as temperatures are increased. Some BMG alloys have extended short-range order in the liquid near the melting point, and thus show small changes to the heat capacity as a function of temperature on undercooling. Measuring the heat capacity as temperatures increase would likely show a decrease in the heat capacity as the fraction of short-range ordering decreases. Additionally, in containerless processing, often the liquid is superheated prior to cooling. It would be of interest to quantify if this practice has some basis related to the elimination of pre-existing liquid structures.

APPENDIX A. Manuscript for Publication

The following is a manuscript intended for publication which includes the enthalpy measurements of $Al_{90}Tb_{10}$ and $Al_{90}Sm_{10}$. The other results in Chapter 5 are going to be included in separate publications with S.H. Zhou as primary author.

Thermal Analysis of Undercooled $Al_{90}Tb_{10}$ and $Al_{90}Sm_{10}$ at.% Melts by Electromagnetic Levitation Drop Calorimetry

C. Tackes, Z. L. Royer, R. E. Napolitano

Material Science and Engineering, Ames Laboratory, US DOE, Ames IA 50011, USA

Department of Material Science and Engineering, Iowa State University, Ames IA 50011, USA

Abstract

The enthalpies of Al-Tb and Al-Sm metallic liquids are measured over temperature ranges that extend well into the sub-liquidus (undercooled) regime. Deep undercooling is achieved experimentally using containerless electromagnetic levitation (EML), and enthalpy is quantified using an isoperibolic drop calorimetry technique. The constant pressure heat capacity, C_p, is determined from enthalpy measurements, and the results show that both alloys exhibit constant C_p over the entire ranges measured. Specifically, we find $C_p(Al_{90}Tb_{10}) = 45.79 \pm 0.86$ J/K-mol over the range 983-1332 K, and $C_p(Al_{90}Sm_{10}) = 32.24 \pm 3.62$ J/K-mol over the range 1139-1294 K. The results are discussed with respect to liquid behavior and the structural dynamics of binary Al-RE (rare-earth) alloys. Experimental details and the design of a compact calorimeter are presented.

Introduction

A principal barrier to the effective utilization of metallic glasses and the range of remarkable properties that they can exhibit is an incomplete understanding of the behavior of undercooled metallic liquids and the structural dynamics involved in the liquid-glass transition. A long history of research has focused on the glass transition, the related structural characteristics, and the various thermodynamic and kinetic factors that contribute to observed behavior, as summarized in a number of comprehensive reviews [233, 53, 2, 50, 51]. From the standpoint of controlling phases, structure, and properties through far-from-equilibrium processing routes that utilize the undercooled liquid or glassy phase as a transient or final state, making the connection between the short- and medium-range structure, chemical ordering and segregation, and bulk thermodynamic properties is a necessary but elusive objective of fundamental research. Central to this task is the quantification of basic properties such as heat capacity, density, viscosity, and diffusivity, where correlations between the measured temperature dependence of these properties has led to the identification of glass-forming liquid archetypes [76, 60].

Quantification of the fundamental thermodynamic properties of an undercooled liquid is a challenging prospect, given the inherent instability of the liquid phase below its liquidus or melting temperature. Reported measurements are scarce, as experimental techniques must suppress the energetic advantage for nucleation provided by container walls or impurities. Computational approaches have emerged as an extremely valuable tool here, but these must employ atomistic potentials that accurately predict the atomic bonding and associated short- and medium-range order, a criterion that is extremely difficult to verify directly, since such verification, again, calls for measurement of structural and physical properties in the undercooled state. For these reasons, any method capable of providing reliable direct measurement of the basic properties of the undercooled liquid state promises to break the considerable barriers to making the requisite connections required to understand and take full advantage of the novel transformation pathways afforded by glass-forming metals.

In the investigation reported here, we focus on the constant-pressure heat capacity, and employ a containerless electromagnetic levitation (EML) technique to study the behavior of

selected glass-forming metals over a temperature range that extends well into the sub-liquidus or highly undercooled regime. Through appropriate coil design [41] and the use of gas-cooling [35], this method can achieve a high degree of temperature control. A critical aspect of our study is the development and implementation of an isoperibolic drop calorimeter, with which we quantify the heat capacity and its temperature dependence for the selected test alloys.

We focus our study specifically on the Al-Tb and Al-Sm binary alloys, a sampling of the group of Al-RE alloys which have attracted interest for a combination of unique features such as multiple competitive crystalline phases [234, 46] and growth morphologies that can be observed at attainable cooling rates [235]. In addition, these marginal glass formers may illustrate several important features of structural and chemical ordering and their relationship to glass/crystal competition, where recent investigations [226, 228, 229, 230] of these binary systems have identified medium-range network structures, suggesting the origin of Al separation and nanocrystal formation which have been reported in these systems [44]. To date, all investigations of the glass forming behavior of Al-Sm and Al-Tb alloys has been conducted using rapid cooling techniques, such as melt-spinning. In the current work, the bulk thermodynamic properties of the undercooled liquid state are examined quasi-statically using levitation drop calorimetry.

Experimental Approach

The experimental procedure relies on the EML apparatus, which is used to melt and undercool the metallic samples, and a calorimeter, which has a precisely determined heat capacity. The metallic liquid is introduced into the calorimeter, and the temperature response of the calorimeter evaluated to determine the enthalpy of metallic melt.

Electromagnetic Levitation System

When a conductor is placed within a high-frequency induction coil, the time-varying magnetic field generated by the coil induces eddy-currents in the object. The interaction between the induced currents and the applied magnetic field produces an electromagnetic force, known as a Lorentz force. When the strength of the Lorentz force is greater than the strength of

gravity, the conductor levitates. The induced currents also generate resistive heating, which eventually melts the levitated conductor.

The EML system is contained within a stainless steel vacuum chamber, as Figure A.1 illustrates. The vacuum system consists of a roughing pump and a Pfeiffer turbo molecular pump which enables high-vacuum conditions (10^{-6} mbar). The high frequency power source is an Ameritherm Hot-Shot 6 kW power supply. The experimental coil geometry used in this work is from [48], in which optimized coil geometries are determined using a genetic algorithm coupled with an analytical model to determine a coil design with a reduced equilibrium sample temperature. The coil geometry is given in Figure A.2. A rotational actuator is used for initial sample manipulation, and once the sample is levitated, the actuator is rotated to position a vaporization shield for the infrared pyrometer. The cooling gas system consists of an inert gas cylinder (99.999% pure He), and a manually operated needle valve connected with copper tubing which is pointed at the sample approximately 6 inches away. When the pressure regulator on the gas cylinder is closed, the needle valve can be opened and evacuated along with the chamber to reduce the oxygen content in the gas lines. Once the sample temperature is decreased, and chamber pressure increased, the vaporization shield is rotated from the optical path of the IR pyrometer, enabling temperature measurements.

Levitated sample temperatures are measured using a non-contact infrared pyrometer, in which the basis of temperature measurement is from Planck's law, which describes the radiation emitted by a blackbody at a given temperature at thermal equilibrium. Levitated samples are considered greybodies, in which emissivities are used to relate the sample to blackbody conditions. The pyrometer used is a Pyrometer Instrument Company Pyrofiber II, which measures radiated intensities at 1.550 μm with focusing optics that produce a 1.9 mm spot size at a working distance of 14". The operating mode used produces readings at a rate of 8 Hz. The emissivities of the melts were determined using an equilibrium thermal signal, such as a melting plateau, to measure the apparent temperature at which point the emissivity may be corrected such that the known thermal signal is represented in the temperature measurement.

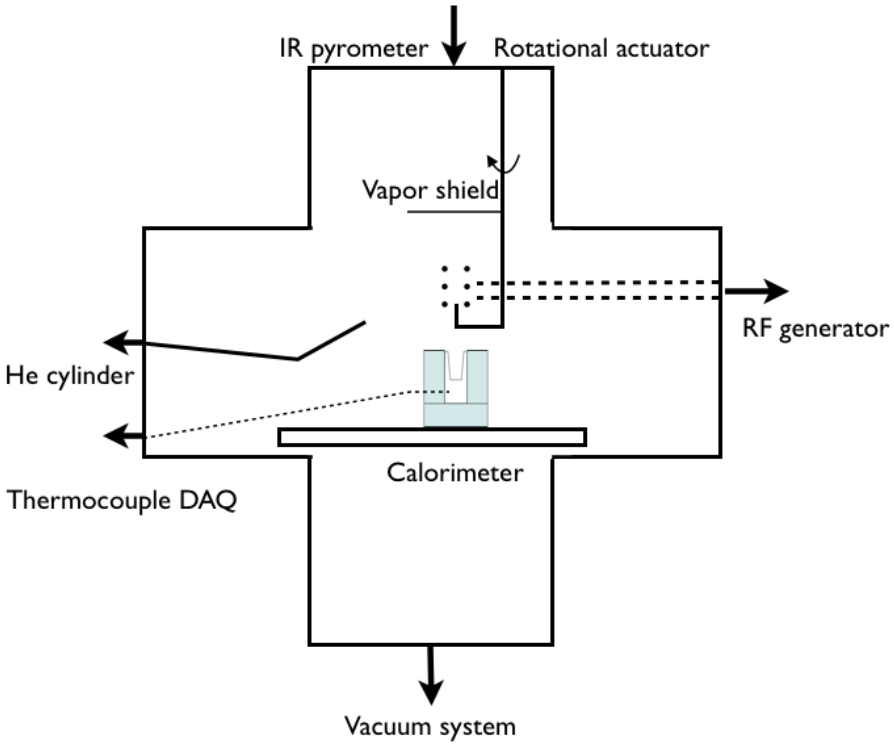

Figure A.1 Description of levitation drop calorimeter apparatus.

Using Wien's approximation to Planck's law the emissivity can be determined by [182, 28]

$$\epsilon_\gamma(T_m) = \exp\left[\frac{C_2}{\gamma}(\frac{1}{T_m} - \frac{1}{T_a})\right], \tag{A.1}$$

where T_m is the published or experimentally determined temperature of the thermal signal, T_a is the measured apparent temperature of the thermal signal from the pyrometer, γ is the wavelength measured by the pyrometer, and C_2 is the second radiation constant that has the value 14.388×10^6 nm K. Once the temperature measurement is determined to be stable, the RF power supply is turned off and the sample drops into the calorimeter.

Isoperibolic Drop Calorimeter

The principle of the drop calorimetry technique is the establishment of thermal equilibrium between the experimental sample at high temperature, and the calorimeter at room temperature, with precisely known heat capacity. Isoperibolic describes calorimeters for which a

z-Position (m)	Radius (m)
0.015	0.016
0.013	0.012
0.004	0.016
0.004	0.012
0.000	0.012
-0.0045	0.012

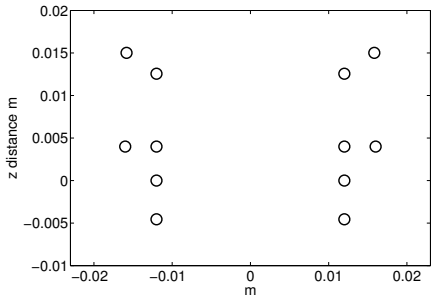

Figure A.2 Experimental coil geometry, from [48]. The first two positions in the table (the upper windings) are wound in an opposite direction to the lower windings to provide a restoring force.

constant surrounding temperature is maintained [101]. In contrast to adiabatic calorimeters, heat is lost to the surroundings during the sample-calorimeter heat transfer period, which requires temperature correction in order to accurately determine the enthalpy of the sample. In the isoperibolic design employed here the initial calorimeter temperature is the same temperature as the surroundings prior to the introduction of heat from the sample, at which point the calorimeter temperature rises (sample-calorimeter heat transfer period) and eventually returns to the initial temperature (calorimeter-surroundings heat transfer period). The calorimeter presented here is designed to be compact to minimize the duration of the sample-calorimeter heat transfer period, as well as the drop distance to reduce the overall sensitivity to temperature corrections for both the calorimeter as well as radiative and convective losses during the drop period.

The calorimeter, shown in Figure A.3, consists of a 1 inch diameter copper rod with an overall length of 2.25 inches that is insulated with open-cell polyimide foam. The open-cell foam is suitable for use in vacuum systems and prevents convection for a large fraction of the surface area of the calorimeter. The overall size of the copper rod is considerably smaller than what has been reported for use in this method previously, with a weight of approximately 160 grams. Compared to the ∼2.5 kg aluminum calorimeters of Bonnell [176] or the ∼6.4 kg copper calorimeter of Schaefers et. al. [28], the main heat transfer period is considerably shorter. The heat transfer period duration reported by Bonnell is on average 1000 seconds, and the average heat transfer period duration reported by Schaefers is 780 seconds. The heat transfer period

for the calorimeter presented here is approximately 40 seconds. The natural result is a shorter period for which heat can be lost, reducing the overall temperature correction and requirement for strict environmental control. For comparison, the reported temperature corrections by Bonnell are on average 1-2°C [176], in this work the overall temperature correction is .1-.5°C.

The calorimeter is thermally connected to the stainless steel chamber via a finite heat conduction path through the insulation. In this way, the initial and final calorimeter temperatures vary with each experiment but are approximately constant. The sample-calorimeter heat transfer period is on average 40 seconds, and the calorimeter-surroundings heat transfer period on average is two hours. The final calorimeter temperature after the period of two hours is on average within 3% of the initial temperature. As described previously, the small-size calorimeter was designed to minimize the sensitivity to overall temperature correction, and it is assumed the minor fluctuations in the final calorimeter temperature contribute to random error in the temperature correction. As will be demonstrated, the overall sensitivity of the technique is within the expected accuracy, ±1-3 % error, while having considerable advantages of size and construction simplicity making the technique suitable for implementation in existing EML systems designed for other purposes.

The temperature of the calorimeter block is measured using two type-K thermocouples and a National Instruments USB-9211 data acquisition system, in which the data is recorded at a rate of 3 Hz and accuracy of ±0.02 K. The temperature response of the calorimeter from a 880.2mg copper sample at 1426.4 K is plotted in Figure A.4, where it can be seen that the temperature of the calorimeter increases from the sample introduction and then begins to drift towards the initial calorimeter temperature.

Temperature Rise Correction

Considering the temperature response from before, shown in Figure A.4, the method for determining the corrected temperature rise is illustrated in Figure A.5. The method for determining the true temperature was presented by Bonnell [176] in which a newtonian cooling fit (where dT/dt is proportional to the temperature difference of the object and its surroundings) is applied to the cooling portion of the temperature response curve, which is then used to

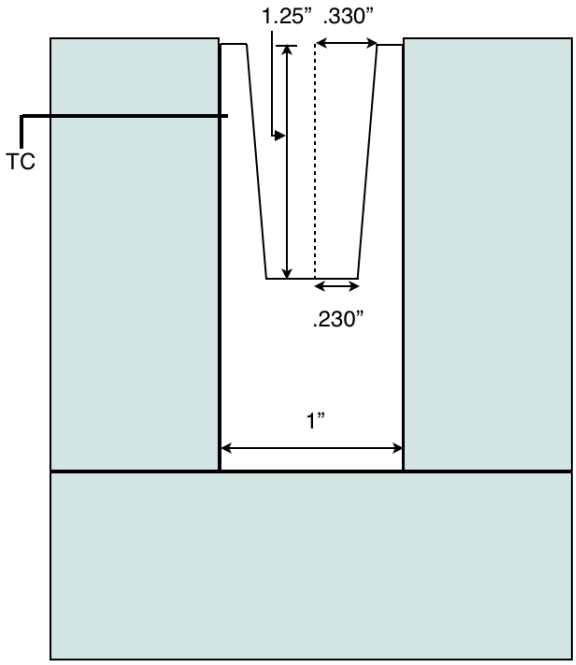

Figure A.3 Calorimeter design used in enthalpy determination.

determine the time-lag free temperature rise of the calorimeter. In the work of Bonnell [176], the calorimeter jacket temperature is fixed at a temperature in which it is greater than the calorimeter temperature throughout the experiment. The calorimeter temperature then constantly drifts towards the jacket temperature, and the corrected temperature rise is calculated at the mid-point of heat transfer. In this work, the initial and final calorimeter temperatures are assumed to be constant, thus the temperature correction is calculated at the time in which the sample was introduced. Illustrated in Figure A.5 is the increased calorimeter temperature, T_δ, defined as $Ti + \Delta T$ where T_i is the initial calorimeter temperature. T_δ is the thermal equilibrium temperature between the sample and calorimeter.

Enthalpy Determination

The enthalpy increment of a sample at temperature, T, can be calculated with respect to the increased calorimeter temperature, T_δ, in the following manner,

$$H(T) - H(T_\delta) = C_p^{cal} \Delta T \frac{M}{m} + Q_{lost} \frac{M}{m}, \tag{A.2}$$

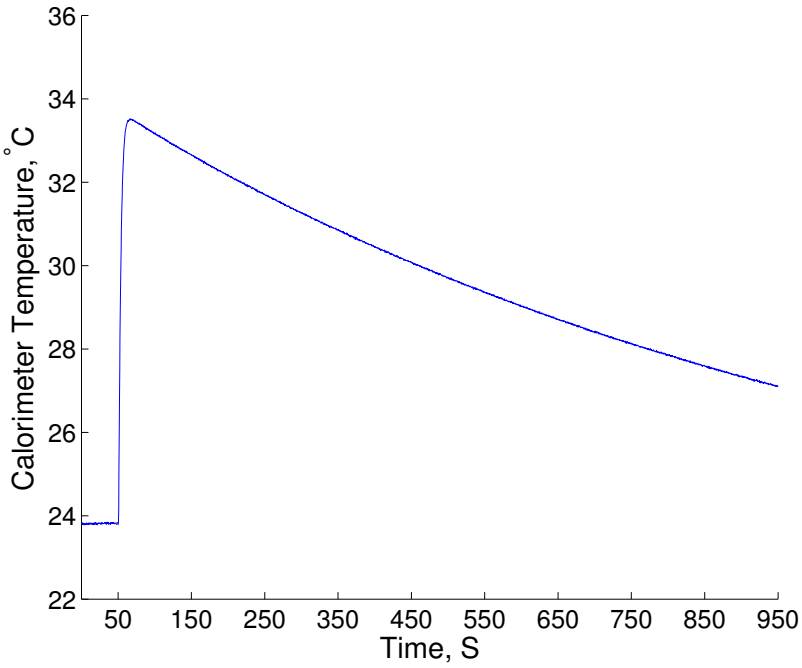

Figure A.4 Temperature response of the calorimeter from the introduction of a 880.2mg copper sample at 1426.4 K.

in which C_p^{cal} is the heat capacity of the calorimeter, ΔT is the corrected temperature rise of the calorimeter, M is the molar mass, m is the sample mass, and Q_{lost} represents the heat lost during the drop from radiation and convection ($Q_{lost} = Q_{rad.} + Q_{conv.}$). It is generally more useful to have measured enthalpy increments be in reference to the same final temperature, usually 298 K. This requires the addition of the remaining enthalpy from T_δ to 298 K, which requires experimental determination of the heat capacity or estimation from thermodynamic data. The heat capacity is generally assumed to be constant over the small range (6-10 K) [28, 90] of T_δ to 298 K. In this work, the heat capacity for pure materials is obtained from the Scientific Group Thermodata Europe (SGTE) database [42], and if no reference is available the heat capacity is measured in reference to a sapphire standard with application of the isothermal step method [129, 130] using a Perkin-Elmer Pyris 1 DSC. The room temperature heat capacity of the sample is used in the following manner,

$$H(T_\delta) - H(298) = C_p^{298}(T_\delta - 298), \tag{A.3}$$

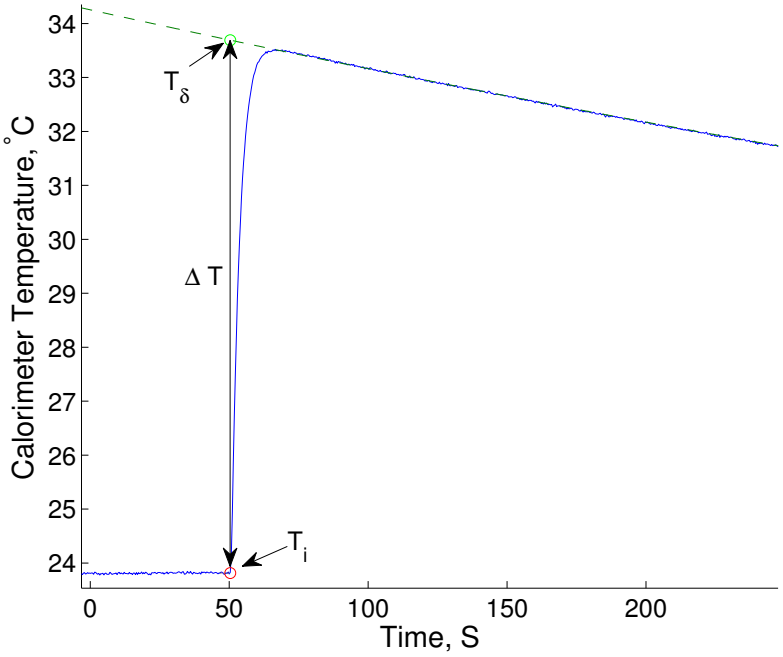

Figure A.5 Corrected temperature rise of the calorimeter block from the introduction of a 880.2mg copper sample at 1426.4 K.

which is added to Equation A.2 to calculate the enthalpy increment for a fixed reference temperature, $H(T) - H(298)$, which has been commonly used [121, 169, 90, 184],

$$H(T) - H(298) = C_b \Delta T_b \frac{M}{m} + Q_{lost} \frac{M}{m} + [H(T_\delta) - H(298)]. \tag{A.4}$$

Q_{rad} can be calculated using Stefan and Boltzmann's law for the sample drop period [28],

$$Q_{rad} = \epsilon_t \sigma A (T_s^4 - T_r^4) t_d \tag{A.5}$$

where ϵ_t is the total hemispherical emissivity, σ is the Stefan-Boltzmann constant of value 5.67×10^{-8} J S^{-1} m^{-2} K^{-4}, A is the surface area of the sample, t_d is the time of the drop period, T_s is the temperature of the sample, and T_r is the temperature of the surroundings, room temperature in this calculation. The total hemispherical emissivity is generally not known, others have presented estimating the value from the determined spectral emissivity [176]. The surface area can be estimated from the assumption of a spherical sample, where the volume can be calculated from the the liquid density to determine the surface area ($A = 4\pi r^2$). In some

cases the liquid density is reported, otherwise it has been presented that estimating the liquid density to be 10% less than the room temperature crystalline state is reasonably consistent with reported data [186]. The drop time, t_d can be determined by assuming free fall conditions,

$$t_d = \left(\frac{2h}{g}\right)^{1/2} \tag{A.6}$$

where h is the drop height, and g the standard acceleration due to gravity, 9.806 m/s^2.

The magnitude of the radiative losses during the drop period is small for moderate temperatures, noting the T^4 dependence. Considering pure aluminum, m = 509.4 mg, A = 8.02 x 10^{-4} m^2 (from liquid density of 2.375 g/cm^3 [195]), T_s = 1389 K, T_r = 298 K, t_d = 0.178 seconds, ϵ_t = 0.084 (value estimated as 20% more than the spectral emissivity, from [121], the enthalpy lost was 133.9 J/mol which represents 0.3% of the measured enthalpy increment.

Convective heat losses are calculated using the method presented by Stretz [121], where the primary assumptions are a stationary spherical sample where the gas flow velocity is approximated as the free-fall sample drop velocity. The heat losses due to convection can be written as

$$Q_{conv.} = A(T_s - T_g)\int_0^{t_d} \alpha \ \mathrm{d}t, \tag{A.7}$$

where t_d is the sample drop time, A the surface area, T_s the sample temperature, T_g the gas temperature (usually assumed 298 K),and α the heat transfer coefficient,

$$\alpha = \frac{\lambda}{D}\left[2 + 0.6(\mathrm{Re})_f^{1/2}(\mathrm{Pr})_f^{1/3}\right], \tag{A.8}$$

where λ is the gas thermal conductivity, D the sample diameter, Re the Reynolds number, and Pr the Prandtl number. The Reynolds and Prandtl number are calculated using the gas film temperature ($T_f = \frac{(T_s - T_g)}{2}$). The Reynolds number and Prandtl number are defined as

$$\mathrm{Re}_f = \left(\frac{D\rho_g v_{gas}}{\mu_f}\right) \tag{A.9}$$

and

$$\mathrm{Pr}_f = \left(\frac{C_p^{gas}\mu_f}{\lambda}\right) \tag{A.10}$$

where v_{gas} is the gas velocity, ρ_g the gas density, μ_f the kinematic viscosity at T_f, C_p^{gas} the gas heat capacity. As an approximation for the gas velocity, the sample velocity as a function

of drop time is substituted, where the modified Reynolds number takes the following form,

$$\mathrm{Re}'_f = \left(\frac{D \rho_g g t_d}{\mu_f} \right). \tag{A.11}$$

When the modified Reynolds number is combined into Equation A.8, and Equation A.7 evaluated, the final form can be written as

$$Q_{conv.} = A(T_s - T_g) \frac{\lambda}{D} \left[2t_d + 0.4(t_d)^{3/2} \left(\mathrm{Re}'_f \right)^{1/2} \left(\mathrm{Pr}_f \right)^{1/3} \right]. \tag{A.12}$$

Considering again pure aluminum, $m = 509.4$ mg, $A = 8.02$ x 10^{-4} m^2, $T_s = 1389$ K, $T_g = 298$ K, the total enthalpy lost is 265 J/mol, which is 0.61% of the total heat content. Convective losses are linearly temperature dependent $(T_s - T_g)$ compared to the fourth order dependence for radiative losses $(T_s^4 - T_r^4)$, meaning the overall sensitivity to temperature dependent changes is decreased. Due to a hardware limitation, gas pressure measurements are limited to the range 1x10^{-6} to 30 mbar, whereas experimental conditions can exceed 30 mbar for some materials. Due to this limitation, convective losses are assumed to be negligible.

Calorimeter Calibration

The heat capacity of the calorimeter is determined using 99.999% pure aluminum. Enthalpy increments are measured and calculated with Equation A.4, and the results compared to the value in the SGTE database [42]. The heat capacity of the calorimeter, C_b, is then adjusted to minimize the error between the measured results and the reference. The apparent spectral emissivity of unoxidized liquid aluminum at 1.550 μm, ϵ_γ, was determined to be 0.07. The results from calibration are listed in Table A.1 and shown in Figure A.6 where it can be seen that the technique is precise, in that experimental measurements show little variation in comparison to the reference for a given calorimeter heat capacity.

Once the calorimeter is calibrated, another material of well known enthalpy is evaluated using the levitation calorimeter to confirm the calibration value. Pure copper is well described in literature and is chosen to evaluate the calibration. The apparent spectral emissivity of liquid copper, ϵ_γ at 1.550 μm was determined to be 0.019. The measured enthalpy increments are summarized in Figure A.7 and Table A.2.

Table A.1 Measured enthalpy increments of pure aluminum used for calorimeter calibration.

Mass (mg)	Temperature (K)	$H_T - H_{298}$ (kJ/mol)	% Deviation from [42]
509.43	1389.7	43.30	0.05
514.64	1227.5	38.20	-0.07
515.57	1264.0	39.37	-0.09
518.00	1184.5	36.81	0.01
512.75	1342.9	41.85	-0.03
516.01	1153.0	35.76	0.11
509.10	1114.7	34.65	-0.12
514.52	1072.1	33.22	0.03
487.59	1182.4	36.70	0.10

Table A.2 Measured enthalpy increments of pure copper.

Mass (mg)	Temperature (K)	$H_T - H_{298}$ (kJ/mol)	% Deviation from [42]
878.2	1426.5	44.56	0.32
848.5	1536.3	47.87	0.60
728.3	1568.8	49.14	0.09
740.0	1505.6	47.23	-0.06

Indeed, the drop calorimetry method is successful in determining the enthalpy of liquid melts within 1%. The error observed is likely a result of the combination of uncertainty involved in experimental emissivity determination for both copper and aluminum, which is a limitation resulting from the necessity of non-contact temperature measurement.

Results

$Al_{90}Tb_{10}$ and $Al_{90}Sm_{10}$ at.% alloys were created from 99.999% pure Al, and rare earth purity of at least 99.995% overall by the Materials Preparation Center at Ames Laboratory [a] in an arc-melting furnace. The apparent spectral emissivity of each sample composition was determined using Eq. A.1, with the reference T_m value from both calculated phase diagrams [231, 232] and DTA. The room temperature heat capacities were measured using stepwise DSC, the results of which are in Table A.4. Applying the levitation drop calorimetry technique to $Al_{90}Tb_{10}$ and $Al_{90}Sm_{10}$ at.% alloys the enthalpy of the liquid as well as the undercooled liquid were measured. In both cases it was determined that a linear fit is sufficient to represent

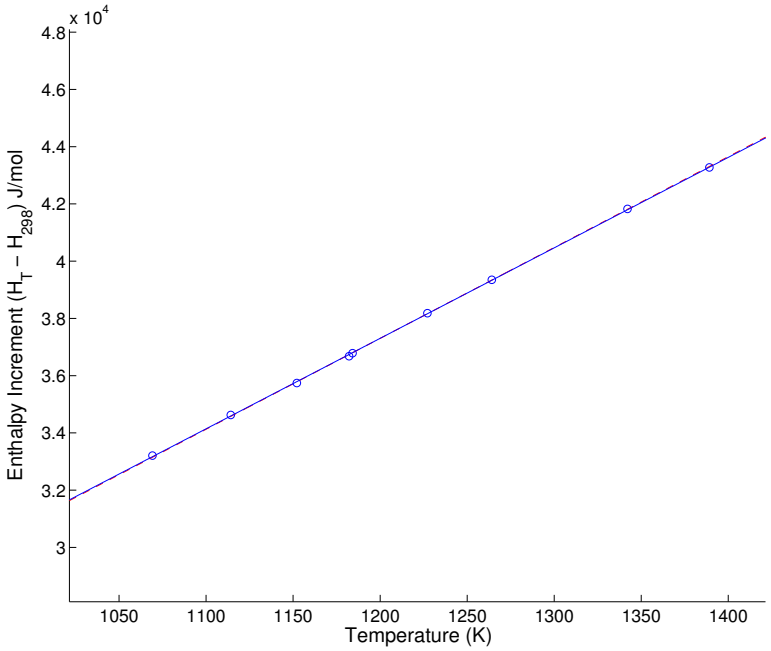

Figure A.6 Measured enthalpy increments of pure aluminum for calibration (∘), and linear fit (solid line). Red dashed line for reference is from the SGTE database [42].

the experimental data. The measured enthalpy increments are presented in Figure A.8 and Figure A.9. The heat capacity, $\frac{\delta H}{\delta T}$, is the slope of the fit and is presented in Table A.5. For each material, it was necessary to check that the crystalline phases formed after being dropped into the calorimeter were consistent, as the formation of differing phases would affect the measured enthalpies. Using XRD and SEM, it was determined that the $Al_{90}Tb_{10}$ at.% samples formed Al_3Tb-δ and and f.c.c. aluminum, and the $Al_{90}Sm_{10}$ at.% samples formed Al_4Sm-β and f.c.c. aluminum. There is more variation in the $Al_{90}Sm_{10}$ at.% enthalpy measurements, which is likely a result of the higher vapor pressure of Samarium which is an experimental obstacle considering the necessity of removing the oxide layer in vacuum. This results in less oxide layer removal compared to the $Al_{90}Tb_{10}$ at.% samples, which acts as a heterogenous nucleation site, influencing the maximum undercooling achieved. The maximum relative undercooling achieved for $Al_{90}Tb_{10}$ at. %, $\Delta T/T_m = 0.185$, is consistent with the range reported for EML [185].

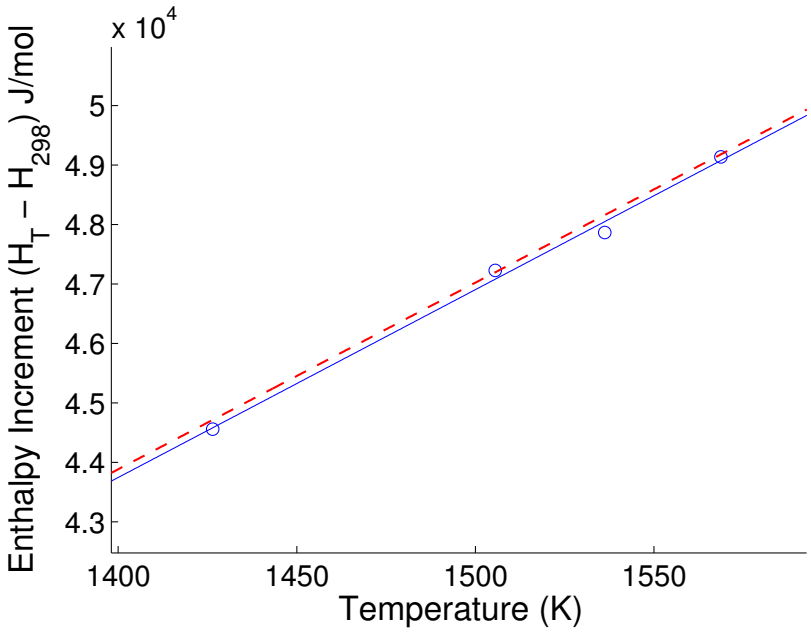

Figure A.7 Measured enthalpy increments of pure copper (○) and linear fit (solid line). Red dashed line for reference is from the SGTE database [42].

Table A.3 Determined liquid and undercooled liquid heat capacity from linear fit of enthalpy data, and intercept for the form H(T) - H(298) = C_p·T + b, with 95% confidence intervals given.

Sample	C_p (J/mol K)	b (kJ/mol)	% Deviation from [42]
Al	31.76±0.31	-0.808±0.37	-0.03
Cu	31.59±7.06	-0.479±10.67	-0.67

Discussion

The present work employs levitation drop calorimetry to quantify the enthalpy of undercooled marginal glassforming $Al_{90}Tb_{10}$ and $Al_{90}Sm_{10}$ at.% alloys. High energy X-ray diffraction (HEXRD) studies of liquid $Al_{91}Tb_9$ at.% above melting indicate a small intensity pre-peak at low Q which is evidence for the existence ordering in the liquid [230]. HEXRD of as quenched samples revealed a higher intensity peak at the same location[230], and further analysis using fluctuation electron microscopy, atom probe topography suggested a highly networked medium range order structure.

The temperature dependence of the undercooled heat capacity can vary depending on the

Table A.4 Measured heat capacities at 298 K from stepwise DSC for use in Equation A.3 with 95% confidence intervals given.

Sample (at. %)	C_p at 298 K (J/mol K)
$Al_{90}Tb_{10}$	23.3 ±0.19
$Al_{90}Sm_{10}$	23.8 ±0.36

Table A.5 Determined heat capacity from linear fit of enthalpy data, and intercept for the form H(T) - H(298) = C_p·T + b with 95% confidence intervals given.

Sample	C_p (J/mol K)	b (kJ/mol)
$Al_{90}Tb_{10}$	45.79±0.86	-17.09±1.010
$Al_{90}Sm_{10}$	32.24±3.62	-1.521±4.397

liquid behavior, i.e. 'fragile' or 'strong' liquids. For a strong liquid, $Pd_{40}Ni_{40}P_{20}$, the temperature dependence of the undercooled heat capacity has been shown to be linear [20], and it has also been shown that there can be essentially no temperature dependence to the heat capacity prior to a peak near T_g, such as the measured results for $Pd_{77.5}Cu_6Si_{16.5}$, a 'fragile' liquid [20]. One of the best bulk metallic glass forming alloys, $Mg_{65}Cu_{25}Y_{10}$, has been shown to display very little temperature dependence of the heat capacity [4], similar to the results for other excellent glassforming alloys such as the Zr-based Vitreloy compositions [2]. Recent MD investigations reveal a strong correlation between the fraction of polyhedral structures observed as a function of temperature and the specific heat capacity as a function of temperature [24], indicating that fragile liquids undergo a large degree of structural ordering prior to glass formation. The heat capacity measurements presented here do not include any temperature dependence, which raises several questions regarding the dynamics of the ordering processes and liquid behavior of Al-RE alloys. The continued ordering could occur at lower temperatures, or the highly networked MRO may not reflect an experimentally observable deviation in heat capacity. For the Al-Re alloys, further undercooling is a difficult experimental range to access. Given the quenched in nanocrystal nuclei, the heat capacity of the undercooled liquid cannot be determined from *in-situ* devitrification, and thus the only likely solution to further quantify the structural dynamics of Al-Re alloys is through the use of computational techniques, such as molecular dynamics.

Table A.6 Measured enthalpy increments of $Al_{90}Tb_{10}$ at% alloy.

Mass (mg)	Temperature (K)	$H_T - H_{298}$ (kJ/mol)	% Deviation from fit
644.00	1331.9	43.86	0.01
738.65	1238.8	39.49	0.28
754.89	1223.6	38.81	0.25
594.55	1195.9	37.68	-0.11
479.64	1292.1	41.99	0.11
464.98	1259.2	40.48	0.13
603.91	1147.5	35.34	0.25
426.98	1068.0	31.55	0.73
464.13	1156.4	36.03	-0.55
347.12	1206.6	38.48	-0.93
509.67	1020.8	29.77	-0.49
516.47	984.4	28.07	-0.38
487.95	1262.8	40.66	0.10
454.60	983.5	27.75	0.60

Conclusions

From the measured results and analysis, we draw the following conclusions:

(i) With appropriate instrument analysis through the testing of material standards, the electromagnetic levitation drop-calorimetry technique can provide reliable high-accuracy measurements of enthalpy and related heat capacity for metallic liquids.

(ii) The measured results of Al-Tb and Al-Sm within the best glass forming range (10% at. RE) are best described with a linear fit, indicating a constant heat capacity over the experimental range. Extensions of the thermodynamic value for the liquid, 45.79 J/mol K and 32.24 J/mol K for $Al_{90}Tb_{10}$ at.% and $Al_{90}Sm_{10}$ at.%, respectively, are confirmed to be suitable for 220 K undercooling for $Al_{90}Tb_{10}$ at.% and 94 K undercooling for $Al_{90}Sm_{10}$ at.%.

(iii) Further quantification of the structural dynamics of Al-RE systems requires additional investigation of lower temperature liquid regimes, which are difficult to access experimentally, even with containerless processing.

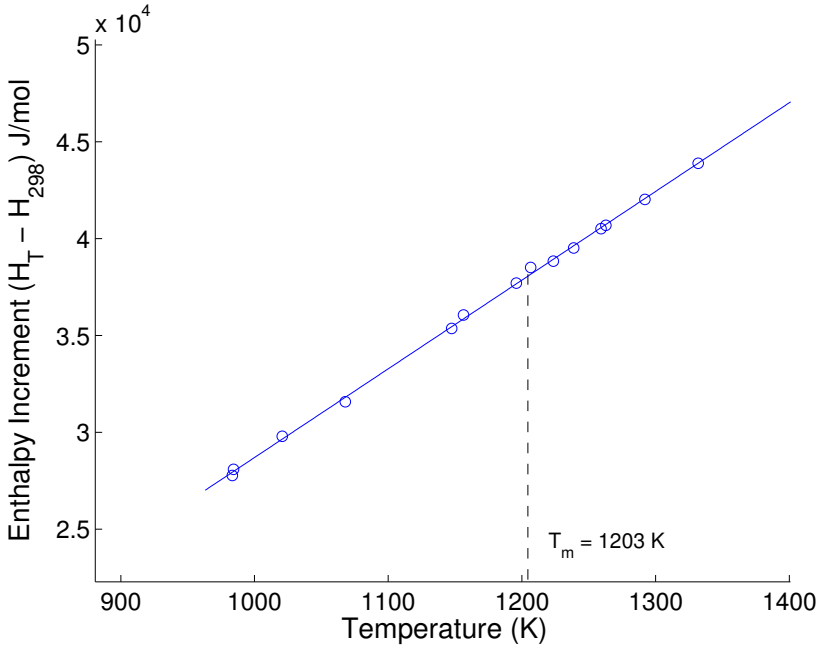

Figure A.8 Measured enthalpy increments of $Al_{90}Tb_{10}$ alloy (∘), and fit (solid line). T_{melt} is indicated by the dashed line.

Acknowledgements

This work was supported by the US Department of Energy, **Office of Basic Energy Science, Division of Material Sciences and Engineering**. The research was performed at Ames Laboratory, Ames Laboratory is operated for the US Department of Energy by Iowa State University under Contract No. DE-AC02-07CH11358.

Table A.7 Measured enthalpy increments of $Al_{90}Sm_{10}$ at% alloy

Mass (mg)	Temperature (K)	$H_T - H_{298}$ (kJ/mol)	% Deviation from fit
534.40	1294.3	40.20	0.02
493.28	1234.5	38.77	1.28
611.06	1248.6	38.73	0.02
567.90	1185.1	36.73	0.11
407.30	1192.6	37.13	0.54
493.87	1331.7	41.25	0.39
441.33	1181.6	36.35	0.61
472.00	1171.1	35.76	1.31
369.50	1147.6	35.31	0.48
350.88	1139.4	35.53	0.89

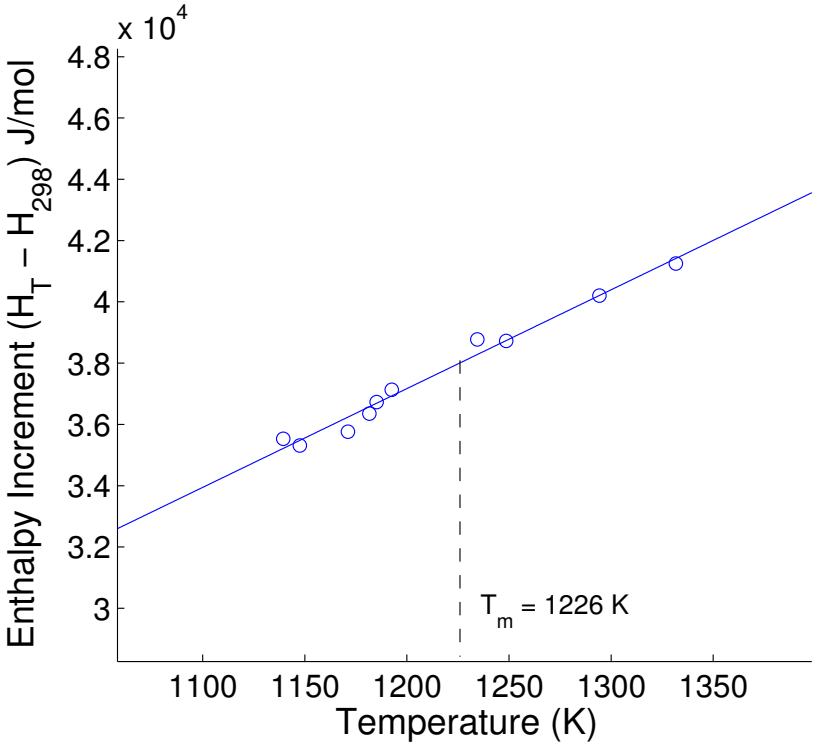

Figure A.9 Measured enthalpy increments of $Al_{90}Sm_{10}$ alloy (○), and fit (solid line). T_{melt} is indicated by the dashed line.

APPENDIX B. Drop Calorimetry Calculation with Matlab

The logic of the code can be summarized below:

1. Specify material analyzed and relevant material parameters (melting temperature, molar mass)
2. Import calorimeter file
3. Analyze calorimeter file, determine ΔT
4. Calculate enthalpy from calorimeter response, heat loss from radiation and convection, adjust for final calorimeter temperature (T_δ) with respect to the desired interval (Usually $H(T) - H_{298}$).
5. Store enthalpy values
6. Import next calorimeter file, repeat until complete
7. Output graphs and summarized enthalpy data

The code follows:

```
%This script is for calculation of enthalpy increments of liquid drops for a Levitation
Calorimetry system.
%It was created by Carl Tackes with some contributions from Zach Royer.

clc
clear all
%Set the material case, can be convenient to switch between systems
material = 'Cu';
%material = 'Al';
%material = 'AlTb';
%material = 'AlSm';
%material = 'AlTb20';

%plot switch, use for when it is desired to see each calorimeter plot
%fit switch is to be 0  when a single data point is to be calculated
%last increment plot shows the last calorimeter plot
%TC switch is used to use both thermocouples independently, and should
%be used when two thermocouples are used.
plotswitch = 0;
extendfitswitch = 0;
fitswitch = 1;
lastincrementplot = 0;
TCswitch = 1;

%The header file contains the sample ID, the drop temperature, and the
%sample mass recovered from the calorimeter.

%headerfilename = sprintf('/newheaders/%sheaderv13.csv',material);
headerfilename = sprintf('/newheaders/%stest2.csv',material);
header = csvread(headerfilename);
[a,b]=size(header);
report = size(header);
%setting the fit type for modeling the cooling portion of the calorimeter
%response, which should be newtonian.
f=fittype('a*exp(b*x)+c');

%the molecular weight, melting temperature, and heat of fusion are
%described. Only the MW is used in calculations but the others are useful
%when calibrating the calorimeter.
Cuflag = strcmp(material, 'Cu');
Alflag = strcmp(material, 'Al');
AlTbflag = strcmp(material, 'AlTb');
AlSmflag = strcmp(material, 'AlSm');
AlTb2flag = strcmp(material, 'AlTb20');
if Cuflag == 1
% coeff=[a;b;c] from Gaskell, J/mol K
coeff=[22.64;6.28e-3]; % for Copper Cp
MW=63.546; %g/mol
Tm=1084.62 + 273.15; %K
Hf=13263.28; %j/mol
Eexp=0.019;
density = 8.02; %g/cm^3 for liquid from literature
etotal = .16; %total hemispherical emissivity
%etotal = Eexp * 1.20;
CpCuRt = 24.5;
end
if Alflag == 1
CpAlRt = 24.2894; %298.15 - 700
coeff=[20.67;12.38e-3];
MW=26.9815; %g/mol
Tm=933.47; %K
Hf=10711.04; %j/mol
Eexp=0.07;
density = 2.35; %g/cm^3
etotal = .084; %estimate
end
if AlTbflag == 1
CpAlTbRt = 24.79; %neumann kopp
coeff=[20.67;12.38e-3]; %TEMPORARY ESTIMATION AS ALUMINUM
MW = 41.49; %g/mol assuming 89-11 at%
Tm = 930 + 273.15; %K
Hf = 4371; %j/mol K
Eexp=0.067;
density = 3.3;%g/cm^3
```

```
etotal = 0.0804;
end
if AlTb2flag ==1
AlTbflag = 1;
CpAlTbRt = 25.67; %neumann kopp

MW = 53.37; %g/mol assuming 80-20 at%
Tm = 1130 + 273.15; %K
Hf = 4371; %j/mol K
Eexp=0.118;
density = 3.3 * .9;%g/cm^3
etotal = Eexp * 1.2;
end

if AlSmflag == 1

CpAlSmRt = 23.7314; % fromDSC, 3 line
MW = 39.3194;
Tm = 952.8 + 273.15; %K
Hf = 4371; %unknown
Eexp=0.065;
density = 3.21; %g/cm^3
etotal = .0780; %estimate
end

%heat capacity of calorimeter, determined by calibration.
%61.85
%64.4 adiabatic
Wcal(1) = 61.643427; %for V3 with new thermocouple

if TCswitch == 0
    Wcal(2) = Wcal(1);
else
Wcal(2) = 63.05;
end
counter = 0; %the counter displays the increment of calorimeter file being processed

%Data to account for radiation during sample fall time, which is 0.178s.
C2 = 1.52e4; %for Wien approx
droptime = 0.178; %s
sigma = 5.67e-8;

%Zeroing variables can lead to faster processing time, eventually variables
%consumed too much RAM to use the feature.
% ID = zeros(1:a);
% Tdrop = zeros(1:a);
% mass = zeros(1:a);
% tstart = zeros;
% tTmin = zeros;
% Tf = zeros;
% T1 = zeros;
% tau = zeros;
% t4 = zeros;
% tmid = zeros;
% Tpeak = zeros;
% DT = zeros;
% Hdt = zeros;
% Qdt = zeros;
% cpadd = zeros;
% Qrd = zeros;
% H = zeros;
% storeRd = zeros;
%For loop to import each calorimeter file
for j=1:a
    %importing header files
    ID(j)=header(j,1);
    Tdrop(j)=header(j,2) + 273.15;
    mass(j)=header(j,3);
    %convert mass to grams
    mass(j) = mass(j)/1000;

    %If calibration changes, can define range of experiments
    if ID(j) >= 414
    Wcal(1) = 61.6; %for V3 with new thermocuple
```

```
    Wcal(2) = 61.3;
    end

    if ID(j) >= 439
        Wcal(1) = 59.9; %for V3 with new thermocuple
    Wcal(2) = 59.5;
    end

    %setting the filename and importing/cropping the data
    if ID(j) >=100
    filename = sprintf('CA-%i.xlsx',ID(j));
    else
    filename = sprintf('CA-0%i.xlsx',ID(j));
    end
if TCswitch ==1
    sheet1size = xlsread(filename,2,'B:B');
    sheet1crop = sheet1size(11:end);
    sheet2size = xlsread(filename,1,'B:B');
    sheet2crop = sheet2size(11:end);
else
    if ID >= 336
    sheet1size = xlsread(filename,2,'B:B');
    sheet1crop = sheet1size(11:end);
    sheet2crop = sheet1crop;
    else
    sheet1size = xlsread(filename,1,'B:B');
    sheet1crop = sheet1size(11:end);
    sheet2crop = sheet1crop;
    end
end

    %filling in the amount of time based on the length of the cal data
    time = (0:.367:(size(sheet1crop)/(1/.367) - 0.367))';
    DataC = [sheet1crop sheet2crop];

    %finding tstart, time of the start of the temperature increase. This is
    %done by taking the approximate derivative (using the gradient
    %function) and finding the maximum. This corresponds to the moment of
    %maximum temperature increase. Subtracting 6 points ensures that the
    %tstart is still within the room temperature regime of the calorimeter
    %reponse. Using [~,tstart(k)] is a useful way to pull out the time step
    %(X) of a desired Y.

   for k = 1:2
        [~,tstart(k)] = max(gradient(DataC(:,k)));
        tstart(k) = tstart(k) - 6;
        Tstart(k) = mean(DataC(tstart-10:tstart,k));
        Tmax(k) = max(DataC(:,k));
   end
    %determining the time of the maximum temperature, which is the peak
    %temperature of the calorimeter response.
    [~,tTmax]=max(DataC);
    tTmax=tTmax';

   [a2,b2] = size(DataC);%more counting variables
   %determining time of minimum temperature after tTmax,
   %should be the end of the data set
  for k=1:b2
    [~,tTmin(k)]=min(DataC(tTmax(k):a2,k)); %#ok<*SAGROW>
    tTmin = tTmin + tTmax;
  end
    %some functions require column variables
    tTmin=tTmin';

    %more counting variables
    [m,n]=size(DataC);
   %The time shift is used for adjusting the fitting of the cooling curve,
   %occasionally the fit requires manual adjustment
   shift=0;

%fitting the cooling portion of the data with the specified fit type f from
%before.

    for k = 1:2
```

```
     fitmodel= fit(time(tTmax(k):end), DataC(tTmax(k):end,k),f,'StartPoint', [25 -.003↵
25]);
     lineartest = fit(time(tTmax(k)+300:tTmax(k) + 500), DataC(tTmax(k)+300:tTmax(k) +↵
500,k),'poly1');
     savemodel = fit(time(tTmax(k):end), DataC(tTmax(k):end,k),f,'StartPoint', [25 -.003↵
25]);

     modelvals = coeffvalues(fitmodel);
     modela = modelvals(1)*1.185;
     modelb = modelvals(2)*.93;
     modelc = modelvals(3);

     newfitmodel = cfit(f, modela, modelb, Tstart(k));

%    Ci2 = confint(savemodel,.95);
%    Tf2=(Ci(1,3)+Ci(2,3))/2;
%    T12=(Ci(1,1)+Ci(2,1))/2+Tf;
%    tau2=(Ci(1,2)+Ci(2,2))/2;
%    Tpredict(:,k)=(T1-Tf)*exp(tau*time(:))+Tf

   %test = newfitmodel(tstart(k):20000);
   if extendfitswitch == 1
   test = savemodel(0:7000);
   end
   Ci=confint(fitmodel,.95);
   %these are coefficients
   Tf=(Ci(1,3)+Ci(2,3))/2;
   T1=(Ci(1,1)+Ci(2,1))/2+Tf;
   tau=(Ci(1,2)+Ci(2,2))/2;
  %Tpredict is the actual cooling fit
   Tpredict(:,k)=(T1-Tf)*exp(tau*time(:))+Tf;

    end

%This portion calculates the end period of heat transfer by determining
%where the fit model of the cooling curve intercepts the experimental data
%in the heat transfer period. When the difference between them is zero, the
%time is chosen
for k = 1:b2
   for p=1:m
      difft=Tpredict(p,k)-DataC(p,k);
         if difft<=0
         t4(k)=p;
         break
      end
   end
end
%this portion determines the middle of the heat transfer period by using
%the areas under the cooling curve (during the heat transfer period) and
%the area under the heat transfer period to tmid (the middle of the heat
%transfer period). It can be seen in literature as a method for corrected
%temperature rise.
for k=1:2
    tmid(k)=tstart(k)+1;
    F1=DataC(tmid(k),k)-DataC(tstart(k),k);
    F2=0;
    for p=tmid(k)+1:t4(k)
       F2=F2+Tpredict(p,k)-DataC(p,k);
    end
    while (F2>=F1)
        F1=0;
        F2=0;
        tmid(k)=tmid(k)+1;
        for p=tstart(k):tmid(k)
            F1=F1+(DataC(p,k)-DataC(tstart(k),k));
        end
        for p=tmid(k)+1:t4(k)
            F2=F2+Tpredict(p,k)-DataC(p,k);
        end
    end
end
%this portion plots the calorimeter response and marks the areas of tstart,
%tmid, tfinal (t4) and the model of the cooling curve. This is useful for
%troubleshooting.
```

```
% %
if lastincrementplot == 1

if j == a
    plotswitch = 1;
end
end

if plotswitch == 1
    for k = 1:2
    figure
    hold on
    plot(time,DataC(:,k),time+.367, Tpredict(:,k))
    %plot(time,DataC(:,k+1),time,Tpredict(:,k+1))
    %plot(tstart(k)*.367,DataC(tstart(k),k),'or')
     plot(tstart(k)*.367,Tstart(k),'or')
    plot(tstart(k)*.367,Tpredict(tstart(k),k),'og')
    plot(time(tstart(k)-10:tstart(k)),Tstart(k))
    if extendfitswitch ==1
    plot(test)
    end
    if k==1
    title(sprintf('0%i TC1',ID(j)));
    else
    title(sprintf('0%i TC2',ID(j)));
    end
    hold off
    end
end

%this calculates the delta T, which is the corrected temperature rise of
%the block from room temperature, the source of the enthalpy measurement.
%This is done by taking the value of the cooling curve at the mid point of
%heat transfer from literature.
for k=1:2
    Tpeak(k)=Tpredict(tstart(k),k);
    %Tpeak(k) = Tmax(k);
    Tpeak(k) = Tpeak(k) + 273.15; %convert to K

    oldTpeak(k) = Tpredict(tmid(k),k) + 273.15;
    DiffPeakmax(j,:) = Tpeak(k) - 273.15 - Tmax(k);

    DT(k)=Tpredict(tstart(k),k)-Tstart(k);

    Linearpredict(k) = lineartest(tstart(k));
    storelinearpre(j,k) = Linearpredict(k);
    peakcompare(j,:) = [Linearpredict(k),Tpeak(k) - 273.15];
    %DT(k)=Tpredict(tstart(k),k)-Tstart(k);
    %DT(k) = Tmax(k) - Tstart(k);
    storedt(j,k) = DT(k);
    storeTpeak(j,:) = [Tpeak(k),oldTpeak(k)];
    %integral(k) = trapz(sheet1crop(tstart:end,1)) + trapz(test(length(sheet1crop):end))
- tstart(k)*length(test(length(sheet1crop):end));
%    storeintegral(j,:) = [integral(k)];
end

%this is the temperature range relevant to the material being studied
numrange = (298.15:0.5:Tm);
 %enthalpy of the solid, accounted for the enthalpy increment nature of the
 %experiment
% Hs = (coeff(1)*numrange + 0.5*coeff(2)*(numrange.^2));
 %Hs = Hs - ((coeff(1)*298.15 + 0.5*coeff(2)*(298.15.^2)));

 %these are used for calculating the radiation loss during falling
 %P=[0.001,0.001, 0.0022,0.0063,0.00074,0.001,0.014,0.03,0.0063];
 P=[0.03,0.03, 0.0322,0.0363,0.00074,0.001,0.014,0.03,0.0063,0.001,0.001,
0.0022,0.0063,0.00074,0.001,0.014,0.03,0.0063];
 vol = mass(j)/density;
 volrad = (vol*(3/4*3.14))^(1/3); %cm
 volrad = volrad / 100; %m
 Sa = 4*3.14*volrad^2; %m^2
 storesa(j) = Sa;
 d = volrad*2;
 %convection
```

```
 Ts = Tdrop(j);
 Tg = 298;
 Tf = (Ts-Tg)/2; %Film Temp, K
 deltat = Ts - Tg;

 T0= 273.15; %K
 MWgas = 40.002602/1000; %kg/mol
 Rgas = 8.3144621E-5; %bar K mol
 Cg = 5193.1; % J/kg heat capacity of gas
 g = 9.81; %m/s^2

 %calculated gas properties
lambda = 0.144*(1 + 2.7E-4*P(j))*(Tf/T0)^(0.71*(1-2E-4*P(j))); %heat transfer coef
Rhog = (P(j) * MWgas)/(Rgas*Tg); %Gas density
Muf = 1.865E-5*(Tf/T0)^.7; %dynamic viscosity
kinv=Muf/Rhog;%kinematic viscosity
Restar = droptime*(d*Rhog*g)/(Muf);
Pr = (Cg*Muf)/lambda;

convloss = Sa*deltat*lambda/d*(MW/mass(j))*((2*droptime + 0.4*droptime^(3/2)*Pr^(1/3)*
(Restar)^(1/2)));
convloss = convloss';
storeconvloss(j) = convloss;
 %the main enthalpy calculation
for k=1:2
       RTadjust(k) = 25 - Tstart(k);
       Qdt(k) = Wcal(k)*DT(k) * MW/mass(j);
       if AlSmflag == 1
           cpadd(k) = CpAlSmRt*(Tpeak(k) - 298);
       end
       if AlTbflag == 1
           cpadd(k) = CpAlTbRt*(Tpeak(k) - 298);
       end
       if Alflag == 1
           cpadd(k) = CpAlRt*(Tpeak(k) - 298);
       end
       if Cuflag == 1
           cpadd(k) = CpCuRt*(Tpeak(k) - 298);
       end
       storecpadd(j) = cpadd(k);
       H(k) = Wcal(k)*DT(k) * MW/mass(j) + cpadd(k);
%       H2(k) = Wcal(k) * integral(k) * MW/mass(j);
 %heat loss correction while falling
 Qrd(k) = (etotal*sigma*droptime*(Tdrop(j)^4-298.15^4)*Sa) * MW/mass(j); %e = 0.83 from
bonnell thesis
 storeRd(j) = Qrd(k);
 %Hdt is the main value
 Hdt(k) = (H(k) + Qrd(k));

end
%stored values is the main storing variable. Currently the script does not
%function without clearing relevant variables from calorimeter data to next
%calorimeter data. This is used to store the information and is not cleared
%at the end
if extendfitswitch == 1
storedvalues(j,:) = [ID(j),mass(j),Tdrop(j),Hdt,storedt(j,1),(test(end) - Tstart(1))];
else
storedvalues(j,:) = [ID(j),mass(j),Tdrop(j),Hdt];
end
%this is used to fit a linear model to the enthalpy data and plot the
%results
if j == a
if fitswitch == 1

Hfit = fit(storedvalues(:,3),storedvalues(:,4),'poly1')
Hfitconf = confint(Hfit);

Hc = coeffvalues(Hfit);

numrange2 = (Tm-240:0.5:2000);
Hfitplot = Hc(1)*numrange2 + Hc(2);
Hfitconfplot1 = Hfitconf(1,1)*numrange2 + Hfitconf(1,2);
Hfitconfplot2 = Hfitconf(2,1)*numrange2 + Hfitconf(2,2);
```

```
%calculate deviations from fit
for m = 1:a
    storedeviation(m) = (Hc(1)*(Tdrop(m))+Hc(2)) - (storedvalues(m,4));
    percentdeviation(m) = (storedeviation(m) / (Hc(1)*(Tdrop(m))+Hc(2))) * 100;
end

percentdeviation = percentdeviation';
numrange3 = numrange';
%it is useful to see the enthalpy of solid as well
%Hsfit = fit(numrange3, Hs', 'poly1');
%Hsc = coeffvalues(Hsfit);
%plot of all enthalpy data
if Alflag == 1
    newrange = (1232.5-250:0.5:1232.5+250);

SGTEliquid = -795.996 + 31.748192*numrange2;
SGTEliquid2 = -795.996 + 31.748192*newrange;
EvalHfit = Hfit(newrange)';
Evaldiff = (SGTEliquid2 - EvalHfit)';
x1 = mean(Evaldiff);
SGTEvalcompare = -795.996 + 31.748192*Tdrop;
SGTEvalcompare = SGTEvalcompare';
EvalWcal = SGTEvalcompare - storedvalues(:,4);
x2 = mean(EvalWcal);
x2p = (EvalWcal/ SGTEvalcompare) * 100;
%solids
sgteT1 = (298.15:0.01:700)';
sgteT2 = (700:0.01:933.47)'; %should be 933.47
SGTEsolid1 = -7976.15 + 137.093038*sgteT1 - 24.3671976*sgteT1.*log(sgteT1) - 1.884662E-↵
3.*sgteT1.^2 - 0.8776648E-6.*sgteT1.^3 + 74092.*sgteT1.^-1; %298.15 - 700
SGTEsolid2 = -11276.24 + 223.048446*sgteT2 - 38.5844296*sgteT2.*log(sgteT2) + 18.531982↵
E-3*sgteT2.^2 - 5.764227E-6*sgteT2.^3 + 74092*sgteT2.^-1;%700 - 933.47
Hsolid1 = -7976.15 + 24.3671976*sgteT1 - ((-1.884662E-3.*sgteT1.^2) - (2*0.8776648E-6.↵
*sgteT1.^3) + (-2*74092.*sgteT1.^-1));
Hsolid2 = -11276.44 + (38.5844296*sgteT2) - ((18.531982E-3*sgteT2.^2) - (2*5.764227E-6.↵
*sgteT2.^3) + (-2*74092.*sgteT2.^-1));
end
if Alflag ==1
%calculate Hf, useful for calibration
%calchf = Hc(1)*Tm + Hc(2) - (coeff(1)*Tm + 0.5*coeff(2)*(Tm.^2) - (coeff(1)*298 + 0.5↵
*coeff(2)*(298.^2)));
calchf = Hc(1)*Tm + Hc(2) - (Hsolid2(end));
end
if Cuflag ==1
    SGTEliquid = -46.545 + 31.38*numrange2;
    SGTEvalcompare = -46.545 + 31.38*Tdrop;
    SGTEvalcompare = SGTEvalcompare';

EvalWcal = SGTEvalcompare - storedvalues(:,4);
x2 = EvalWcal;
x2p = (EvalWcal / SGTEvalcompare) * 100;


end
if AlTbflag ==1
    SGTEliquid = -13247.649 + 46.4842*numrange2;
end

%plot reference data
figure
hold on
plot(storedvalues(:,3),storedvalues(:,4), 'o')
if Alflag == 1
plot(numrange2, SGTEliquid, 'r')
plot(sgteT1, Hsolid1 , 'g')
plot(sgteT2, Hsolid2, 'g')
end
if Cuflag ==1
    plot(numrange2, SGTEliquid, 'r')
end

plot(numrange2, Hfitplot);set(gca,'FontSize',14)
%plot(numrange2, Hfitconfplot1)
%plot(numrange2, Hfitconfplot2)
```

```
[~,tmtestindex] = min(abs(numrange2 - Tm));

plot(Tm, Hfitplot(tmtestindex),'Marker', '.', 'MarkerSize', 10);
%L+S region
% plot(1113.2, 28069, 'x')
%title([material, ' Levitation Calorimetry ', date])
ylabel('Enthalpy Increment (H_T - H_{298}) J/mol', 'FontSize',16)
xlabel('Temperature (K)','FontSize',16)
xlim([1100 1500])
ylim([30000 50000])
%plot(numrange, Hs)
hold off
%above section repeated

% figure
% hold on
% plot(storedvalues(:,3),storedvalues(:,5), 'x')
% if Alflag == 1
% plot(numrange2, SGTEliquid, 'r')
% plot(sgteT1, Hsolid1 , 'g')
% plot(sgteT2, Hsolid2, 'g')
% end
% if Cuflag ==1
%     plot(numrange2, SGTEliquid, 'r')
% end
%
% plot(numrange2, Hfitplot)
% [~,tmtestindex] = min(abs(numrange2 - Tm));
%
% plot(Tm, Hfitplot(tmtestindex),'Marker', '.', 'MarkerSize', 10);
% %L+S region
% % plot(1113.2, 28069, 'x')
% title([material, ' Levitation Calorimetry ', date])
% ylabel('Enthalpy Increment (H_T - H_{298}) J/mol')
% xlabel('Temperature (K)')
% xlim([700 2000])
% ylim([0 70000])
% %plot(numrange, Hs)
% hold off

% else
%     figure
%     hold on
%     plot(storedvalues(:,3),storedvalues(:,4), 'x')
% %    plot(numrange, Hs)
end

storeTs = storedvalues(:,3);
storeHs = storedvalues(:,4);

end

counter = counter + 1


clear DataC Tpeak Tf T1 tau time tTmin tTmax Ci DT F1 F2 Tpredict
end
```

Bibliography

[1] Herbert Ipser, Adolf Mikula, and Iwao Katayama. Overview: The emf method as a source of experimental thermodynamic data. *Calphad-Computer Coupling of Phase Diagrams and Thermochemistry*, 34(3):271–278, 2010. doi:10.1016/j.calphad.2010.05.001.

[2] R. Busch, J. Schroers, and W. H. Wang. Thermodynamics and kinetics of bulk metallic glass. *Mrs Bulletin*, 32(8), 2007. doi:10.1557/mrs2007.122.

[3] R. Busch, Y. J. Kim, and W. L. Johnson. Thermodynamics and kinetics of the undercooled liquid and the glass-transition of the zr41.2ti13.8cu12.5ni10.0be22.5 alloy. *Journal of Applied Physics*, 77(8):4039–4043, 1995. doi:10.1063/1.359485.

[4] R. Busch and W. L. Johnson. The kinetic glass transition of the zr46.75ti8.25cu7.5ni10be27.5 bulk metallic glass former-supercooled liquids on a long time scale. *Applied Physics Letters*, 72(21):2695–2697, 1998. doi:10.1063/1.121102.

[5] R. Busch, W. Liu, and W. L. Johnson. Thermodynamics and kinetics of the mg65cu25y10 bulk metallic glass forming liquid. *Journal of Applied Physics*, 83(8), 1998. doi:10.1063/1.367167.

[6] S. C. Glade, R. Busch, D. S. Lee, W. L. Johnson, R. K. Wunderlich, and H. J. Fecht. Thermodynamics of cu47ti34zr11ni8, zr52.5cu17.9ni14.6al10ti5 and zr57cu15.4ni12.6al10nb5 bulk metallic glass forming alloys. *Journal of Applied Physics*, 87(10):7242–7248, 2000. doi:10.1063/1.372975.

[7] Isabella Gallino, Jan Schroers, and Ralf Busch. Kinetic and thermodynamic studies of the fragility of bulk metallic glass forming liquids. *Journal of Applied Physics*, 108(6), 2010. doi:10.1063/1.3480805.

[8] W. Kurz and D. J. Fisher. *Fundamentals of Solidification*. Trans Tech Publications Ltd, Enfield, NH, fourth revised edition edition, 1998.

[9] M. Palumbo and L. Battezzati. Thermodynamics and kinetics of metallic amorphous phases in the framework of the calphad approach. *Calphad-Computer Coupling of Phase Diagrams and Thermochemistry*, 32(2):295–314, 2008. doi:10.1016/j.calphad.2007.12.002.

[10] S. H. Zhou and R. E. Napolitano. Phase equilibria and thermodynamic limits for partitionless crystallization in the al-la binary system. *Acta Materialia*, 54(3):831–840, 2006. doi:10.1016/j.actamat.2005.10.013.

[11] A. Inoue, K. Ohtera, and T. Masumoto. New amorphous al-y, al-la and al-ce alloys prepared by melt spinning. *Japanese Journal of Applied Physics Part 2-Letters*, 27(5): L736–L739, 1988. doi:10.1143/jjap.27.l736.

[12] P. Nash and R. B. Schwarz. Calculation of the glass forming range in binary metallic systems using thermodynamic models. *Acta Metallurgica*, 36(11):3047–3053, 1988. doi:10.1016/0001-6160(88)90187-3.

[13] K. H. J. Buschow. Effect of short-range order on the thermal-stability in amorphous ti-ni alloys. *Journal of Applied Physics*, 56(2):304–306, 1984. doi:10.1063/1.333962.

[14] K. C. H. Kumar and P. Wollants. Some guidelines for thermodynamic optimisation of phase diagrams. *Journal of Alloys and Compounds*, 320(2):189–198, 2001.

[15] H. J. Fecht, J. H. Perepezko, M. C. Lee, and W. L. Johnson. Thermodynamic properties and crystallization kinetics of glass-forming undercooled liquid au-pb-sb alloys. *Journal of Applied Physics*, 68(9), 1990. doi:10.1063/1.346200.

[16] D. Turnbull and J. C. Fisher. Rate of nucleation in condensed systems. *Journal of Chemical Physics*, 17(1):71–73, 1949. doi:10.1063/1.1747055.

[17] K. S. Dubey and P. Ramachandrarao. On the free-energy change accompanying crystallization of undercooled melts. *Acta Metallurgica*, 32(1):91–96, 1984. doi:10.1016/0001-6160(84)90205-0.

[18] C. V. Thompson and F. Spaepen. Approximation of the free-energy change on crystallization. *Acta Metallurgica*, 27(12):1855–1859, 1979. doi:10.1016/0001-6160(79)90076-2.

[19] J. D. Hoffman. Thermodynamic driving force in nucleation and growth processes. *Journal of Chemical Physics*, 29(5):1192–1193, 1958. doi:10.1063/1.1744688.

[20] G. Wilde. The static and dynamic specific heat of undercooled metallic liquids. *Journal of Non-Crystalline Solids*, 307:853–862, 2002. doi:Pii s0022-3093(02)01533-8 10.1016/s0022-3093(02)01533-8.

[21] H. J. Fecht. Thermodynamic properties of amorphous solids - glass-formation and glass-transition. *Materials Transactions Jim*, 36(7):777–793, 1995.

[22] Vikas Jindal, V. C. Srivastava, and Volker Uhlenwinkel. On the role of liquid phase stability and gfa parameters. *Journal of Non-Crystalline Solids*, 355(28-30):1552–1555, 2009. doi:10.1016/j.jnoncrysol.2009.05.049.

[23] F. H. Stillinger. A topographic view of supercooled liquids and glass-formation. *Science*, 267(5206):1935–1939, 1995. doi:10.1126/science.267.5206.1935.

[24] Jun Ding, Yongqiang Cheng, and Evan Ma. Charge-transfer-enhanced prism-type local order in amorphous mg65cu25y10: Short-to-medium-range structural evolution underlying liquid fragility and heat capacity. *Acta Materialia*, 61(8):3130–3140, 2013. doi:http://dx.doi.org/10.1016/j.actamat.2013.02.004.

[25] X. W. Fang, C. Z. Wang, S. G. Hao, M. J. Kramer, Y. X. Yao, M. I. Mendelev, Z. J. Ding, R. E. Napolitano, and K. M. Ho. Spatially resolved distribution function and the medium-range order in metallic liquid and glass. *Scientific Reports*, 1, 2011. doi:194 10.1038/srep00194.

[26] S. M. Foiles and J. B. Adams. Thermodynamic properties of fcc transition-metals as calculated with the embedded-atom method. *Physical Review B*, 40(9):5909–5915, 1989. doi:10.1103/PhysRevB.40.5909.

[27] William D. Callister. *Materials Science and Engineering: An Introduction*. John Wiley and Sons Canada, Limited, 2010.

[28] K. Schaefers, M. Rosner-Kuhn, and M. G. Frohberg. Enthalpy measurements of undercooled melts by levitation calorimetry - the pure metals nickel, iron, vanadium and niobium. *Materials Science and Engineering a-Structural Materials Properties Microstructure and Processing*, 197(1):83–90, 1995. doi:10.1016/0921-5093(95)09764-3.

[29] R. Luck, I. Arpshofen, B. Predel, and J. F. Smith. Calorimetric determination of the enthalpies of formation of liquid ni-ti alloys. *Thermochimica Acta*, 131:171–181, 1988. doi:10.1016/0040-6031(88)80071-6.

[30] O. J. Kleppa. A new twin high-temperature reaction calorimeter. the heats of mixing in liquid sodium potassium nitrates. *Journal of Physical Chemistry*, 64(12):1937–1940, 1960. doi:10.1021/j100841a032.

[31] K. Itagaki and A. Yazawa. Heats of mixing in liquid silver binary alloys. *Transactions of the Japan Institute of Metals*, 10(4):259–266, 1969.

[32] L. S. Levinson. High temperature drop calorimeter. *Review of Scientific Instruments*, 33 (6):639–642, 1962. doi:10.1063/1.1746630.

[33] M. Barth, F. Joo, B. Wei, and D. M. Herlach. Measurement of the enthalpy and specific-heat of undercooled nickel and iron melts. *Journal of Non-Crystalline Solids*, 156:398–401, 1993. doi:10.1016/0022-3093(93)90205-c.

[34] J. H. Perepezko. Nucleation in undercooled liquids. *Materials Science and Engineering*, 65(1), 1984. doi:10.1016/0025-5416(84)90206-4.

[35] D. M. Herlach, R. F. Cochrane, I. Egry, H. J. Fecht, and A. L. Greer. Containerless processing in the study of metallic melts and their solidification. *International Materials Reviews*, 38(6):273–347, 1993.

[36] R. Busch, Y. J. Kim, W. L. Johnson, A. J. Rulison, W. K. Rhim, and D. Isheim. Hemispherical total emissivity and specific-heat capacity of deeply un-

dercooled zr41.2ti13.8cu12.5ni10.0be22.5 melts. *Applied Physics Letters*, 66(23), 1995. doi:10.1063/1.113619.

[37] N. Elkaddah and J. Szekely. The electromagnetic force-field, fluid-flow field, and temperature profiles in levitated metal droplets. *Metallurgical Transactions B-Process Metallurgy*, 14(3):401–410, 1983. doi:10.1007/bf02654359.

[38] K. T. Jacob, S. Priya, and Y. Waseda. Thermodynamic mixing properties and solid-state immiscibility in the systems pd-rh and pd-rh-o. *Journal of Phase Equilibria*, 19(4): 340–350, 1998. doi:10.1361/105497198770342076.

[39] M. Heyrman, C. Chatillon, H. Collas, and J. Chemin. Improvements and new capabilities for the multiple knudsen cell device used in high-temperature mass spectrometry. *Rapid Communications in Mass Spectrometry*, 18(2):163–174, 2004. doi:10.1002/rcm.1298.

[40] S. Watanabe and O. J. Kleppa. A thermochemical study of liquid and solid alloys (1-x)la+xni at 1376-k. *Journal of Chemical Thermodynamics*, 15(7):633–644, 1983. doi:10.1016/0021-9614(83)90077-0.

[41] Z. L. Royer, C. Tackes, R. Napolitano, and R. Lesar. Coil optimization for electromagnetic levitation using a genetic like algorithm. Submitted to Journal of Applied Physics, 2013.

[42] A. T. Dinsdale. Sgte data for pure elements. *Calphad-Computer Coupling of Phase Diagrams and Thermochemistry*, 15(4), 1991. doi:10.1016/0364-5916(91)90030-n.

[43] H. Okamoto. Al-sm (aluminum-samarium). *Journal of Phase Equilibria and Diffusion*, 33(3):243–243, 2012. doi:10.1007/s11669-012-0019-y.

[44] A. Inoue. Amorphous, nanoquasicrystalline and nanocrystalline alloys in al-based systems. *Progress in Materials Science*, 43(5):365–520, 1998. doi:10.1016/s0079-6425(98)00005-x.

[45] K. Hono, Y. Zhang, A. P. Tsai, A. Inoue, and T. Sakurai. Solute partitioning in partially crystallized al-ni-ce(-cu) metallic glasses. *Scripta Metallurgica Et Materialia*, 32(2):191–196, 1995. doi:10.1016/s0956-716x(99)80035-1.

[46] S. H. Zhou and R. E. Napolitano. Energetics of nonequilibrium solidification in al-sm. *Physical Review B*, 78(18), 2008. doi:184111 10.1103/PhysRevB.78.184111.

[47] D. M. Matson. *Nucleation in the Mushy Zone*. Wiley, 2012.

[48] Zachary L. Royer. *Optimizing electromagnetic levitation design to enhance thermodynamic measurement*. 3539473, Iowa State University, 2012.

[49] A. Inoue. Stabilization of metallic supercooled liquid and bulk amorphous alloys. *Acta Materialia*, 48(1):279–306, 2000. doi:10.1016/s1359-6454(99)00300-6.

[50] Y. Q. Cheng and E. Ma. Atomic-level structure and structure-property relationship in metallic glasses. *Progress in Materials Science*, 56(4):379–473, 2011. doi:10.1016/j.pmatsci.2010.12.002.

[51] H. W. Sheng, E. Ma, and M. J. Kramer. Relating dynamic properties to atomic structure in metallic glasses. *Jom*, 64(7), 2012. doi:10.1007/s11837-012-0360-y.

[52] S. Sastry, P. G. Debenedetti, and F. H. Stillinger. Signatures of distinct dynamical regimes in the energy landscape of a glass-forming liquid. *Nature*, 393(6685):554–557, 1998. doi:10.1038/31146.

[53] W. H. Wang, C. Dong, and C. H. Shek. Bulk metallic glasses. *Materials Science and Engineering R-Reports*, 44(2-3), 2004. doi:10.1016/j.mser.2004.03.001.

[54] F. Sommer. Thermodynamics of liquid alloys. *Journal of Non-Crystalline Solids*, 353 (32-40):3709–3716, 2007. doi:10.1016/j.noncrysol.2007.05.149.

[55] F. Sommer. Thermodynamic properties of undercooled liquid-metals - experiments and models. *Materials Science and Engineering a-Structural Materials Properties Microstructure and Processing*, 178(1-2):51–54, 1994. doi:10.1016/0921-5093(94)90517-7.

[56] D. Turnbull. Metastable structures in metallurgy. *Metallurgical Transactions a-Physical Metallurgy and Materials Science*, 12(5):695–708, 1981. doi:10.1007/bf02648333.

[57] R.T. DeHoff. *Thermodynamics in Materials Science*. Taylor and Francis, 2006.

[58] G. W. Lee, A. K. Gangopadhyay, T. K. Croat, T. J. Rathz, R. W. Hyers, J. R. Rogers, and K. F. Kelton. Link between liquid structure and the nucleation barrier for icosahedral quasicrystal, polytetrahedral, and simple crystalline phases in ti-zr-ni alloys: Verification of frank's hypothesis. *Physical Review B*, 72(17), 2005. doi:174107 10.1103/PhysRevB.72.174107.

[59] W. Kauzmann. The nature of the glassy state and the behavior of liquids at low temperatures. *Chemical Reviews*, 43(2):219–256, 1948. doi:10.1021/cr60135a002.

[60] P. G. Debenedetti and F. H. Stillinger. Supercooled liquids and the glass transition. *Nature*, 410(6825):259–267, 2001. doi:10.1038/35065704.

[61] J. H. Hollomon and D. Turnbull. Nucleation. *Progress in Metal Physics*, 4:333–388, 1953. doi:10.1016/0502-8205(53)90020-3.

[62] N. Saunders and A.P. Miodownik. *CALPHAD (Calculation of Phase Diagrams): A Comprehensive Guide*. Elsevier Science, 1998.

[63] L. Battezzati. Thermodynamic aspects of metastable-phase formation. *Philosophical Magazine B-Physics of Condensed Matter Statistical Mechanics Electronic Optical and Magnetic Properties*, 61(4):511–524, 1990. doi:10.1080/13642819008219290.

[64] R. Bormann, F. Gartner, and K. Zoltzer. Application of the calphad method for the prediction of amorphous phase formation. *Journal of the Less-Common Metals*, 145 (1-2):19–29, 1988. doi:10.1016/0022-5088(88)90258-5.

[65] R. Bormann and K. Zoltzer. Determination of the thermodynamic functions and calculation of phase-diagrams for metastable phases. *Physica Status Solidi a-Applied Research*, 131(2):691–705, 1992. doi:10.1002/pssa.2211310238.

[66] R. Bormann. Thermodynamics of undercooled liquids and its application to amorphous phase-formation. *Materials Science and Engineering a-Structural Materials Properties Microstructure and Processing*, 178(1-2):55–60, 1994. doi:10.1016/0921-5093(94)90518-5.

[67] K. N. Lad, K. G. Raval, and A. Pratap. Estimation of gibbs free energy difference in bulk metallic glass forming alloys. *Journal of Non-Crystalline Solids*, 334:259–262, 2004. doi:10.1016/j.jnoncrysol.2003.11.053.

[68] C. A. Angell. Formation of glasses from liquids and biopolymers. *Science*, 267(5206): 1924–1935, 1995. doi:10.1126/science.267.5206.1924.

[69] H. S. Chen and D. Turnbull. Thermal properties of gold-silicon binary alloy near eutectic composition. *Journal of Applied Physics*, 38(9):3646, 1967. doi:10.1063/1.1710186.

[70] M. D. Ediger, C. A. Angell, and S. R. Nagel. Supercooled liquids and glasses. *Journal of Physical Chemistry*, 100(31):13200–13212, 1996. doi:10.1021/jp953538d.

[71] V. K. Malinovsky and A. P. Sokolov. The nature of boson peak in raman-scattering in glasses. *Solid State Communications*, 57(9):757–761, 1986. doi:10.1016/0038-1098(86)90854-9.

[72] S. N. Taraskin and S. R. Elliott. Nature of vibrational excitations in vitreous silica. *Physical Review B*, 56(14):8605–8622, 1997. doi:10.1103/PhysRevB.56.8605.

[73] S. N. Taraskin, Y. L. Loh, G. Natarajan, and S. R. Elliott. Origin of the boson peak in systems with lattice disorder. *Physical Review Letters*, 86(7):1255–1258, 2001. doi:10.1103/PhysRevLett.86.1255.

[74] G. Adam and J. H. Gibbs. On temperature dependence of cooperative relaxation properties in glass-forming liquids. *Journal of Chemical Physics*, 43(1):139, 1965. doi:10.1063/1.1696442.

[75] M. D. Ediger. Spatially heterogeneous dynamics in supercooled liquids. *Annual Review of Physical Chemistry*, 51:99–128, 2000. doi:10.1146/annurev.physchem.51.1.99.

[76] C. A. Angell. Relaxation in liquids, polymers and plastic crystals - strong fragile patterns and problems. *Journal of Non-Crystalline Solids*, 131:13–31, 1991. doi:10.1016/0022-3093(91)90266-9.

[77] M. Goldstein. Viscous liquids and glass transition - a potential energy barrier picture. *Journal of Chemical Physics*, 51(9):3728, 1969. doi:10.1063/1.1672587.

[78] G. Csanyi, T. Albaret, M. C. Payne, and A. De Vita. "learn on the fly": A hybrid classical and quantum-mechanical molecular dynamics simulation. *Physical Review Letters*, 93 (17), 2004. doi:175503 10.1103/PhysRevLett.93.175503.

[79] D.C. Rapaport. *The Art of Molecular Dynamics Simulation*. Cambridge University Press, 2004.

[80] M. S. Daw and M. I. Baskes. Embedded-atom method - derivation and application to impurities, surfaces, and other defects in metals. *Physical Review B*, 29(12):6443–6453, 1984. doi:10.1103/PhysRevB.29.6443.

[81] M. W. Finnis and J. E. Sinclair. A simple empirical n-body potential for transition-metals. *Philosophical Magazine a-Physics of Condensed Matter Structure Defects and Mechanical Properties*, 50(1):45–55, 1984.

[82] M. J. Stott and E. Zaremba. Quasiatoms - an approach to atoms in nonuniform electronic systems. *Physical Review B*, 22(4):1564–1583, 1980. doi:10.1103/PhysRevB.22.1564.

[83] M. I. Mendelev, S. Han, D. J. Srolovitz, G. J. Ackland, D. Y. Sun, and M. Asta. Development of new interatomic potentials appropriate for crystalline and liquid iron. *Philosophical Magazine*, 83(35):3977–3994, 2003. doi:10.1080/14786430310001613264.

[84] M. S. Daw, S. M. Foiles, and M. I. Baskes. The embedded-atom method - a review of theory and applications. *Materials Science Reports*, 9(7-8):251–310, 1993. doi:10.1016/0920-2307(93)90001-u.

[85] B. J. Lee, J. H. Shim, and H. M. Park. A semi-empirical atomic potential for the fe-cr binary system. *Calphad-Computer Coupling of Phase Diagrams and Thermochemistry*, 25(4):527–534, 2001. doi:Pii s0364-5916(02)00005-6 10.1016/s0364-5916(02)00005-6.

[86] M. I. Mendelev, M. J. Kramer, C. A. Becker, and M. Asta. Analysis of semi-empirical interatomic potentials appropriate for simulation of crystalline and liquid al and cu. *Philosophical Magazine*, 88(12):1723–1750, 2008. doi:10.1080/14786430802206482.

[87] M. Asta, D. Morgan, J. J. Hoyt, B. Sadigh, J. D. Althoff, D. de Fontaine, and S. M. Foiles. Embedded-atom-method study of structural, thermodynamic, and atomic-transport properties of liquid ni-al alloys. *Physical Review B*, 59(22):14271–14281, 1999. doi:10.1103/PhysRevB.59.14271.

[88] M. I. Mendelev, M. Asta, M. J. Rahman, and J. J. Hoyt. Development of interatomic potentials appropriate for simulation of solid-liquid interface properties in al-mg alloys. *Philosophical Magazine*, 89(34-36):3269–3285, 2009. doi:Pii 917302199 10.1080/14786430903260727.

[89] M. I. Mendelev, M. J. Kramer, R. T. Ott, D. J. Sordelet, D. Yagodin, and P. Popel. Development of suitable interatomic potentials for simulation of liquid and amorphous cu-zr alloys. *Philosophical Magazine*, 89(11):967–987, 2009. doi:Pii 910503793 10.1080/14786430902832773.

[90] N. Wang, X. J. Han, and B. Wei. Specific heat and thermodynamic properties of undercooled liquid cobalt. *Applied Physics Letters*, 80(1):28–30, 2002. doi:10.1063/1.1428409.

[91] D. Bolmatov, V. V. Brazhkin, and K. Trachenko. The phonon theory of liquid thermodynamics. *Scientific Reports*, 2, 2012. doi:421 10.1038/srep00421.

[92] B. Predel, I. Arpshofen, and M. J. Pool. Calorimetric methods in metallurgy. *Thermochimica Acta*, 22(2):211–236, 1978. doi:10.1016/0040-6031(78)85089-8.

[93] O. Kubaschewski, E. LL. Evans, and C. B. Alcock. *Metallurgical Thermochemistry*. Pergamon Press, New York, 4th ed. edition, 1967.

[94] D.R. Gaskell. *Introduction to the Thermodynamics of Materials*. Taylor and Francis Group, 2008.

[95] Evan H. Copland. Measuring thermodynamic properties of metals and alloys with knudsen effusion mass spectrometry. `http://purl.fdlp.gov/GPO/gpo7998`, 2010.

[96] M. Randall and L.E. Young. *Elementary physical chemistry.* Randall and sons, 1942.

[97] G.N. Lewis and M. Randall. *Thermodynamics and the free energy of chemical substances.* McGraw-Hill, 1923.

[98] Douglas McKie and Niels h. de V. Heathcote. *The Discovery of Specific and Latent Heats.* Edward Arnold and Co., London, 1935.

[99] James Prescott Joule. On the mechanical equivalent of heat. *Philosophical Transactions of the Royal Society of London*, 140:61–82, 1850. doi:10.1098/rstl.1850.0004.

[100] W. P. White. *The Modern Calorimeter.* Chemical Catalog Company, New York, 1928.

[101] W. Hemminger and G. Hohne. *Calorimetry - Fundamentals and Practice.* Verlag Chemie, Deerfield Beach, 1984.

[102] D.Q.M. Craig and M. Reading. *Thermal Analysis of Pharmaceuticals.* Taylor and Francis, 2010.

[103] M. T. Kalichevsky, E. M. Jaroszkiewicz, and J. M. V. Blanshard. Glass-transition of gluten .1. gluten and gluten sugar mixtures. *International Journal of Biological Macromolecules*, 14(5):257–266, 1992. doi:10.1016/s0141-8130(05)80038-8.

[104] L. M. Reid, C. P. O'Donnell, and G. Downey. Recent technological advances for the determination of food authenticity. *Trends in Food Science and Technology*, 17(7):344–353, 2006. doi:10.1016/j.tifs.2006.01.006.

[105] C. D. Doyle. Estimating thermal stability of experimental polymers by empirical thermogravimetric analysis. *Analytical Chemistry*, 33(1):77–79, 1961. doi:10.1021/ac60169a022.

[106] R. W. Seymour and S. L. Cooper. Thermal-analysis of polyurethane block polymers. *Macromolecules*, 6(1):48–53, 1973. doi:10.1021/ma60031a008.

[107] O. Martin and L. Averous. Poly(lactic acid): plasticization and properties of biodegradable multiphase systems. *Polymer*, 42(14):6209–6219, 2001. doi:10.1016/s0032-3861(01)00086-6.

[108] W. Gibbs. On the equilibrium of heterogenous substances. *Transactions of the Connecticut Academy of Arts and Sciences*, 1876. doi:http://citebank.org/node/50964.

[109] K.J. Laidler. *The World of Physical Chemistry*. Oxford University Press, 1995.

[110] V. A. Shaposhnik. Walter nernst and analytical chemistry. *Journal of Analytical Chemistry*, 63(2):199–201, 2008. doi:10.1134/s1061934808020160.

[111] G. N. Lewis. Outlines of a new system of thermodynamic chemistry. *Proceedings of the American Academy of Arts and Sciences*, 43(1/12):259–293, 1907. doi:10.2307/20022322.

[112] G. N. Lewis. The law of physical-chemical procedures. *Zeitschrift Fur Physikalische Chemie–Stochiometrie Und Verwandtschaftslehre*, 38(2):205–226, 1901.

[113] B. Predel. Recent trends and developments of experimental methods for the determination of thermodynamic quantities of alloys. *Calphad-Computer Coupling of Phase Diagrams and Thermochemistry*, 6(3):199–216, 1982. doi:10.1016/0364-5916(82)90002-5.

[114] J. P. Bros. High-temperature calorimetry in metallurgy. *Journal of the Less-Common Metals*, 154(1):9–30, 1989. doi:10.1016/0022-5088(89)90166-5.

[115] K. L. Komarek. Experimental-techniques in high-temperature thermodynamics. *Pure and Applied Chemistry*, 64(1):93–102, 1992. doi:10.1351/pac199264010093.

[116] O. Kubaschewski. Experimental thermochemistry of alloys. *Thermochimica Acta*, 129 (1):11–27, 1988. doi:10.1016/0040-6031(88)87193-4.

[117] O. J. Kleppa. Evolution and application of high-temperature reaction calorimetry at the university of chicago from 1952 to 2000. *Journal of Alloys and Compounds*, 321(2): 153–163, 2001. doi:10.1016/s0925-8388(01)00964-1.

[118] W. R. Parrish. Recent advances in calorimetry. *Fluid Phase Equilibria*, 29:177–192, 1986. doi:10.1016/0378-3812(86)85020-8.

[119] J. Rouquerol and W. Zielenkiewicz. Suggested practice for classification of calorimeters. *Thermochimica Acta*, 109(1):121–137, 1986. doi:10.1016/0040-6031(86)85014-6.

[120] W. Zielenkiewicz. Calorimetric models. *Journal of Thermal Analysis*, 33(1):7–13, 1988. doi:10.1007/bf01914579.

[121] L. A. Stretz. *High Temperature Heat Content of Selected Rare Earth Metals by Levitation Calorimetry*. PhD thesis, Iowa State University, 1973.

[122] M. J. Pool, B. Predel, and E. Schultheiss. Application of the setaram high-temperature calorimeter for determination of mixing enthalpies of liquid alloys. *Thermochimica Acta*, 28(2):349–358, 1979. doi:10.1016/0040-6031(79)85138-2.

[123] R. Luck and B. Predel. The enthalpy of mixing of liquid iron-tin alloys determined by means of a new high-temperature calorimeter. *Zeitschrift Fur Metallkunde*, 76(10): 684–686, 1985.

[124] M. E. Schlesinger and S. Jacob. Advances in high-temperature calorimetry: A comparison. *Jom*, 56(12):37–40, 2004. doi:10.1007/s11837-004-0233-0.

[125] W. P. White. Specific heats of silicates and platinum. *American Journal of Science*, 28: 334–346, 1906.

[126] R.D.D. Weir and T.W. De Loos. *Measurement of the Thermodynamic Properties of Multiple Phases*. Elsevier Science & Tech, 2005.

[127] W. A. Dench. Adiabatic high-temperature calorimeter for measurement of heats of alloying. *Transactions of the Faraday Society*, 59(486):1279–1292, 1963. doi:10.1039/tf9635901279.

[128] W. A. Dench and O. Kubaschewski. Heat capacity of iron at 800 degrees to 1420 degrees c. *Journal of the Iron and Steel Institute*, 201(2):140–, 1963.

[129] S. C. Mraw and D. F. Naas. Measurement of accurate heat-capacities by differential scanning calorimetry comparison of dsc results on pyrite (100-k to 800-k) with literature values from precision adiabatic calorimetry. *Journal of Chemical Thermodynamics*, 11 (6):567–584, 1979. doi:10.1016/0021-9614(79)90097-1.

[130] C. A. Cerdeirina, J. A. Miguez, E. Carballo, C. T. E. de la Puente, and L. Romani. Highly precise determination of the heat capacity of liquids by dsc: calibration and measurement. *Thermochimica Acta*, 347(1-2):37–44, 2000. doi:10.1016/s0040-6031(99)00414-1.

[131] B. A. Mueller and J. H. Perepezko. The undercooling of aluminum. *Metallurgical Transactions a-Physical Metallurgy and Materials Science*, 18(6):1143–1150, 1987.

[132] J. A. Graves, J. H. Perepezko, C. H. Ward, and F. H. Froes. Microstructural development in rapidly solidified tial. *Scripta Metallurgica*, 21(4):567–572, 1987. doi:10.1016/0036-9748(87)90202-x.

[133] D. Turnbull. Formation of crystal nuclei in liquid metals. *Journal of Applied Physics*, 21 (10):1022–1028, 1950. doi:10.1063/1.1699435.

[134] D. Turnbull. Kinetics of heterogeneous nucleation. *Journal of Chemical Physics*, 18(2): 198–203, 1950. doi:10.1063/1.1747588.

[135] B. Vonnegut. Variation with temperature of the nucleation rate of supercooled liquid tin and water drops. *Journal of Colloid Science*, 3(6):563–569, 1948. doi:10.1016/s0095-8522(48)90049-x.

[136] C. C. Wang and C. S. Smith. Undercooling of minor liquid phases in binary alloys. *Transactions of the American Institute of Mining and Metallurgical Engineers*, 188(1): 136–138, 1950.

[137] Y. He, T. D. Shen, and R. B. Schwarz. Bulk amorphous metallic alloys: Synthesis by fluxing techniques and properties. *Metallurgical and Materials Transactions a-Physical Metallurgy and Materials Science*, 29(7):1795–1804, 1998. doi:10.1007/s11661-998-0002-8.

[138] C. E. Mendenhall and L. R. Ingersoll. On certain phenomena exhibited by small particles on a nernst glower. *Philosophical Magazine*, 15(85-90):205–214, 1908.

[139] J. H. Perepezko and J. S. Paik. Thermodynamic properties of undercooled liquid-metals. *Journal of Non-Crystalline Solids*, 61-2(JAN), 1984. doi:10.1016/0022-3093(84)90538-6.

[140] T. Mizoguchi and J. H. Perepezko. Nucleation behavior during solidification of cast iron at high undercooling. *Materials Science and Engineering a-Structural Materials Properties Microstructure and Processing*, 226:813–817, 1997. doi:10.1016/s0921-5093(97)80085-8.

[141] J. C. Fisher, J. H. Hollomon, and D. Turnbull. Rate of nucleation of solid particles in a subcooled liquid. *Science*, 109(2825):168–169, 1949. doi:10.1126/science.109.2825.168-a.

[142] H. S. Chen and D. Turnbull. Evidence of a glass-liquid transition in a gold-germanium-silicon alloy. *Journal of Chemical Physics*, 48(6):2560, 1968. doi:10.1063/1.1669483.

[143] H. S. Chen and D. Turnbull. Specific heat of tin and gallium in their stable and undercooled pure liquid states. *Acta Metallurgica*, 16(3):369–, 1968. doi:10.1016/0001-6160(68)90023-0.

[144] R. Willnecker, K. Wittmann, and G. P. Gorler. Undercooling investigations and heat-capacity measurements on pd-ni-p melts. *Journal of Non-Crystalline Solids*, 156:450–454, 1993. doi:10.1016/0022-3093(93)90217-l.

[145] I. Egry, A. Diefenbach, W. Dreier, and J. Piller. Containerless processing in space-thermophysical property measurements using electromagnetic levitation. *International Journal of Thermophysics*, 22(2):569–578, 2001. doi:10.1023/a:1010753805462.

[146] R. K. Wunderlich and H. J. Fecht. Thermophysical properties of bulk metallic glass forming alloys in the stable and undercooled liquid - a microgravity investigation. *Materials Transactions*, 42(4):565–578, 2001. doi:10.2320/matertrans.42.565.

[147] Krishnan Shankar. *Thermophysical and Optical Property Measurements of Electromagnetically-Levitated Liquid Metals*. PhD thesis, Rice University, 1989.

[148] Dominika Jendrzejczyk-Handzlik and Krzysztof Fitzner Firtzner. *Electromotive Force Measurements in High-Temperature Systems*, chapter 7, pages 125–152. Intech, 2011. doi:10.5772/30231.

[149] Z. Moser and K. Fitzner. The use of experimental thermodynamic data in the phase equilibria verification. *Thermochimica Acta*, 332(1):1–19, 1999. doi:10.1016/s0040-6031(99)00061-1.

[150] J. N. Pratt. Applications of solid electrolytes in thermodynamic studies of materials - a review. *Metallurgical Transactions a-Physical Metallurgy and Materials Science*, 21(5): 1223–1250, 1990. doi:10.1007/bf02698252.

[151] D. M. Babanly, Yu A. Yusibov, and M. B. Babanly. Phase equilibria and thermodynamic properties of the system tl-tlbr-se. *Russian Journal of Inorganic Chemistry*, 52(5):761–767, 2007. doi:10.1134/s0036023607050178.

[152] K. Kiukkola and C. Wagner. Measurements on galvanic cells involving solid electrolytes. *Journal of the Electrochemical Society*, 104(6):379–387, 1957. doi:10.1149/1.2428586.

[153] R. W. Taylor and H. Schmalzried. Free energy of formation of some titanates silicates + magnesium aluminate from measurements made with galvanic cells involving solid electrolytes. *Journal of Physical Chemistry*, 68(9):2444, 1964. doi:10.1021/j100791a010.

[154] S. Stolen and T. Grande. *Chemical Thermodynamics of Materials: Macroscopic and Microscopic Aspects*. John Wiley and Sons, 2004.

[155] M. Knudsen. Experimental determination of the pressure of saturated mercury steam at 0 degrees and at higher temperatures. *Annalen der Physik*, 29(6):179–193, 1909.

[156] M. Knudsen. The laws of the molecular current and the internal friction current of gases by channels. *Annalen der Physik*, 29(1):75–130, 1909.

[157] M. Knudsen. The molecular current of gases through openings and the effusion. *Annalen der Physik*, 29(5):999–1016, 1909.

[158] Mavr da Silva and M. J. S. Monte. The construction, testing and use of a new knudsen effusion apparatus. *Thermochimica Acta*, 171:169–183, 1990. doi:10.1016/0040-6031(90)87017-7.

[159] Mavr da Silva, M. J. S. Monte, and Lmnbf Santos. The design, construction, and testing of a new knudsen effusion apparatus. *Journal of Chemical Thermodynamics*, 38(6):778–787, 2006. doi:10.1016/j.jct.2005.08.013.

[160] J. Drowart, R. P. Burns, G. Demaria, and M. G. Inghram. Mass spectrometric study of carbon vapor. *Journal of Chemical Physics*, 31(4):1131–1132, 1959. doi:10.1063/1.1730519.

[161] P. K. Raychaudhuri and F. E. Stafford. Alloy thermodynamics by mass-spectrometry - critical review. *Materials Science and Engineering*, 20(1):1–18, 1975. doi:10.1016/0025-5416(75)90125-1.

[162] Eiichi Kato. Thermodynamic studies of metallurgical systems by mass spectrometry. *Journal of the Mass Spectrometry Society of Japan*, 41(6):297–316, 1993. doi:http://dx.doi.org/10.5702/massspec.41.297.

[163] G. R. Belton and R. J. Fruehan. Determination of activities by mass spectrometry .i. liquid metallic systems iron-nickel and iron-cobalt. *Journal of Physical Chemistry*, 71(5): 1403–1409, 1967. doi:10.1021/j100864a034.

[164] J. Berkowitz and W. A. Chupka. Composition of vapors in equilibrium with salts at high temperatures. *Annals of the New York Academy of Sciences*, 79(11):1073–1078, 1960. doi:10.1111/j.1749-6632.1960.tb42773.x.

[165] J. Drowart, C. Chatillon, J. Hastie, and D. Bonnell. High-temperature mass spectrometry: Instrumental techniques, ionization cross-sections, pressure measurements, and thermodynamic data - (iupac technical report). *Pure and Applied Chemistry*, 77(4):683–737, 2005. doi:10.1351/pac200577040683.

[166] W. R. Smythe. *Static and Dynamic Electricity.* McGraw-Hill Book Co., New York, 1950.

[167] Otto. Muck. Process and arrangement for melting, especially of conductors, etc. by electrical induction currents, 1923.

[168] E. C. Okress and D. M. Wroughton. Electromagnetic levitation of solid and molten metals. *Journal of Applied Physics*, 23(5):545–552, 1952. doi:10.1063/1.1702249.

[169] M. G. Frohberg. Thirty years of levitation melting calorimetry - a balance. *Thermochimica Acta*, 337(1-2):7–17, 1999. doi:10.1016/s0040-6031(99)00159-8.

[170] D. M. Wroughton, E. C. Okress, P. H. Brace, G. Comenetz, and J. C. R. Kelly. A technique for eliminating crucibles in heating and melting of metals. *Journal of the Electrochemical Society*, 99(5):205–211, 1952. doi:10.1149/1.2779703.

[171] Melting metals in mid-air. *Life*, June 16 1952.

[172] Delbert James Jackson. *Electromagnetic levitation of a solid metallic torus*. PhD thesis, University of Toronto, 2001.

[173] J. Vanauden. Vacuum evaporation of metals by high frequency levitation heating. *Review of Scientific Instruments*, 36(3):383–385, 1965. doi:10.1063/1.1719577.

[174] E. Fromm and H. Jehn. Electromagnetic forces and power absorption in levitation melting. *British Journal of Applied Physics*, 16(5):653–659, 1965. doi:10.1088/0508-3443/16/5/308.

[175] J. A. Treverton and J. L. Margrave. Thermodynamic properties by levitation calorimetry .3. enthalpies of fusion and heat capacities for liquid phases of iron, tatanium, and vanadium. *Journal of Chemical Thermodynamics*, 3(4):473, 1971. doi:10.1016/s0021-9614(71)80029-0.

[176] D.W. Bonnell. *Property Measurements at High Temperatures - Levitation Calorimetry Studies of Liquid Metals*. PhD thesis, Rice University, 1972.

[177] L. A. Stretz and R. G. Bautista. High-temperature heat content of liquid yttrium by levitation calorimetry. *Metallurgical Transactions*, 5(4):921–928, 1974. doi:10.1007/bf02643149.

[178] L. A. Stretz and R. G. Bautista. High-temperature enthalpy of liquid lanthanum by levitation calorimetry. *Journal of Chemical Thermodynamics*, 7(1):83–88, 1975. doi:10.1016/0021-9614(75)90084-1.

[179] L. A. Stretz and R. G. Bautista. Liquid praseodymium heat content by levitation calorimetry. *Journal of Chemical and Engineering Data*, 21(1):13–15, 1976. doi:10.1021/je60068a032.

[180] K. Ohsaka, J. R. Gatewood, and E. H. Trinh. An apparatus for the specific-heat measurement of undercooled liquids. *Scripta Metallurgica Et Materialia*, 25(6):1459–1464, 1991. doi:10.1016/0956-716x(91)90433-2.

[181] M. Rosner-Kuhn, D. M. Matson, K. Drewes, U. Thiedemann, G. Kuppermann, M. C. Flemings, and M. G. Frohberg. Enthalpies and heat capacities of liquid fe-cr-ni alloys with the focus on pure liquid chromium. *Thermochimica Acta*, 314(1-2):123–129, 1998. doi:10.1016/s0040-6031(97)00460-7.

[182] M. Rosner-Kuhn, K. Drewes, H. Franz, and M. G. Frohberg. Enthalpy measurements of the solid high-temperature beta-phase and the liquid phase of hafnium (3 wt. *Materials Science and Engineering a-Structural Materials Properties Microstructure and Processing*, 308(1-2):60–64, 2001. doi:10.1016/s0921-5093(00)02044-x.

[183] N. Wang and B. Wei. Thermodynamic properties of highly undercooled liquid tial alloy. *Applied Physics Letters*, 80(19):3515–3517, 2002. doi:10.1063/1.1478777.

[184] X. J. Han and B. Wei. Thermophysical properties of undercooled liquid co-mo alloys. *Philosophical Magazine*, 83(13):1511–1532, 2003. doi:10.1080/1478643031000090284.

[185] D. M. Herlach. Containerless undercooling and solidification of pure metals. *Annual Review of Materials Science*, 21:23–44, 1991. doi:10.1146/annurev.ms.21.080191.000323.

[186] D.W. Bonnell, R. L. Montgomery, B. Stephenson, P. C. Sundareswaran, and J. L. Margrave. *Levitation Calorimetry*, chapter 7, pages 265–298. Hemisphere, New York, 1988.

[187] M. Schonhuber. Breakdown of gases below paschen minimum - basic design data of high-voltage equipment. *Ieee Transactions on Power Apparatus and Systems*, PA88(2): 100–107, 1969. doi:10.1109/tpas.1969.292410.

[188] Friedrich Paschen. Ueber die zum funkenübergang in luft, wasserstoff und kohlensäure bei verschiedenen drucken erforderliche potentialdifferenz. *Annalen der Physik*, 273(5): 69–96, 1889. doi:10.1002/andp.18892730505.

[189] L. D. Hansen and R. M. Hart. The art of calorimetry. *Thermochimica Acta*, 417(2): 257–273, 2004. doi:10.1016/j.tca.2003.07.023.

[190] Peter J. Mohr, Barry N. Taylor, and David B. Newell. Codata recommended values of the fundamental physical constants: 2010. *Reviews of Modern Physics*, 84(4):1527–1605, 2012. doi:10.1103/RevModPhys.84.1527.

[191] P. B. Coates. Multi-wavelength pyrometry. *Metrologia*, 17(3):103–109, 1981. doi:10.1088/0026-1394/17/3/006.

[192] J. A. Treverton and J. L. Margrave. Levitation calorimetry .4. thermodynamic properties of liquid cobalt and palladium. *Journal of Physical Chemistry*, 75(24):3737, 1971. doi:10.1021/j100693a018.

[193] R. P. Liu, D. M. Herlach, M. Vandyoussefi, and A. L. Greer. Undercooling and solidification of al-50 at. pct si alloy by electromagnetic levitation. *Metallurgical and Materials Transactions a-Physical Metallurgy and Materials Science*, 35A(2):607–612, 2004. doi:10.1007/s11661-004-0372-5.

[194] R. Brooks and A. Day. Observations of the effects of oxide skins on the oscillations of electromagnetically levitated metal droplets. *International Journal of Thermophysics*, 20 (4):1041–1050, 1999. doi:10.1023/a:1022642501415.

[195] M. J. Assael, K. Kakosimos, R. M. Banish, J. Brillo, I. Egry, R. Brooks, P. N. Quested, K. C. Mills, A. Nagashima, Y. Sato, and W. A. Wakeham. Reference data for the density

and viscosity of liquid aluminum and liquid iron. *Journal of Physical and Chemical Reference Data*, 35(1):285–300, 2006. doi:10.1063/1.2149380.

[196] H. Petersen. *The Properties of Helium: Density, Specific Heats, Viscosity and Thermal Conductivity at Pressures from 1 to 100 Bar and from Room Temperature to about 1800K.* 1970.

[197] Michael E. Wieser and Tyler B. Coplen. Atomic weights of the elements 2009 (iupac technical report). *Pure and Applied Chemistry*, 83(2):359–396, 2011. doi:10.1351/pac-rep-10-09-14.

[198] R. Ferro, G. Borzone, G. Cacciamani, and R. Raggio. Calorimetric measurements in metallurgy: remarks on calibration and some specific problems. *Thermochimica Acta*, 347(1-2):103–122, 2000. doi:http://dx.doi.org/10.1016/S0040-6031(99)00422-0.

[199] P. Predecki, Mullendo.Aw, and N. J. Grant. A study of splat cooling technique. *Transactions of the Metallurgical Society of Aime*, 233(8):1581, 1965.

[200] P. Ramachan., M. G. Scott, and G. A. Chadwick. Constitution and microstructure of rapidly solidified aluminum-germanium alloys. *Philosophical Magazine*, 25(4):961, 1972. doi:10.1080/14786437208229316.

[201] H. A. Davies and J. B. Hull. Amorphous phase in a splat-quenched al-17.3at percent cu alloy. *Scripta Metallurgica*, 6(3):241–245, 1972. doi:10.1016/0036-9748(72)90174-3.

[202] P. Furrer and H. Warlimont. Crystalline and amorphous structures of rapidly solidified al-cr alloys. *Materials Science and Engineering*, 28(1):127–137, 1977. doi:10.1016/0025-5416(77)90096-9.

[203] H. H. Liebermann and C. D. Graham. Production of amorphous alloy ribbons and effects of apparatus parameters on ribbon dimensions. *Ieee Transactions on Magnetics*, 12(6): 921–923, 1976. doi:10.1109/tmag.1976.1059201.

[204] A. Inoue, A. Kitamura, and T. Masumoto. The effect of aluminum on mechanical-properties and thermal-stability of (fe,co,ni)-al-b ternary amorphous-alloys. *Journal of Materials Science*, 16(7):1895–1908, 1981. doi:10.1007/bf00540638.

[205] A. Inoue, M. Yamamoto, H. M. Kimura, and T. Masumoto. Ductile aluminum-base amorphous-alloys with 2 separate phases. *Journal of Materials Science Letters*, 6(2): 194–196, 1987. doi:10.1007/bf01728983.

[206] A. Inoue, K. Ohtera, A. P. Tsai, and T. Masumoto. Aluminum-based amorphous-alloys with tensile-strength above 980 mpa (100 kg mm2). *Japanese Journal of Applied Physics Part 2-Letters*, 27(4):L479–L482, 1988. doi:10.1143/jjap.27.l479.

[207] A. Inoue, K. Ohtera, A. P. Tsai, H. Kimura, and T. Masumoto. Glass-transition behavior of al-y-ni and al-ce-ni amorphous-alloys. *Japanese Journal of Applied Physics Part 2-Letters*, 27(9):L1579–L1582, 1988.

[208] A. Inoue, K. Ohtera, K. Kita, and T. Masumoto. New amorphous-alloys with good ductility in al-ce-nb, al-ce-fe, al-ce-co, al-ce-ni, al-ce-cu systems. *Japanese Journal of Applied Physics Part 2-Letters*, 27(10):L1796–L1799, 1988.

[209] A. Inoue, K. Ohtera, A. P. Tsai, and T. Masumoto. New amorphous-alloys with good ductility in al-y-m and al-la-m (m=fe, co, ni or cu) systems. *Japanese Journal of Applied Physics Part 2-Letters*, 27(3):L280–L282, 1988. doi:10.1143/jjap.27.l280.

[210] A. Inoue, K. Ohtera, K. Kita, and T. Masumoto. New amorphous mg-ce-ni alloys with high-strength and good ductility. *Japanese Journal of Applied Physics Part 2-Letters*, 27 (12):L2248–L2251, 1988.

[211] Y. He, S. J. Poon, and G. J. Shiflet. Synthesis and properties of metallic glasses that contain aluminum. *Science*, 241(4873):1640–1642, 1988. doi:10.1126/science.241.4873.1640.

[212] Y. H. Kim, A. Inoue, and T. Masumoto. Increase in mechanical strength of al-y-ni amorphous-alloys by dispersion of nanoscale fcc-al particles. *Materials Transactions Jim*, 32(4):331–338, 1991.

[213] S. J. Savage, D. Eliezer, and F. H. Froes. Microstructural observations and thermal-stability of a rapidly solidified aluminum-gadolinium alloy. *Metallurgical Transactions a-Physical Metallurgy and Materials Science*, 18(8):1533–1536, 1987. doi:10.1007/bf02646666.

[214] A. Ruder and D. Eliezer. Microstructural transitions in an rs al-4la alloy. *Journal of Materials Science*, 24(4):1474–1478, 1989. doi:10.1007/bf00553183.

[215] A. Inoue, K. Ohtera, Z. Tao, and T. Masumoto. New amorphous al-pr, al-nd, al-sm or al-gd alloys prepared by melt spinning. *Japanese Journal of Applied Physics Part 2-Letters*, 27(9):L1583–L1586, 1988.

[216] F. Q. Guo, S. J. Poon, and G. J. Shiflet. *Glass formability in Al-based multinary alloys*, volume 331-3 of *Materials Science Forum*, pages 31–41. Trans Tech Publications Ltd, Zurich-Uetikon, 2000. doi:10.4028/www.scientific.net/MSF.331-337.31.

[217] T. Masumoto. Recent progress in amorphous metallic materials in japan. *Materials Science and Engineering a-Structural Materials Properties Microstructure and Processing*, 179:8–16, 1994. doi:10.1016/0921-5093(94)90155-4.

[218] J. H. Perepezko, R. J. Hebert, and W. S. Tong. Amorphization and nanostructure synthesis in al alloys. *Intermetallics*, 10(11-12):1079–1088, 2002. doi:10.1016/s0966-9795(02)00144-9.

[219] T. Egami and Y. Waseda. Atomic size effect on the formability of metallic glasses. *Journal of Non-Crystalline Solids*, 64(1-2):113–134, 1984. doi:10.1016/0022-3093(84)90210-2.

[220] H. Y. Hsieh, B. H. Toby, T. Egami, Y. He, S. J. Poon, and G. J. Shiflet. Atomic-structure of amorphous al90fexce10-x. *Journal of Materials Research*, 5(12):2807–2812, 1990. doi:10.1557/jmr.1990.2807.

[221] K. Nakazato, Y. Kawamura, A. P. Tsai, A. Inoue, and T. Masumoto. On the growth of nanocrystalline grains in an aluminum-based amorphous alloy. *Applied Physics Letters*, 63(19):2644–2646, 1993. doi:10.1063/1.110407.

[222] J. C. Foley, D. R. Allen, and J. H. Perepezko. Analysis of nanocrystal development in al-y-fe and al-sm glasses. *Scripta Materialia*, 35(5):655–660, 1996. doi:10.1016/1359-6462(96)00196-0.

[223] A. P. Tsai, T. Kamiyama, Y. Kawamura, A. Inoue, and T. Masumoto. Formation and precipitation mechanism of nanoscale al particles in al-ni base amorphous alloys. *Acta Materialia*, 45(4):1477–1487, 1997. doi:10.1016/s1359-6454(96)00268-6.

[224] G. Wilde, H. Sieber, and J. H. Perepezko. Glass formation versus nanocrystallization in an al92sm8 alloy. *Scripta Materialia*, 40(7):779–783, 1999. doi:10.1016/s1359-6462(99)00029-9.

[225] R. I. Wu, G. Wilde, and J. H. Perepezko. Glass formation and primary nanocrystallization in al-base metallic glasses. *Materials Science and Engineering a-Structural Materials Properties Microstructure and Processing*, 301(1):12–17, 2001. doi:10.1016/s0921-5093(00)01390-3.

[226] W. G. Stratton, J. Hamann, J. H. Perepezko, P. M. Voyles, X. Mao, and S. V. Khare. Aluminum nanoscale order in amorphous al92sm8 measured by fluctuation electron microscopy. *Applied Physics Letters*, 86(14), 2005. doi:141910 10.1063/1.1897830.

[227] M. M. J. Treacy, J. M. Gibson, L. Fan, D. J. Paterson, and I. McNulty. Fluctuation microscopy: a probe of medium range order. *Reports on Progress in Physics*, 68(12): 2899–2944, 2005. doi:10.1088/0034-4885/68/12/r06.

[228] Y. E. Kalay, L. S. Chumbley, and I. E. Anderson. Crystallization behavior in a highly driven marginal glass forming alloy. *Journal of Non-Crystalline Solids*, 354(26):3040–3048, 2008. doi:10.1016/j.jnoncrysol.2007.12.006.

[229] Y. E. Kalay, C. Yeager, L. S. Chumbley, M. J. Kramer, and I. E. Anderson. Initial crystallization in a nanostructured al-sm rare earth alloy. *Journal of Non-Crystalline Solids*, 356(28-30):1416–1424, 2010. doi:10.1016/j.jnoncrysol.2010.05.005.

[230] Y. E. Kalay, I. Kalay, Jinwoo Hwang, P. M. Voyles, and M. J. Kramer. Local chemical and topological order in al-tb and its role in controlling nanocrystal formation. *Acta Materialia*, 60(3):994–1003, 2012. doi:10.1016/j.actamat.2011.11.008.

[a] Materials preparation center, a. l., us doe basic energy sciences, ames, ia. `www.ameslab.gov/mpc`.

[231] S. H. Zhou and R. E. Napolitano. Modeling of thermodynamic properties and phase equilibria for the al-sm binary system. *Metallurgical and Materials Transactions a-Physical Metallurgy and Materials Science*, 39A(3):502–512, 2008. doi:10.1007/s11661-007-9445-6.

[232] S. H. Zhou, C. Tackes, Y. Huo, and R. E. Napolitano. Phase stability for the al-tb system: First principles, experiments and solution based modeling. To be submitted., 2013.

[233] A. Inoue and A. Takeuchi. Recent progress in bulk glassy alloys. *Materials Transactions*, 43(8), 2002. doi:10.2320/matertrans.43.1892.

[234] Y. E. Kalay, L. S. Chumbley, and I. E. Anderson. Characterization of a marginal glass former alloy solidified in gas atomized powders. *Materials Science and Engineering a-Structural Materials Properties Microstructure and Processing*, 490(1-2):72–80, 2008. doi:10.1016/j.msea.2008.02.032.

[235] N. Wang, Y. E. Kalay, and R. Trivedi. Eutectic-to-metallic glass transition in the al-sm system. *Acta Materialia*, 59(17):6604–6619, 2011. doi:10.1016/j.actamat.2011.07.015.